

# **Growth mechanism and structure of epitaxial perovskite thin films and superlattices**

## **Dissertation**

zur Erlangung des akademischen Grades

Doctor rerum naturalium (Dr. rer. nat.)

vorgelegt der

Mathematisch-Naturwissenschaftlich-Technischen Fakultät  
(mathematisch-naturwissenschaftlicher Bereich)  
der Martin-Luther-Universität Halle-Wittenberg

von Frau Alina Mihaela Visinoiu  
geb.: 27.06.1974 in: Pitesti

Gutachter:

1. Prof. Dr. H. Neddermeyer
2. Prof. Dr. U. Gösele
3. Prof. Dr. H.-U. Krebs

Halle (Saale), am 10 Februar 2003.

**urn:nbn:de:gbv:3-000004646**

[<http://nbn-resolving.de/urn/resolver.pl?urn=nbn%3Ade%3Agbv%3A3-000004646>]

# Contents

<b>1</b>	<b>Introduction</b>	<b>1</b>
<b>2</b>	<b>Ferroelectric oxide thin films - structure, growth, downscaling</b>	<b>3</b>
<b>3</b>	<b>Experimental and characterization methods</b>	<b>19</b>
3.1	Pulsed laser deposition . . . . .	19
3.2	X-ray diffraction . . . . .	32
3.3	Atomic force microscopy . . . . .	38
3.4	Transmission electron microscopy . . . . .	39
3.5	Electrical measurements . . . . .	40
<b>4</b>	<b>Results and discussion</b>	<b>42</b>
4.1	Vicinal SrTiO <sub>3</sub> substrate surfaces . . . . .	42
4.1.1	General remarks . . . . .	42
4.1.2	Preparation of vicinal SrTiO <sub>3</sub> substrate surfaces . . . . .	43
4.2	Epitaxial BaTiO <sub>3</sub> thin films . . . . .	49
4.2.1	Initial growth stages of BaTiO <sub>3</sub> thin films on SrTiO <sub>3</sub> surfaces . . . . .	49
4.2.2	Analysis of the crystallographic orientation . . . . .	56
4.2.3	Later growth stages . . . . .	60
4.2.4	Concluding remarks . . . . .	67
4.3	Epitaxial BaTiO <sub>3</sub> /SrTiO <sub>3</sub> multilayers . . . . .	69
4.3.1	Expected stresses in BaTiO <sub>3</sub> /SrTiO <sub>3</sub> multilayers . . . . .	69
4.3.2	Growth, structure and morphology of BaTiO <sub>3</sub> /SrTiO <sub>3</sub> multilayers . . . . .	70
4.3.3	Concluding remarks . . . . .	78
4.4	Dielectric properties . . . . .	79
4.4.1	BaTiO <sub>3</sub> films . . . . .	79
4.4.2	BaTiO <sub>3</sub> /SrTiO <sub>3</sub> multilayers . . . . .	85
<b>5</b>	<b>Conclusions and outlook</b>	<b>90</b>
	<b>Bibliography</b>	<b>92</b>



# 1 Introduction

Barium titanate ( $\text{BaTiO}_3$ ) and Ba-rich solid solutions of barium-strontium titanate  $[(\text{Ba,Sr})\text{TiO}_3]$  are attractive in applications due to their large dielectric permittivity at  $T > T_c$ , a sufficiently low temperature dependence of the remanent polarization at  $T < T_c$ , a moderate coercive field and a large electro-optic coefficient. One of their most promising applications is their use as storage capacitors for dynamic random access memory (DRAM) like storage capacitors for high densities above 1 Gb. This attractiveness resulted in many research activities on  $(\text{Ba,Sr})\text{TiO}_3$  thin films over the recent years.  $(\text{Ba,Sr})\text{TiO}_3$ , e.g., almost dominated the research field of dielectric materials for high-permittivity dielectrics with respect to a variety of applications (e.g. as a replacement for silicon oxide or nitride dielectrics<sup>[1]</sup>). However, in recent years also other functional oxides (superconducting, piezoelectric, ferroelectric, magnetoresistiv) have been studied extensively. Their physical properties in thin films can now be fine-tuned or modified, due to well-controlled growth conditions or careful selection of substrates, and due to strain effects, interfacial or boundary and coupling effects, if different layers are assembled together. As a result, oxide superlattice materials, with an artificial control of the crystal structure, can now be grown, and their properties are studied in order to find new functions of ceramic systems, eventually leading to applications such as piezoelectric actuators, non-volatile memories, IR detectors and Josephson devices.

While research on semiconductor superlattices started quite early, research on artificial oxide superlattices begun only in the early 1990ies. Among other systems,  $\text{BaTiO}_3/\text{SrTiO}_3$  multilayers and superlattices attracted attention. They have been prepared by several groups<sup>[2, 3, 4, 5, 6, 7, 8]</sup> and showed quite different dielectric properties compared to single-phase  $\text{BaTiO}_3$  or  $(\text{Ba,Sr})\text{TiO}_3$ . Particularly,  $\text{BaTiO}_3/\text{SrTiO}_3$  superlattices show a dramatically increased dielectric constant and large optical non-linearity. Generally, dielectric and ferroelectric superlattices offer a promising approach to create new ferroelectric materials and to study the origin of their remarkable properties. Concerning ferroelectric superlattices, one principal idea put forward is to enhance the tetragonality and the ferroelectric distortions of  $\text{BaTiO}_3$  in strained superlattices by help of the relatively large mismatch of, e.g., about 3% between the in-plane lattice parameters of  $\text{BaTiO}_3$  and another oxide, like  $\text{SrTiO}_3$ . Naturally, the properties of such superlattices are very sensitive to the thickness of each layer and the microstructure of the interface. Therefore, a control of the superlattice structure at an atomic scale and the characterization of the surface and the interfaces are particularly important. A well-defined control of the microstructure of a superlattice, however, requires insight into the initial growth stages of the involved thin-film materials.

Initial growth stages of epitaxial oxides have not been studied in sufficient detail up to now. Moreover, the operating growth mechanism in  $\text{BaTiO}_3/\text{SrTiO}_3$  systems is still controversial. It has still not yet been settled whether, and under which conditions,  $\text{BaTiO}_3$  films growing on  $\text{SrTiO}_3$  substrates by pulsed laser deposition (PLD) are growing with a layer-by-layer growth mode<sup>[6]</sup> or with an island growth mode<sup>[9]</sup>. Layer-by-layer growth has been shown to be a possible growth mechanism taking into account the binding energies between layer and substrate obtained by electronic structure calculations and taking into account the surface charge neutrality<sup>[10]</sup>.

Considering all these aspects, the present work is dedicated first to a systematic investigation of the initial growth stages of epitaxial  $\text{BaTiO}_3$  films growing on  $\text{SrTiO}_3$  substrates, when deposited by PLD. Second, the obtained insight into the initial growth stages of  $\text{BaTiO}_3$  films was used to grow  $\text{BaTiO}_3/\text{SrTiO}_3$  multilayers by PLD under well-controlled growth conditions. Following these aims, the initial growth stages and the growth mechanism of epitaxial  $\text{BaTiO}_3$  films and  $\text{BaTiO}_3/\text{SrTiO}_3$  multilayers on (001)  $\text{SrTiO}_3$  substrates are studied in terms of surface morphology, crystalline orientation, microstructure and interface morphology, using a combined application of atomic force microscopy (AFM), high-resolution transmission electron microscopy (HRTEM), and x-ray diffraction (XRD).

Nucleation and film growth processes are influenced by many factors, like film-substrate lattice mismatch, kind and spacing of defects on substrates, deposition rate and temperature. Some of these aspects of nucleation and growth processes are summarized in **Chapter 2** with emphasis on the theory of epitaxial growth and on the three main mechanisms that govern epitaxial growth. This chapter also gives an introduction into the structure and properties of ferroelectric films, as well as into actual tendencies of their downscaling.

**Chapter 3** is dedicated to the discussion of the deposition method and the investigation techniques used in the present study. The experimental setup is presented, and some advantages and problems involved in the applied methods are discussed.

The experimental results and a detailed discussion of them are presented in **Chapter 4**. Atomically flat surfaces of (001)-oriented  $\text{SrTiO}_3$  substrates have been prepared by a specific etching and annealing treatment described in detail in Section 4.1. Special attention has been paid to the initial growth stages of  $\text{BaTiO}_3$  films with emphasis on the nucleation and the different growth stages as a function of the film thickness (Section 4.2.). A study of epitaxial  $\text{BaTiO}_3/\text{SrTiO}_3$  multilayers in terms of the surface morphology, the crystalline orientation, the microstructure and the film/substrate interface morphology is presented in Section 4.3. The dielectric properties of the grown films and multilayers and their possible relations with the microstructure are described in Section 4.4.

## 2 Ferroelectric oxide thin films - structure, growth, downscaling

### 2.1 Ferroelectrics - crystal structures and properties

#### 2.1.1 Overview

The phenomenon of pyroelectricity, i.e. the property by some materials of a temperature-dependent spontaneous electric dipole moment had been known for long times, before in 1880 piezoelectricity was discovered, which is defined as the generation of an electrical polarity by the application of mechanical stress. Ferroelectricity was discovered in 1921 by the observation of a ferroelectric hysteresis loop in Rochelle salt<sup>[11, 12]</sup>. Ferroelectrics are materials that belong to the pyroelectric family, showing a spontaneous polarization in the absence of an external electric field, and within a certain range of temperatures and pressures. The property that distinguishes ferroelectrics from other pyroelectrics is the switchability of their polarization, i.e. in ferroelectrics the direction of the polarization can be changed by an external electric field or by mechanical stress<sup>[13]</sup>. Ferroelectrics are usually divided into separate regions (domains) which differ in the direction of the spontaneous polarization. Ferroelectric crystals can have structures with different degrees of complexity, from a most simple unit cell like that of the cubic perovskite structure (e.g.  $\text{BaTiO}_3$ ) - to rather complex unit cells like that of the layered perovskite structures (e.g.  $\text{SrBi}_2\text{Ta}_2\text{O}_9$ ) (Fig. 2.1).

The very important group of ferroelectrics known as perovskites is named after the mineral  $\text{CaTiO}_3$ . The ideal perovskite structure of the general formula  $\text{ABO}_3$  is cubic (space group  $\text{Pm}\bar{3}\text{m}$ ) with the A cations situated at the corners of the cube (A - monovalent or divalent metal), the B cations at the center (B - tetravalent or pentavalent metal), and the  $\text{O}^{2-}$  anions at the centres of the faces. The  $\text{BO}_6$  octahedra are corner-linked.

The first discovered ferroelectric with a perovskite structure was  $\text{BaTiO}_3$ , the discovery of which was largely a consequence of war-time research in electronic components, particularly capacitors, cf. [14].

The polarization states in a ferroelectric crystal are due to the displacement of positive metallic and negative oxygen ions in opposite directions (Fig. 2.2). This displacement reduces the symmetry of the crystal from cubic to tetragonal. Thermodynamically stable, these states can be switched from one to the other by applying an external electric field larger than the coercive field  $E_c$ . As a rule,

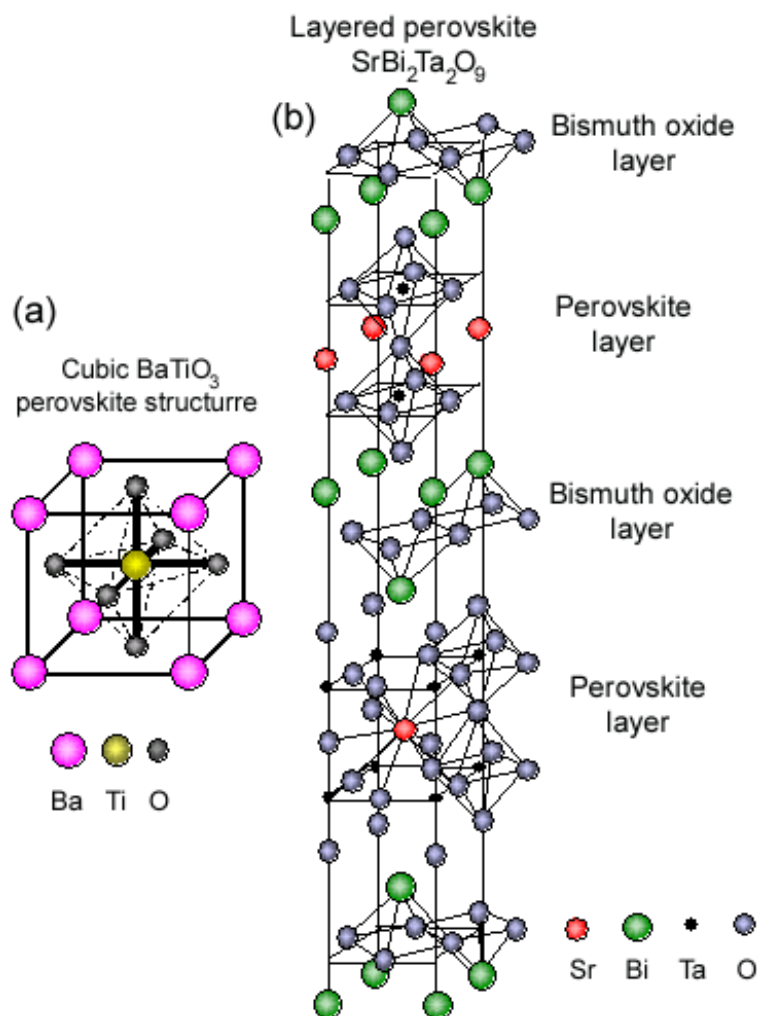


*Fig. 2.1: Unit cells of two ferroelectric crystals: (a) the cubic perovskite structure ( $\text{BaTiO}_3$ ) and (b) the layered perovskite structure ( $\text{SrBi}_2\text{Ta}_2\text{O}_9$ ).*

ferroelectrics are transforming from the ferroelectric phase at low temperature to a non-ferroelectric phase at the higher temperature  $T_c$ .  $T_c$  is usually called the Curie temperature.

Epitaxial oxide thin films are potentially important for the electronics industry because they may exhibit a large number of useful properties (Fig. 2.3). The ferroelectric  $\text{BaTiO}_3$  is one of the most promising of these materials.

### 2.1.2 Barium Titanate

The origin of ferroelectricity in  $\text{BaTiO}_3$  was studied since 1950. It has been attributed to long-range dipolar forces which, due to the Lorentz local effective field, tend to destabilize the high-symmetry configuration favored by the local forces<sup>[16]</sup>. Correspondingly, the sensitivity of ferroelectrics to their composition and to defects, electrical boundary conditions and pressure arises from a balance between the long-range Coulomb forces and the short-range repulsions<sup>[17]</sup>.

$\text{BaTiO}_3$  is paraelectric (non-polar) and of the proper cubic perovskite structure at high temperatures. The crystal structure consists of a set of  $\text{TiO}_6$  octahedrons sharing the oxygen atoms, and with the Ba ions in between the octahedrons, at the centers of the cubic unit cell [see Fig. 2.1(a)].  $\text{BaTiO}_3$

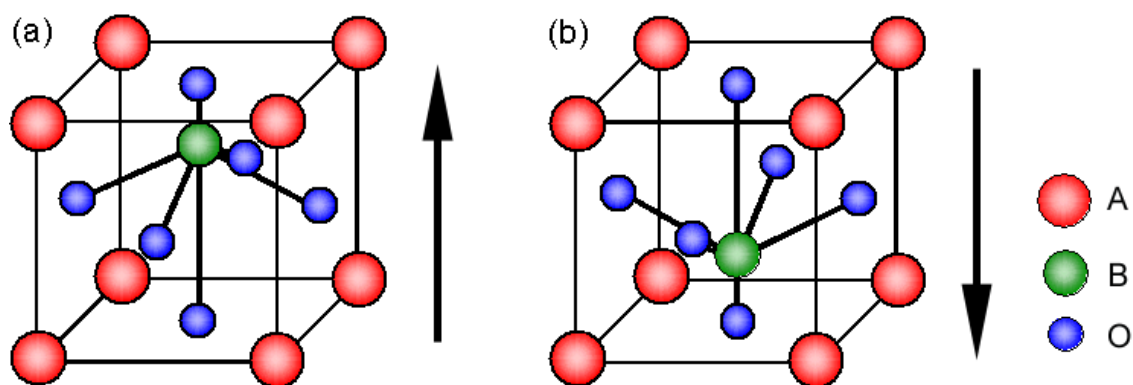


Fig. 2.2: Unit cell of a  $ABO_3$  ferroelectric with polarization up (a) and down (b).

has three ferroelectric phase transitions: cubic to tetragonal at 393 K, tetragonal to orthorhombic at 278 K, and orthorhombic to rhombohedral at 183 K. The ferroelectric distortions involve small displacements in the cations relative to the anions, leading to a net dipole moment per unit volume - the spontaneous polarization.

Macroscopically, ferroelectrics can be described in a thermodynamic context writing the Gibbs free energy:

$$dG = -SdT + x_i dX_i - D_i dE_i \quad (2.1)$$

where  $G$ ,  $S$ ,  $T$ ,  $E$  and  $D$  are the Gibbs free energy, the entropy, the temperature, the electric field, and the electric displacement ( $D = \epsilon_0 E + P$ ,  $P$  being the polarization), and  $x_i$  and  $X_i$  are the components of strain and stress. One of the thermodynamic theories of ferroelectricity is the one by Devonshire, developed in the 1950ies based on the Ginzburg-Landau theory, with specific reference to BaTiO<sub>3</sub>, describing both polar and non-polar phases by the same energy function<sup>[18, 19]</sup>. By expanding the free energy as a function of polarization and strain and making reasonable assumptions about the coefficients, Devonshire was able to calculate various crystal transitions, and to deduce, e.g. dielectric constant, crystal strain, internal energy, and self polarization as functions of temperature. The simple polynomial form of the Gibbs free energy is expressed in powers of displacement:

$$G = \frac{1}{2}\alpha D^2 + \frac{1}{4}\gamma D^4 + \frac{1}{2}\delta D^6 \quad (2.2)$$

where  $\alpha$ ,  $\gamma$ , and  $\delta$  are coefficients. Only one of these coefficients is temperature dependent (for  $\chi$  and  $C$ , see next page):

$$\alpha = \frac{1}{\chi} = \frac{(T - T_c)}{C} \quad (2.3)$$

The ferroelectric transitions in BaTiO<sub>3</sub> are first-order phase transitions and they occur from the paraelectric phase, which is determined by the point-symmetry group  $O_h(m3m)$  as follows:

$$O_h(m3m) \rightleftharpoons C_{4v}(mm4) \rightleftharpoons C_{2v}(mm2) \rightleftharpoons C_{3v}(3m) \quad (2.4)$$

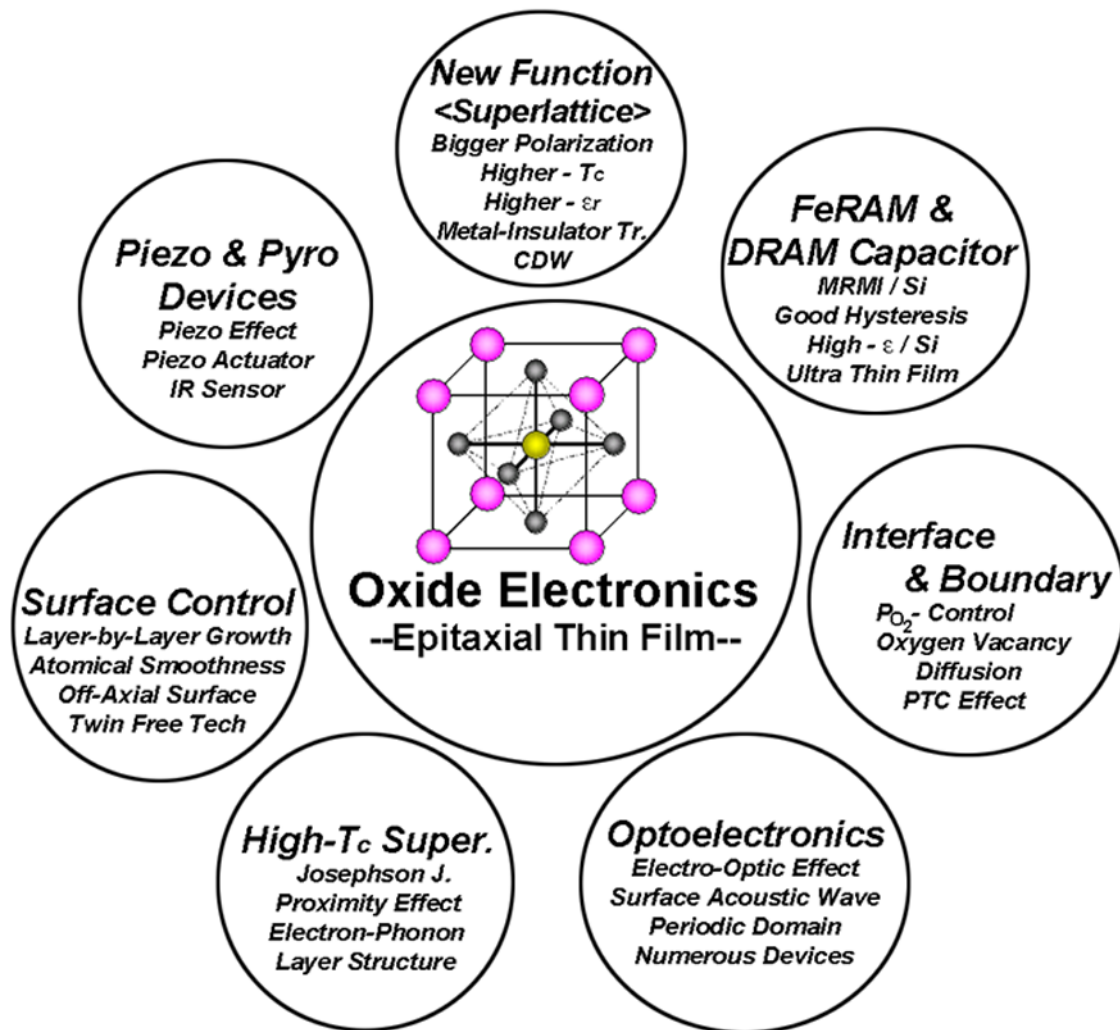


**Fig. 2.3:** Application potential and fundamental technical terms of epitaxial oxide thin films, according to ref. [15].

where  $O_h$ ,  $C_{4v}$ ,  $C_{2v}$ , and  $C_{3v}$  are the crystallographic symbols for the cubic, tetragonal, orthorombic and rhombohedral phases, respectively.

The temperature dependence of the dielectric susceptibility,  $\chi$  (Fig. 2.4) is described by the Curie-Weiss law<sup>[20]</sup>:

$$\chi = \frac{C}{T - \theta} \quad (2.5)$$

where  $C$  is the Curie constant (for  $BaTiO_3$ ,  $C$  varies from  $1.56 \cdot 10^5$  degrees to  $1.73 \cdot 10^5$  degrees), and  $\theta$  in the Curie-Weiss temperature. For  $BaTiO_3$ ,  $\theta$  varies within  $10^\circ$  below the Curie temperature. In general, the Curie temperature,  $T_c$ , is considered to be at  $120^\circ C$ . Above the Curie temperature,  $BaTiO_3$  is a cubic crystal.

At the transition temperatures, the dielectric constant in all the crystallographic directions has a maximum<sup>[21]</sup> as shown in Fig. 2.5.

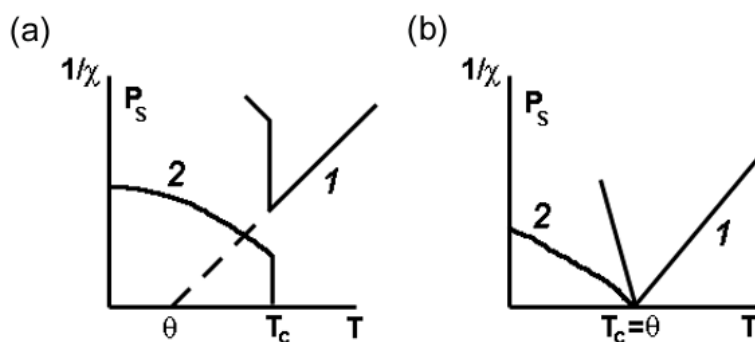


Fig. 2.4: Temperature dependence of the dielectric susceptibility (1) and the spontaneous polarization (2) in: (a) first-order phase transition and (b) second-order phase transition, according to ref.<sup>[20]</sup>.

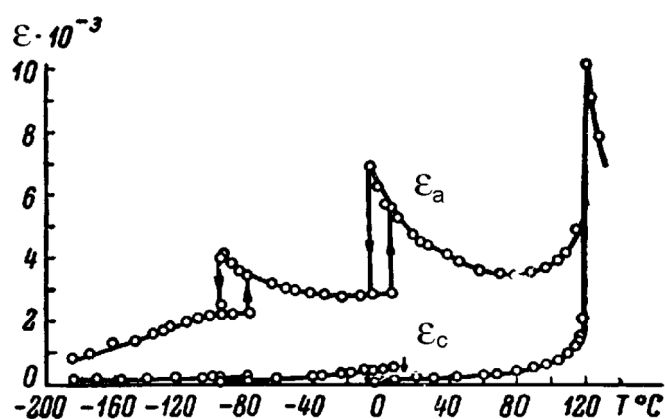


Fig. 2.5: Temperature dependence of dielectric constants  $\epsilon_a$  and  $\epsilon_c$  of a  $\text{BaTiO}_3$  single crystal, according to ref.<sup>[21]</sup>.

Insulating  $\text{BaTiO}_3$  can become semiconducting by annealing in a reducing atmosphere or by doping with suitable ions. In case of doping, substitution can occur either at the Ba sites with a trivalent element such as  $\text{Y}^{3+}$  or  $\text{La}^{3+}$  or at the Ti sites with a pentavalent element such as  $\text{Nb}^{5+}$ <sup>[22]</sup>. Semiconducting doped  $\text{BaTiO}_3$  ceramics are well known for the positive temperature coefficient of resistivity. Also, semiconducting doped  $\text{BaTiO}_3$  films could be of interest as top electrodes for high- $k$   $\text{BaTiO}_3$ -based capacitors. This implies, however, the ability of finely controlling the oxidation and doping level in the top layer, while not degrading the buried insulating high- $k$  layer.

### 2.1.3 Strontium Titanate

In the 1960ies and 1970ies  $\text{SrTiO}_3$  was the subject of extensive research activities. It was the first material for which it was demonstrated that the strong increase of the static dielectric constant at low temperatures is associated with the softening of a long-wavelength transverse optic phonon mode<sup>[23]</sup>.  $\text{SrTiO}_3$  has been studied extensively because of its electronic properties and structural behavior. The important electronic properties include semiconductivity and superconductivity. At high temperatures the dielectric constant follows a Curie-Weiss law suggesting a ferroelectric phase transition at about 35-40 K<sup>[24]</sup>. The superconductivity of  $\text{SrTiO}_3$  was discovered in 1964 by Schooley *et al.*<sup>[25]</sup> showing that superconducting transitions occurred within a range of less than 0.1 K at about 0.25 K.

$\text{SrTiO}_3$  has a perovskite structure and is one of the few titanates which is cubic at room temperature. There is a structural phase transition from cubic to tetragonal at 110 K and to orthorhombic at

65 K<sup>[26]</sup>. In the cubic cell of SrTiO<sub>3</sub>, Sr<sup>2+</sup> ions are surrounded by eight O<sup>2-</sup> ions and six Ti<sup>4+</sup> ions. They occupy the larger space at the center of the cubic cell (Fig. 2.6).

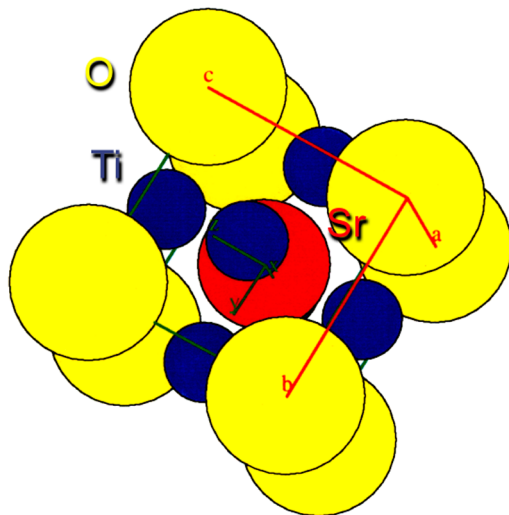


*Fig. 2.6: SrTiO<sub>3</sub> unit cell structure (cubic, at room temperature, with  $a_c = 0.3905$  nm) seen along the [120] direction.*

The Curie temperature of SrTiO<sub>3</sub> is close to 40 K and it has been shown conclusively that quantum fluctuations suppress long-range ferroelectric order at low temperatures<sup>[27]</sup>.

SrTiO<sub>3</sub> is also important from a technological point of view due to its large dielectric constant and its large dielectric breakdown field which make it a potential candidate for storage capacitor cells in DRAMs<sup>[28]</sup>. Its large dielectric nonlinearity at low temperatures is a desirable property for tunable filters or phased array antennas<sup>[29, 30]</sup>. Also, the structural compatibility with high-temperature superconductors like YBa<sub>2</sub>Cu<sub>3</sub>O<sub>7- $\delta$</sub>  leads to an increased interest in thin film microwave applications<sup>[31]</sup>.

## 2.2 Film nucleation and growth

Thin solid films are formed from the vapor phase on a substrate by a process which usually involves the nucleation and growth of individual islands (or clusters). In the initial stage, small nuclei are formed from individual atoms or molecules. Then, as time progresses, these islands grow, eventually coalesce, and finally form a continuous film which then grows in thickness<sup>[32]</sup>. Depending on size, shape, area density and growth rate of the individual islands, a rich variety of morphologies and structures of thin films may result.

Some of the important processes during nucleation and growth of thin films on a substrate are schematically shown in Fig. 2.7. Atoms arrive from the vapor phase and they are adsorbed on the surface. The incident rate is mostly dependent on the deposition parameters. Adsorbed atoms can subsequently diffuse on the surface with a diffusion coefficient which strongly depends on the substrate temperature. Adsorbed atoms can either re-evaporate or form clusters which subsequently may develop into large clusters. Only above a critical size clusters are stable (“critical nucleus”). Single



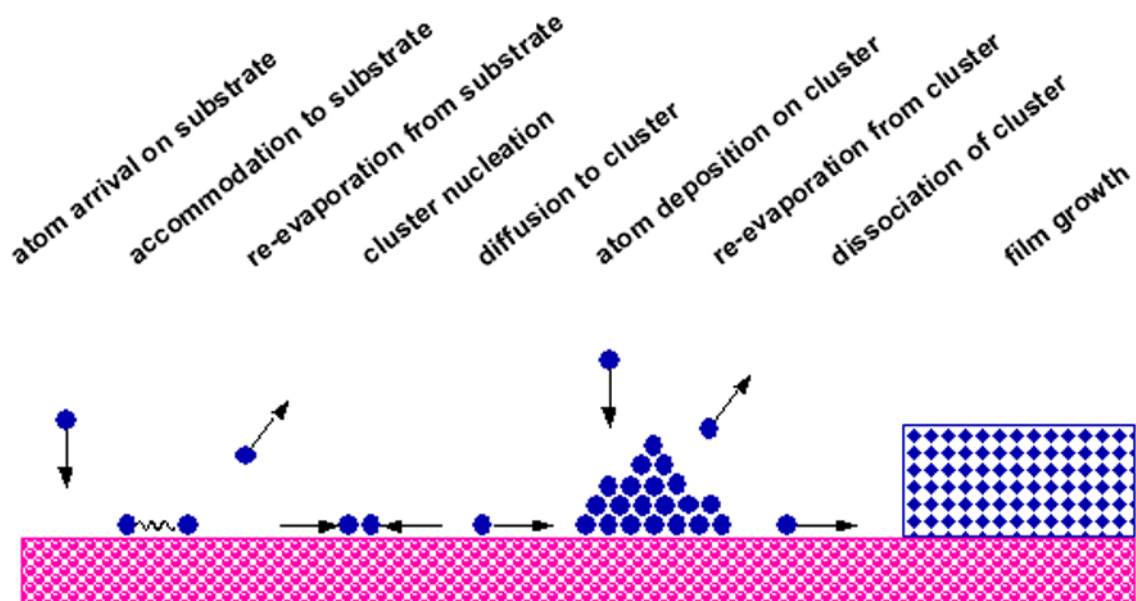


**Fig. 2.7:** Processes in the nucleation and growth of crystals on a substrate.

atoms can diffuse across the substrate to join stable clusters, or they can impinge directly on the grown clusters and become incorporated into them. The balance between growth and dissolution processes for a given cluster is governed by the total free energy of the cluster, relatively to an assembly of individual atoms.

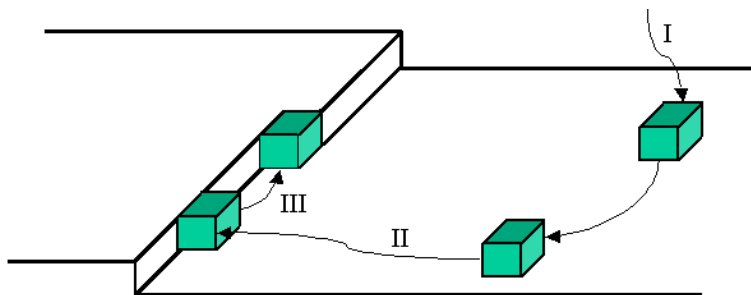


**Fig. 2.8:** Sequence of the incorporation of atoms at a kink site of the surface, according to ref. [33].

Optimal binding forces exist in the case of an atom positioned on surface terraces, at ledges on the surface terraces or at kinks at the ledges<sup>[33]</sup>. In addition, atoms may migrate along the surface terrace until they reach a kink site at the ledge or else may be desorbed (Fig. 2.8). Since the concentration of ledges varies with the orientation of crystal faces, these processes may be different on different faces of the surface, under the same experimental conditions. Faces of different orientation have different surface structures<sup>[35]</sup> (Fig. 2.9). Atomically flat faces, such as the (100) face of simple cubic structures, do not show steps under ideal conditions. They are called singular faces. Faces other than singular ones show various degrees of ledge density, depending on their orientation. Faces differing by small angles from singular faces are called *vicinal faces*. They contain large segments of singular faces interrupted by monatomic steps. The step density is small in this case. Faces having a high density of steps, which increases with increasing angle from the singular faces, are called nonsingular faces. Their steps show a large number of kinks which result in a rough surface. Interfaces corresponding to

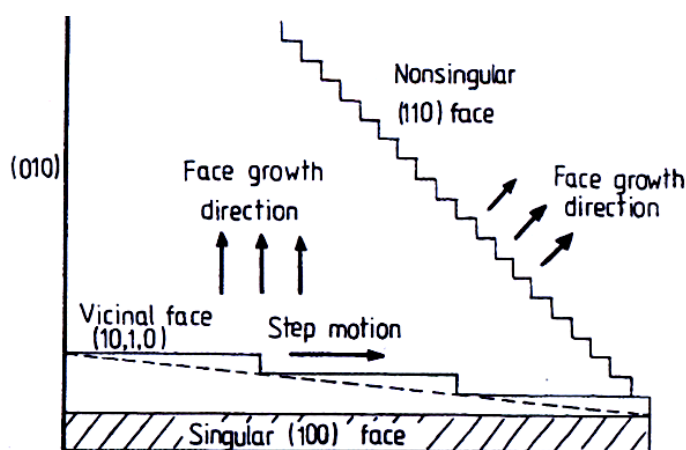


*Fig. 2.9: Cross-sectional view of faces with different orientation of a simple cubic structure, according to ref. [34].*

the singular, vicinal and nonsingular faces are referred to as sharp interfaces. Their energy is usually anisotropic because it depends on the density of steps (i.e. on the crystallographic orientation). For a singular face the surface energy has a sharp minimum, while for nonsingular faces it is high.

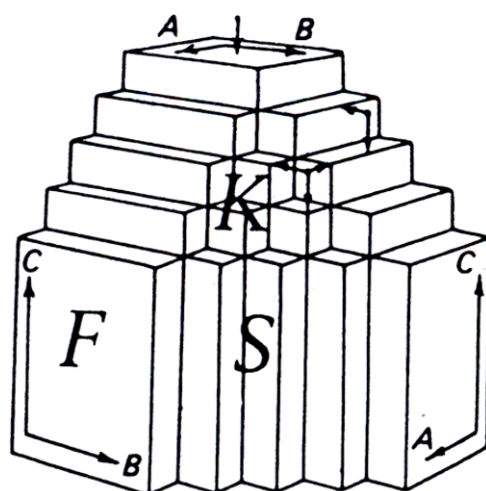


*Fig. 2.10: Classification of faces into flat (F), stepped (S) and kinked (K) faces, according to Hartman[36].*

Hartman<sup>[36]</sup> introduced a classification of crystal faces into flat (F), stepped (S) and kinked (K) faces. In the ideal case, F faces are atomically flat, S faces are composed of ledges, and K ledges consist of kinks only (Fig. 2.10). The essential requirement for the growth of a crystal is the presence of a sufficient number of kinks on its faces. K faces are entirely composed of kinks, but on S and F faces kinks are also provided by statistical fluctuations. Since S faces are composed of ledges, the kink density on them is expected to be much higher than on F faces. A natural consequence of the surface structure is that the F faces are the slowest growing faces, S faces grow at a faster rate than the F faces, and K faces are the fastest growing faces, so that they are usually absent in the growth morphology. Microscopically, F faces remain smooth, while S faces show parallel striations which appear to start from one of the neighboring F faces. Growth of a perfect F face can take place by incorporation of atoms at kinks of the existing ledges. When a monolayer grows out, surface nucleation occurs again in order to provide the source of repeatable steps. The process of surface nucleation and elimination of the ledges originating from there thus repeats discretely.

The formation of three-dimensional (3D) clusters is usually discussed in terms of reduction in the Gibbs free energy of the system. Corresponding to the given supersaturation of the vapor phase and to the temperature, there is a critical value of the free energy reduction when 3D clusters of critical sizes are formed. Only those clusters which have a size greater than the critical one grow by incorporation of atoms at energetically favorable sites, such as a ledge on their surface or on a kink at a ledge. Generally the involved processes, e.g. transport of the atoms or even of small clusters along the surface, or their incorporation at ledges can be controlled by the growth conditions.

While the roles of faces, steps, and kinks have been described here for the case of 3D growth of a cluster, or of a crystal, these roles are also similarly relevant in the case of the growth of a thin film on a substrate, when the surface of the latter involves faces of different morphology, terraces, or kinked steps. Therefore the morphology of the substrate is most relevant to the process of thin film growth, particularly in case of epitaxial growth.

## 2.3 Epitaxial growth

Epitaxy is commonly defined as the oriented growth of a crystalline material on a single crystal surface<sup>[37]</sup>. The first systematic study of epitaxy was published in 1928 by Royer<sup>[38]</sup>, then in 1949 Frank and van der Merwe proposed a theory of epitaxy based on the concept of the pseudomorphism<sup>[39]</sup>.

The epitaxial orientation is generally described in terms of the Miller indices of crystal planes and directions. Epitaxial growth is defined by the nature and strength of the chemical bonds of both film and substrate, and by the different lattice parameters. A measure of the latter is called *lattice mismatch*,  $f$ , between the crystal lattices of the film and the substrate, defined as:

$$f = \frac{a_{\text{film}} - a_{\text{substrate}}}{a_{\text{substrate}}} \quad (2.6)$$

where  $a_{\text{film}}$  and  $a_{\text{substrate}}$  are the lattice constants of the deposited material and the substrate, respectively.

In general terms, the epitaxial orientation is determined by the condition of a minimum of the free energy of the system. Epitaxial growth is classified in: (i) *homoepitaxy* - when film and substrate consist of the same material, and (ii) *heteroepitaxy* - when they are different. The epitaxial orientation of the film depends on the structure, i.e. the crystal planes which are coming in contact, and on the nature of the chemical bond across the epitaxial interfaces. On an empirical base, Royer<sup>[38]</sup> formulated the following rules:

1. Crystal planes in contact should have the same symmetry and close lattice parameters (the difference should not be greater than  $\approx 15\%$ );
2. Both crystals should have the same nature of the chemical bonds;

3. In the case of ionic crystal, the alternation of ions with opposite signs across the interface should be preserved. The atoms of the deposited material can be bound more loosely or more tightly to the substrate atoms than to the atoms of the same crystal. The chemical potential of the film will vary from monolayer to monolayer due to the elastic strain<sup>[40]</sup>.

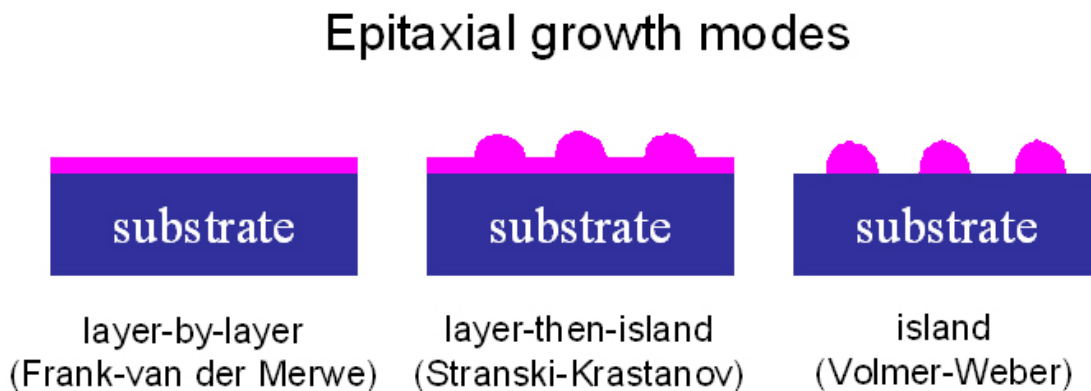


**Fig. 2.11:** *The main epitaxial growth modes.*

Three epitaxial growth modes<sup>[35]</sup> have been identified: the **layer-by-layer (Frank-van der Merwe)** growth, e.g., in the case of a very thin pseudomorphic layer, or in case of almost perfectly lattice-matched materials; the **island (Volmer-Weber)** growth, and the **layer-then-island (Stranski-Krastanov)** growth, mainly for lattice-mismatched materials (Fig. 2.11).

The classical theory of film nucleation and growth states that the “selection” of one of these growth modes by a specific substrate-film system depends on thermodynamics, i.e. on the surface energies of both film and substrate, and on the film-substrate interface energy<sup>[41]</sup>.

The relation between nucleation processes and the occurrence of epitaxy is not yet completely clear. However, in the island growth mode the experimental evidence strongly suggests that epitaxy is a postnucleation phenomenon involving rotation, migration, and rearrangement of “stable” clusters. In the layer-by-layer growth mode, the epitaxy can be “destroyed” by influencing the growth process at a later stage incorporating impurities or defects into the growing film. The impurities can affect the nucleation kinetics or the subsequent growth by reducing the binding energy at kink sites, or conceivably by favouring twin or stacking fault formation. The initial layers are more or less forced to be related epitaxially to the substrate, provided that surface diffusion is sufficiently rapid, so that the growth of amorphous layers should not occur.

In simple terms, the growth can be considered as dependent on two competing forces<sup>[42]</sup>: one of the film-crystal, which has the tendency to keep its own structure, the other of the substrate-crystal, which tends to enforce its structure onto the film. The “compromise” position of the film atoms will eventually depend on the relative strength of these two competing forces via the film-substrate misfit, the relative bond strength, the epitaxial film thickness and the growth temperature. In many film growth techniques, the deposition and growth rates are low enough and the relevant atomic processes

are fast enough so that quasi-equilibrium prevails. In this case, the governing principle is the minimum of the free energy which is strongly dependent on the interface misfit. The growth mode depends also on the temperature and the rate of deposition. For example, the time between consecutive localized arrivals of atoms can be insufficient for them to reach positions needed for an equilibrium state, so that the atoms almost stay at their arrival points, except for small displacements of the order of one atomic distance or less.

If a 3D cluster is large enough to be treated as a continuous solid, its free energy with respect to dissociation processes (see Fig. 2.7) can be written using Green's notation<sup>[43]</sup> as follows:

$$\Delta G = a_1 r^2 \Gamma_{c-v} + a_2 r^2 \Gamma_{s-c} - a_2 r^2 \Gamma_{s-v} + a_3 r^3 \Delta G_v \quad (2.7)$$

where it is considered that the cluster has a surface area  $a_1 r^2$  in the vapor phase, a contact area  $a_2 r^2$  with the substrate and a volume  $a_3 r^3$  ( $a_i$  - constants of geometry depending of the shape of the nuclei,  $r$  - cluster radius). The  $\Gamma$ 's are the interface energies between the substrate, the condensate and the vapor phase. The change in volume free energy on condensation of the cluster,  $\Delta G_v$ , is given by the following relation:

$$\Delta G_v = \frac{kT}{\Omega} \ln \frac{P}{P_e} = \frac{kT}{\Omega} \ln(\zeta) \quad (2.8)$$

where  $\Omega$  is the volume of an adatom,  $k$  is Boltzmann's constant,  $T$  is the absolute temperature,  $P$  is the pressure of arriving atoms,  $P_e$  is the equilibrium vapor pressure of the film atoms, and  $\zeta$  is the supersaturation. An expression for the critical cluster size  $r^*$  can be obtained by maximizing  $\Delta G$  in equation 2.7:

$$\frac{\partial(\Delta G)}{\partial r} = 0 \implies r^* = -\frac{2\Gamma_{c-v}}{\Delta G_v} \text{ and } \Delta G^* = \frac{16\pi\Gamma^3}{3(\Delta G_v)^2} \quad (2.9)$$

As it can be seen in Fig. 2.12, clusters larger than the critical size  $r^*$  can lower their free energy by continuing to grow, while clusters with  $r < r^*$  will dissolve.

The difference in the growth mechanism is given by the sign of the following inequality:

$$a_1 \Gamma_{c-v} + a_2 \Gamma_{s-c} - a_2 \Gamma_{s-v} \quad \left\{ \begin{array}{l} \leq 0 \text{ , layer-by-layer growth} \\ \text{or} \\ > 0 \text{ , island growth} \end{array} \right. \quad (2.10)$$

The positive inequality 2.10 is automatically satisfied for 3D-island growth. If it is not satisfied, it will be energetically more favorable for the film to form a single layer on the substrate, leading to full layer-by-layer growth. In the simplest case, the condition can be written as follows:

$$\frac{\Gamma_{s-v}}{\Gamma_{c-v}} - \frac{\Gamma_{s-c}}{\Gamma_{c-v}} \geq 1 \quad (2.11)$$

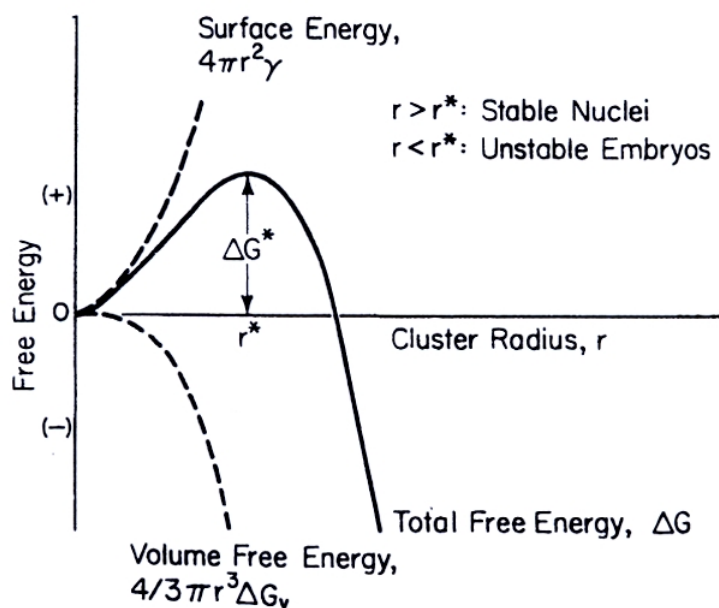


Fig. 2.12: Diagram of the free energy versus the radius of film nuclei<sup>[43]</sup>.

Two-dimensional (2D) layer-by-layer growth is the process in which the coalescence of the islands with a height of one unit cell exceeds the nucleation of adatoms on top of these islands. This mode results in a smooth growth of films with a low density of structural defects.

In the opposite case, the island growth mode, small 3D clusters nucleate on the substrate. Different islands are characterized by different growth rates, resulting in a rough surface.

An intermediate case, the Stranski-Krastanov growth mode, consists of an initial 2D growth and a subsequent transition to 3D island growth. The 2D part of the film is usually formed by one or few monolayers, which then act as a substrate for subsequent 3D nucleation. The initial layers have typically a height of 1 to 5 monolayers. The most obvious feature that could cause 3D cluster nucleation on complete layers is an increase of stress with increasing layer thickness due to mismatched lattice spacings. In cases for which the 3D nucleation occurs at a layer thickness of one or two monolayers, strong chemical bonding forces between the film and the substrate could be involved and these will alter the surface energy of the initial layers.

No *ab initio* molecular dynamic method has so far been applied to metal-oxide interfaces to determine the growth mode, because it would require too much memory and calculation time. Several molecular dynamic approaches, making use of empirical potentials have derived trends in the wetting, the growth, and the nucleation modes of clusters on surfaces. Among them, Grabow and Gilmer<sup>[44]</sup> have obtained a phase diagram for the growth modes as a function of parameters that characterize the interface: the interfacial coupling and the lattice misfit parameter between the film and the substrate (Fig. 2.13). They found out that the Volmer-Weber growth is restricted to systems in which the film-substrate interaction is weak. Beyond a critical value, a layer-by-layer growth takes place. However, the lattice misfit induces stresses in the film which destroy its thermodynamic stability as lattice misfit increases. Beyond a given thickness, ranging from 2 to 5 monolayers, which is an increasing function

of the inverse of the lattice misfit, clusters are formed. This is a Stranski-Krastanov growth mode. Layer-by-layer mode is only seen for values of film-substrate interaction ( $W$ ) larger than one, i.e. under conditions when the lattice misfit ( $\eta$ ) is very low<sup>[45]</sup>. For clusters of large size, there is no clear criterion for obtaining perfect epitaxy. The influence of surface defects, such as the surface roughness or the oxygen deficiency on the film spreading is not very well understood.

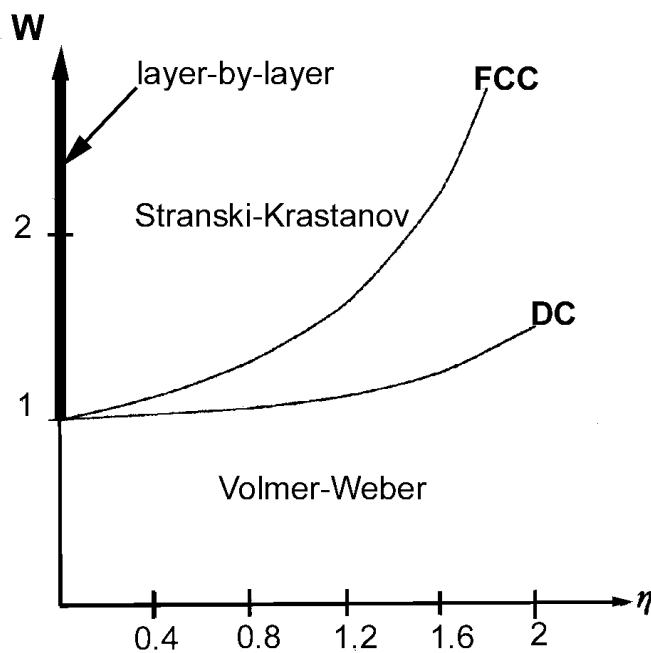


**Fig. 2.13:** Phase diagram for three growth modes: layer-by-layer growth, layer-then-island growth, and island growth, as a function of the interfacial coupling,  $W$ , and the lattice misfit,  $\eta$ , between the film and the substrate (FCC - face centred cubic, DC - diamond cubic), according to refs.<sup>[45, 44]</sup>. The film and the substrate have the same lattice structure.

Conditions which influence the growth mode were summarized by Markov and Stoyanov<sup>[46]</sup> taking into account the binding energies, the substrate temperature, the deposition rate, and the crystallographic orientation of the substrate, as follows:

1. When the bonding at the interface is weaker than the bonding in the film itself, the formation of 3D islands rather than monolayers is favoured.
2. High substrate temperatures favour the growth of 3D islands either on the substrate (island growth mechanism) or on one or several stable monolayers already deposited on the substrate (layer-then-island growth mechanism). In addition, the higher the temperature, the larger is the height of the 3D islands.
3. Higher deposition rates favour the layer-by-layer growth.
4. The larger the mismatch, the higher is the tendency towards island growth.
5. The more densely packed the substrate plane, the flatter the 3D islands will grow.

Theoretical and experimental efforts have resulted in a better understanding of epitaxy in the last decades. Nevertheless, a residue of discrepancy between interface theory and related experiments is likely to remain in the foreseeable future for the following reasons<sup>[42]</sup>:

(i). Interface theories are equilibrium theories and describe the most favourable final configuration of the atoms forming the transition region, depending on the parameters of the given system. But they only rarely give information about the way in which a real physical system can achieve that state of equilibrium. Therefore, it is necessary to experimentally investigate how a given system of real crystals attains its equilibrium state. This involves growth kinetics and reactions of lattice imperfections.

(ii). Many of the parameters which are essential for a theoretical study, i.e. the strength of the interface interaction, the surface topography of the substrate or the special nucleation and growth kinetics of the deposited film, are either unknown or are not taken into account.

The structure of the interface, and its properties, depend essentially on four parameters: (a) the amount of the misfit between the two epitaxial materials, (b) the ratio  $t_{film} / t_{substrate}$  ( $t_{film}$  is the film thickness, and  $t_{substrate}$  is the substrate thickness), (c) the strength of the interaction between the substrate surface and the first atomic layers of the deposited film, (d) the surface condition of the substrate and details of the growth kinetics of the first deposited layer. This includes also diffusion processes and solid state reactions in the interface region and their influence on the strength of interaction between the epitaxial materials.

Pseudomorphic growth is the simplest lattice-fitting mechanism and it occurs due to the existence of strains in the first deposited layers. However, if the bonding force between the substrate and the film is sufficiently weak, the film will grow with its own equilibrium lattice constant, and the substrate will act in such cases simply as a flat carrier. If so, there will be only a relatively weak orientation of the deposit nuclei with respect to the crystallographic directions of the substrate, and imperfections arising during film growth will be related almost exclusively to the coalescence of the individual nuclei.

During the past decade there has been much interest in growing epitaxial multilayers of oxides. The thickness of each layer in the multilayer tends to be in a range of tens of nanometers, while the overall thickness of the multilayer may vary from 1  $\mu\text{m}$  to less than 100 nm. Many promising ferroelectric-based devices, such as ferroelectric field transistors and memory capacitors, involve heterostructures and multilayers. The performance of the devices and the ferroelectric properties such as polarization, fatigue, imprint and leakage current are closely related to the interfaces between the constituent layers and to the overall microstructure of the films. Therefore it is desirable that each constituent layer is grown epitaxially and smoothly to minimize any degradation at the interfaces and to reduce the density of defects in the heterostructures or multilayers. A knowledge of the growth mechanisms and surface microstructures of the individual constituents is thus very important for controlling the interfaces and eventually the interface-determined properties of the multilayers.



## 2.4 Scaling down ferroelectric thin films

Ferroelectric materials offer a wide range of properties which can be used in microsystems technology and nanotechnology within memories, capacitors, detectors, sensors, and filtering devices. Nanotechnology is the science and engineering of creating materials, functional structures, and devices on a nanometer scale. What is interesting in downsizing materials to a nanoscale is that the fundamental physical and chemical properties of materials may surprisingly be altered as their constituent grains or other entities are decreasing to a nanometer size. Nowadays, nanotechnology is a very common term and a fashionable subject covering a wide range of activities, i. e. fabrication and exploitation of materials, devices etc., from ultra-precision engineering and fine-line lithography through nanostructured materials to the manipulation of biological molecules. There is a strong overlap with the subject of microsystems technology, whereby systems incorporating sensing, signal processing, actuation and communication are or will be integrated into a single microengineering package<sup>[47]</sup>.

Thin ferroelectric films of around 1  $\mu\text{m}$  thickness are ideal for many sensor applications. Such films have been fabricated by sputtering<sup>[48]</sup>, metal organic chemical vapor deposition<sup>[49]</sup>, and various chemical solution deposition methods<sup>[50]</sup>. A critical issue in their manufacturing is the growth temperature. However, a relatively high energy is involved in rf sputtering and there can be an undefined degree of plasma heating of the substrate. The low energy sol-gel method involves low growth temperatures (500 °C) and very thin (15 nm) individual layers<sup>[51]</sup>. Ultimate applications lie in the fields of nanoscale fabrication and information storage, particularly in nonvolatile memory capacitor cells. The ability to scale down ferroelectric capacitor sizes to below 1  $\mu\text{m}^2$  is limited by the following physics-related issues<sup>[52]</sup>: (i) the dependence of the switching speed on capacitor size, (ii) the dependence of the coercive field on frequency, (iii) the dependence of the polarization on the applied voltage at lower values, and, last but not least (iv) by possible size and interface effects, as the occurrence of polarization decrease or imprint effects at very small sizes<sup>[53]</sup>.

Micropatterning is one of the most important technologies in the fabrication of very large scale integrated circuits. In ordinary patterning processes, homogeneous thin films of the required materials are first deposited on substrates. Resist patterns are then formed on the target films using lithography techniques with UV light or an electron beam. Finally, the target films without resist films are removed by dry-etching using reactive gases. With shrinking dimensions side-wall damage may become important since the fabricated features will have increasingly high aspect ratios and high surface-to-volume ratios. In the last years, several patterning methods have been developed to fabricate structures of reduced sizes of ferroelectric thin films:

1. A selective deposition technology by electron beam induced surface reaction<sup>[54]</sup> was used for a micropatterning process of oxides such as high-Tc superconductors<sup>[55]</sup> and ferroelectric materials<sup>[56]</sup>. E.g., using liquid sources square  $\text{Bi}_4\text{Ti}_3\text{O}_{12}$  structures were scaled down to 1  $\mu\text{m}$  in lateral size. The advantage of this method is that each precursor micropattern of submicron size is crystallized into a single crystal.

2. Reactive ion etching was used to obtain  $0.25 \mu\text{m}^2$  ferroelectric capacitors made of  $\text{Pb}(\text{Zr},\text{Ti})\text{O}_3$  [57]. The main problem of this technique is the side-wall redeposition of etch products which is difficult to remove in a manufacturing environment.
3. Focused ion-beam patterning was used for thin film based multilayers, such as  $\text{Pb}(\text{Nb}_x\text{Zr}_y\text{Ti}_z)\text{O}_3$  in the range of  $0.25\text{-}0.017 \mu\text{m}^2$  area [58]. The capacitor quality is strongly influenced by the beam current and the main disadvantage is that it is too slow for production.
4. Electron-beam direct writing was successfully applied to prepare regular  $\text{SrBi}_2\text{Ta}_2\text{O}_9$  cells as well as  $\text{Pb}(\text{Zr}_{0.70}\text{Ti}_{0.30})\text{O}_3$  cells with lateral sizes down to  $100 \text{ nm}$  [52].

All the above mentioned micropatterning methods represent non-standard deposition techniques. An ultimate challenge in preparing sub-micron ferroelectric cells is to use the conventional techniques which are normally used for fabrication of ferroelectric thin films.

The present study is dedicated to the investigation of the growth mode of  $\text{BaTiO}_3$ , the knowledge of which can be considered as a prerequisite to grow ferroelectric  $\text{BaTiO}_3$  cells of small lateral sizes or to grow very thin, smooth  $\text{BaTiO}_3$  layers within multilayer structures. A Stranski-Krastanov growth mode has been identified. A conventional PLD method was used successfully to grow epitaxial  $\text{BaTiO}_3$  thin films with thicknesses decreasing down to  $1 \text{ nm}$ . Up to now, strain relaxation and island formation in the Stranski-Krastanov growth mode have been studied in great detail in semiconductor systems such as  $\text{Ge}/\text{Si}$  or  $(\text{In},\text{Ga})\text{As}/\text{GaAs}$  grown by molecular beam epitaxy (MBE) [59]. The transition from the 2D growth to the 3D growth of  $\text{Ge}$  islands on  $\text{Si}$  (100) substrates, as well as of  $(\text{In},\text{Ga})\text{As}$  islands on  $\text{GaAs}$  (100) substrates, has been discussed in terms of a dislocation-free Stranski-Krastanov growth mode [60, 61]. In the present work, the Stranski-Krastanov growth mode is studied for the first time in case of perovskites. The obtained results are likely to deepen the understanding of the growth of thin perovskite films. They are particularly significant in view of actual efforts to grow artificial superlattices (epitaxial superstructures) involving very thin individual layers of  $\text{BaTiO}_3$  and/or  $\text{SrTiO}_3$ . For example, epitaxial  $\text{BaTiO}_3/\text{SrTiO}_3$  artificial superlattices with a thickness of the individual layers in the order of  $5$  to  $10 \text{ nm}$  are currently studied aiming at either an improvement of the ferroelectric properties or the achievement of new dielectric properties. Optimizing these properties certainly requires a good understanding of the initial growth mode of these very thin individual layers, to which the present work should be able to contribute.

# 3 Experimental and characterization methods

## 3.1 Pulsed laser deposition

### 3.1.1 Introduction and principle

A number of techniques are now available to produce high quality thin films of ferroelectrics (see Table 3.1). Thermal evaporation (TE) represents a physical vapor deposition process using a heated crucible or an electron beam evaporator as the vapor source<sup>[62]</sup>. Sputter deposition (S) is performed by extracting ions from a plasma at keV energies that strike a target consisting of the material to be deposited<sup>[63]</sup>. Molecular beam epitaxy (MBE) uses continuous molecular beams generated by Knudsen sources<sup>[64, 65]</sup>. The deposition flux in chemical vapor deposition (CVD) is derived from the reaction of two or more gaseous chemicals on or above a heated substrate<sup>[66]</sup>. Heaters above the substrate provide the energy necessary to sustain the reaction. Metal organic chemical vapor deposition (MOCVD) is similar to CVD, except that the reacting gases are metal-organic compounds that widen the range of materials that can be deposited by normal CVD.

*Table 3.1: Most known deposition processes.*

Technique	Acronym	Experimental purpose	Reference
Thermal evaporation	TE	optics, protective coatings, electronic materials	[67]
Sputtering (RF, magnetron, ion beam)	S	electronic materials, optics, protective coatings	[68, 69, 70]
Molecular beam epitaxy	MBE	electronic materials	[71, 72, 73, 74, 75]
Chemical vapor deposition	CVD	protective coatings, structural and electronic materials	[76]
Metal-organic chemical vapor deposition	MOCVD	electronic materials	[77, 78, 79, 80, 81, 82, 83, 84]
Pulsed Laser Deposition	PLD	electronic materials	[85, 86, 87]

Physical vapor deposition techniques such as plasma and ion beam sputter deposition and pulsed laser ablated deposition are extensively used for synthesizing single and multicomponent and multilayered thin films<sup>[88]</sup>. The development of PLD has moved rapidly since the discovery of high-temperature superconductor oxides in 1986<sup>[89]</sup>. These oxides have a perovskite-based crystal structure similar to many ferroelectric materials and have been deposited as epitaxial films by, e.g., PLD<sup>[90]</sup>. This deposition technique offers a number of advantages over the other techniques used for the preparation of thin films of ferroelectrics; in particular, epitaxial films can be deposited at rather low substrate temperatures and high deposition rates, over a large range of target phases and compositions, and with few experimental parameters to optimize. An automated PLD technique involves ablation of elemental targets (metals or their oxides) sequentially exposed to an excimer laser beam using a computer-controlled system.

The physical phenomena involved in the interaction of high-power nanosecond excimer-laser pulses with bulk targets resulting in evaporation, plasma formation, and subsequent deposition of thin films were studied by Singh and Narayan<sup>[91, 92]</sup>. They developed a theoretical model for simulating the laser-plasma-solid interaction. Based on the nature of interaction of the laser beam with the target and the evaporated material, the pulsed laser evaporation process has been divided into three separate regimes: (i) interaction of the laser beam with the bulk target, (ii) plasma formation, heating, and initial three-dimensional isothermal expansion, and (iii) adiabatic expansion of the plasma and deposition of thin films (Fig. 3.1). The first two processes occur during the time interval of the laser pulse, while the last process begins after the laser pulse has terminated.

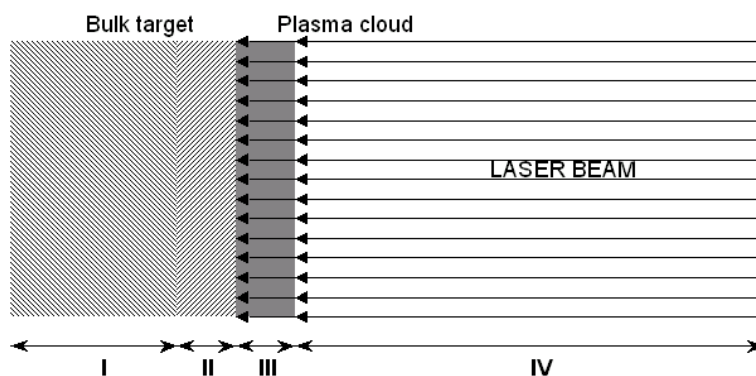


**Fig. 3.1:** Schematic diagram of the laser interaction with the plasma target showing different phases<sup>[91]</sup>: (I) unaffected bulk target, (II) evaporated target surface, (III) dense plasma absorption of the laser radiation, and (IV) expanding plasma.

Thus the impact of the laser beam on the target surface results in a complex process including ablation, melting, and evaporation of material, and producing a plasma due to excitation and ionization of the species ejected from the target by the laser photons. All these processes are triggered by the transformation of electromagnetic energy into electronic excitation, followed by a transformation into thermal, chemical, and mechanical energy. The materials ejected from the target are finally deposited onto a substrate.

Device structures which have been fabricated using PLD-grown ferroelectric thin films include non-volatile random access memory (NVRAM) test structures with oxide electrodes<sup>[93]</sup>, surface acoustic wave (SAW) devices<sup>[94]</sup>, tunable radio frequency (RF) phase shifters<sup>[95]</sup>, acoustic wave

transducers<sup>[96]</sup>, electro-optic switches<sup>[97]</sup>, and pyroelectric sensors<sup>[98]</sup>. A recently renewed interest in ferroelectric thin films can be observed due to their potential with respect to smart materials and active sensors in smart devices<sup>[99]</sup>. In fact, new applications for ferroelectrics will likely be conceived as the ability to prepare high quality films with specific properties is realized<sup>[100]</sup>. PLD is already making impact in this developing field by combining several materials in view of discovering new materials with improved properties. The versatility of the PLD technique is demonstrated by the fact that close to 128 different materials have been deposited as thin films<sup>[101]</sup>. For example, PLD can be used advantageously to synthesize high-quality multicomponent oxide thin films including ferroelectrics, high-temperature superconductors, electro-optic and optical materials<sup>[102, 93]</sup>. A balanced description of advantages and disadvantages of the PLD technique to synthesize high temperature superconductors and ferroelectric films has been presented in several reviews<sup>[103, 104, 105, 87]</sup>. Key advantageous features of the PLD technique include: (1) the possibility of a straightforward transfer, under certain conditions, of a target stoichiometry to the film; (2) the ability to deposit in high background pressures, which in this case minimizes vaporization of volatile species from the film; (3) the ease of deposition at elevated substrate temperature which enables epitaxial film growth and can minimize the thermal budget during processing, and (4) the demonstrated high deposition rate (about 10 Å/s).

Preparation of (Ba,Sr)TiO<sub>3</sub> thin films has been carried out by reactive evaporation<sup>[106]</sup>, rf-sputtering<sup>[107]</sup>, metal organic chemical vapor deposition<sup>[8]</sup>, sol-gel<sup>[3]</sup>, and laser ablation methods<sup>[4]</sup>. The main problem of MOCVD for BaO, SrO, or rare earth-based oxides is the poor volatility and thermal stability of the precursors. Different approaches, mainly using a liquid source, have been proposed to solve this problem. Pulsed liquid-injection MOCVD deposition permits the generation of a stable gas phase from unstable precursors. By adjusting the injection parameters and the molar concentration of the solutions, a “layer-by-layer” growth mode can be approached. This technique is based on the computer-controlled injection of micro-droplets of precursor solution into the evaporator system. In recent years, PLD was developed as a significant method to study the growth processes of oxide thin films.

### 3.1.2 PLD system

The PLD system used in the present study is schematically shown in Fig. 3.2. This PLD system consists of a KrF excimer laser ( $\lambda = 248$  nm,  $\lambda$  - wavelength of the emitted radiation) (Fig. 3.3) and a UHV system in turn consisting of a load lock and a deposition chamber.

The laser beam is directed onto the target by an optical system of lenses. The lens and window materials are chosen to minimize any absorption of laser light and thus to ensure a maximum attainable laser energy on the target. The laser beam is focused at an angle of 45° onto one out of four pressed ceramic powder targets (e.g., BaTiO<sub>3</sub> or SrTiO<sub>3</sub> targets) located in the vacuum chamber (Fig. 3.4).

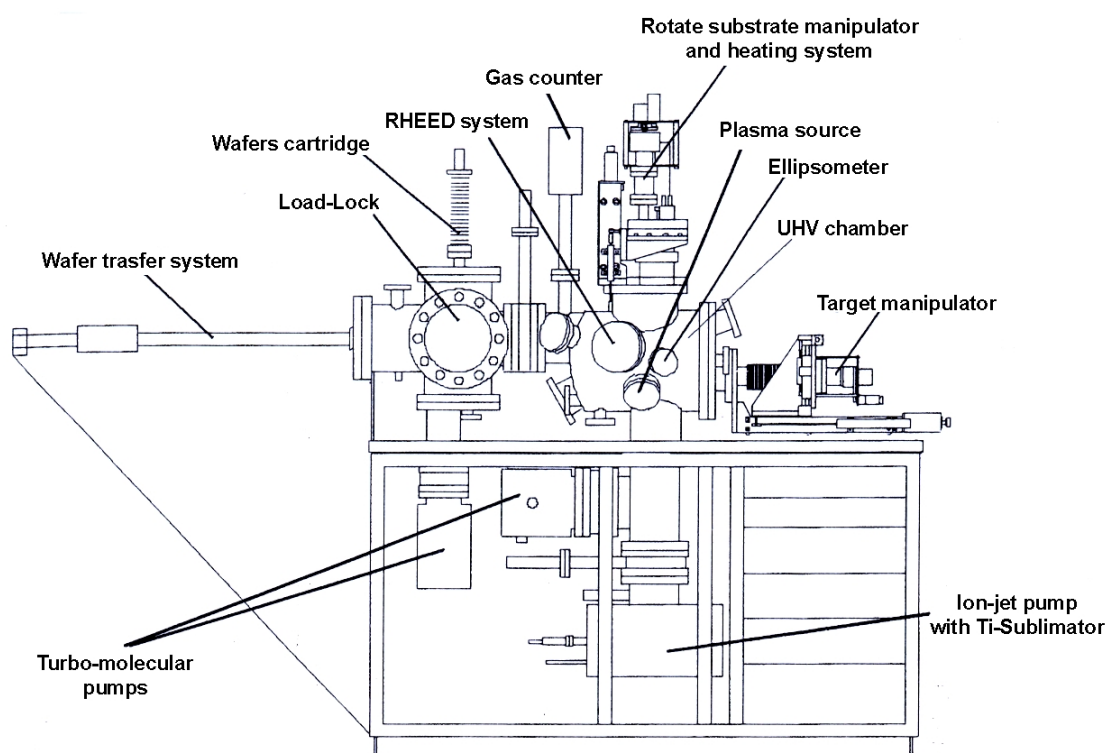


**Fig. 3.2:** Scheme of the pulsed laser deposition system used in the present study (according to Fa. Surface-Hückelhoven, UHV-Laserablationsanlage LDS 3/12, Systembeschreibung). The entrance of the laser beam is on the rear side (not visible here).

The  $\text{SrTiO}_3$  substrates ( $10 \times 10 \times 1 \text{ mm}^3$ ) are glued on a Si (3") carrier wafer using silver paste allowing a good thermal contact between the  $\text{SrTiO}_3$  substrate and the Si wafer. Then the carrier wafer with the substrate is mounted on a stainless steel substrate holder which is finally introduced into the deposition chamber using a load-lock system controlled by computer. The distance between the sample holder and the target carousel holder, the selection of the target to be ablated (out of several targets), as well as the entire deposition process are controlled by two computers. Selection of the target, laser energy, and laser repetition rate can be chosen in the desired order. The temperature is measured inside the heater block with a K-type thermocouple and the maximum temperature achieved is about  $850 \text{ }^\circ\text{C}$ .

### 3.1.3 PLD Parameters

#### General considerations

When the laser radiation is absorbed by the solid surface of the target, electromagnetic energy is converted first into electronic excitation and then into thermal, chemical, and even mechanical energy to cause evaporation, ablation, excitation, plasma formation and exfoliation. The evaporated material forms a plume which consists of a mixture of energetic species including atoms, molecules, electrons, ions, clusters, and droplets. The collisional mean free path inside the dense plume is very short. As

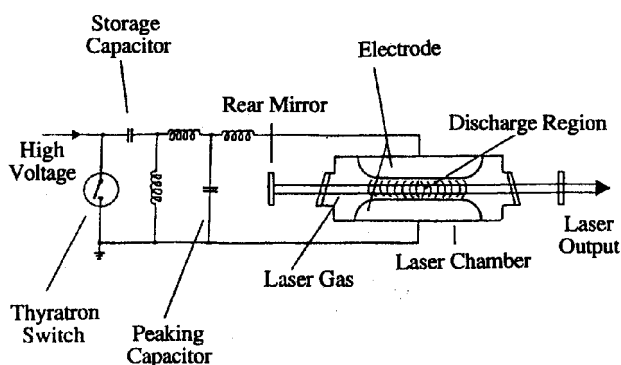


*Fig. 3.3: Scheme of the design of the excimer laser discharge circuit used in the present study.*

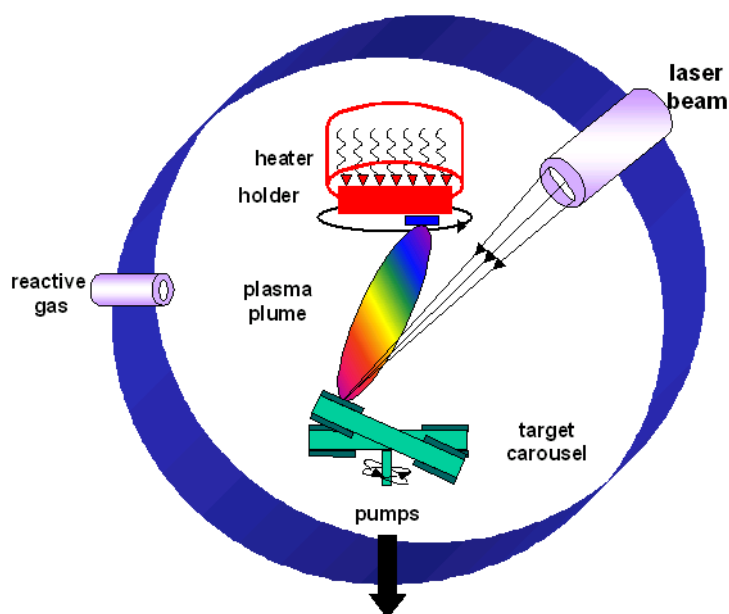


*Fig. 3.4: Schematic diagram of the vacuum chamber used in the present study.*

as a result, immediately after the laser irradiation, the plume rapidly expands from the target into the vacuum or background gas forming a jet with hydrodynamic flow characteristics. This way, the deposition process by PLD consists of three stages:

1. The laser beam strikes the target producing a highly forward-directed plume of partially ionized gas.
2. This plume interacts chemically and physically with the laser beam and the background ambient.
3. The ablated material condenses onto a usually heated substrate where a thin film grows.

Each of these processes plays an important role in the deposition of high quality films. The adjustable experimental parameters are the laser fluency and (to some extent) the wavelength, the composition, structure (i.e. phase) and density of the target, the reactive background gas and its pressure, and the substrate temperature. Understanding how the experimental conditions affect the nucleation and growth of laser-deposited films is an area of research activity in its own right. It is very important to understand the parameters which influence the growth in order to control them and to determine the

film properties, such as orientation, microstructure, and dielectric properties. A discussion of these parameters is the subject of this section.

#### *Target material*

Ideally, when ablating the target, the laser should cause a stoichiometric transfer of the composition of the target to the growing film. Complex-oxide targets are usually obtained from sintering mixtures of the component metal oxides or from calcination of oxide powders. “Fully reacted” targets result from a complete solid-state reaction during the sintering process, whereas “pressed-oxide” targets result only from a mechanical process. Since sintering takes place at high temperatures, it is possible that volatile components of the target may be lost during this process, especially at the surface. Usually the pressed-oxide targets are processed at much lower temperatures (below 600 °C) than the fully reacted targets, and therefore are less affected by losses of volatile components<sup>[108]</sup>.

In order to stabilize the target, the deposition process is typically preceded by a target “burn-in”, during which the target is irradiated by several laser shots prior to using it for the film growth. The purpose of this process is to expose fresh material, and maintain a steady-state composition at the target surface. The surface composition may differ from that in the interior of the target due to segregation phenomena that may occur during target ablation. This burn-in process should be repeated whenever the ambient gas conditions are changed because the segregation process is sensitive to the ambient.

A disadvantage of PLD, in general, is the presence of droplets on the substrate surface. The droplets generated by laser ablation can be due to: (i) protrusions, pits, craters or microcracks that exist in a fresh target or are progressively formed after substantial laser irradiation, being removed from the target due to the thermal and mechanical shock induced by the laser; (ii) rapid expansion of trapped vapor bubbles beneath the surface during laser irradiation, causing forced ejection of surface material; (iii) splashing of the molten layer near the upper surface of the target due to rapid surface evaporation (most commonly observed in case of use of high-power lasers); (iv) condensation of vapor material due to supersaturation (most likely observed in case of use of high gas pressure). Many attempts have been made to avoid the presence of droplets. In case of metals two kinds of droplets (depending on the expelling place, that is from the cones growing out of the target or from the molten surface) have been observed, which have different sizes, angular distributions, velocities, and dependencies on the number of pulses, the roughness of the target and the density of the laser energy<sup>[109]</sup>. The stoichiometry of the oxide targets plays an important role in the density of droplets<sup>[110]</sup>.

#### *Substrate temperature*

The role of the substrate temperature in controlling structure and composition of the film is a primary one. Effects of the substrate temperature appear to be most important in obtaining a particular crystal structure and orientation. E.g., a minimum temperature is usually required to grow crystalline



films rather than amorphous, or epitaxial films rather than polycrystalline. This temperature should be below the temperature at which extensive vaporization of volatile film components occurs. The thermal energy that the condensing species attain on the substrate surface allows to increase the surface mobility and the energy for nucleation and growth of the film. At a particular temperature necessary for these processes to successfully occur, however, some volatile components may not stick to the substrate and/or some may evaporate after incorporation into the film.

Several research groups prepared thin films at near room temperature (conditions typically required for stoichiometric, but amorphous materials) followed by post-deposition annealing at high temperature to recrystallize the material and to induce ferroelectricity. The polycrystalline films that result from post-deposition treatments may not be fully crystallized and are typically neither oriented nor dense. *In-situ* deposition, positioning the substrate onto a heated stage, is the preferable approach to achieve high quality film growth and can yield dense and epitaxial films.

However, measurement of the true substrate temperature is difficult. Therefore, a temperature window for optimum film growth is frequently given in terms of the temperature of the heater.

Each ferroelectric material appears to have a distinct substrate temperature range that is optimum for epitaxial film growth, falling roughly within a 550 °C to 800 °C window or even higher. BaTiO<sub>3</sub> was reported to grow epitaxially at temperatures ranging from 670 °C to 750 °C on MgO by Norton et al.<sup>[111]</sup>. Davis and Gower<sup>[112]</sup> found that BaTiO<sub>3</sub> will not grow epitaxially at temperatures below 600 °C. *c*-axis textured BaTiO<sub>3</sub> films were deposited at a substrate temperature as low as 600 °C by Lin et al.<sup>[113]</sup>. Although depositions performed at 750 °C on MgO and SrTiO<sub>3</sub> substrates yielded the (001) orientation of the BaTiO<sub>3</sub> films, detailed analysis revealed that the crystallinity of films deposited on SrTiO<sub>3</sub> substrates is clearly superior to that of films deposited on MgO substrates. Low substrate temperatures (550 ÷ 650 °C) tend to induce the growth of (110) grains. Non-(001) orientations appear when the oxygen pressure is either too low or too high.

#### *Oxygen partial pressure*

At a given substrate temperature, the incorporation of a volatile atom into the film is greatly dependent upon the pressure of the oxidizing atmosphere. This can be understood from the decrease in vapor pressure observed for metals when they become oxidized. The ambient gas, however, must not only help to keep the atoms on the surface once they arrive, but must also contribute to avoid oxygen losses. *In-situ* fabrication of oxide thin films is generally carried out in an oxygen ambient. Oxygen atoms, ions or molecules in the deposition chamber react with the plume and thus contribute to an optimal oxygen content in the thin film during growth.

At low gas pressure, the scattering of the ejected species by the gas atoms or molecules is the dominant process that determines the relative Ba/Ti content of the deposited films, while at high oxygen pressure, the combination of the initial scattering and the further diffusion that takes place once the injected species have been thermalized is the process that determines the film composition<sup>[114]</sup>.

Norton and Carter deposited BaTiO<sub>3</sub> films on (100) MgO substrates using different oxygen partial pressure and they studied the nucleation and growth of BaTiO<sub>3</sub> by transmission electron microscopy observing two different microstructures as a function of pressure<sup>[111]</sup>: Higher oxygen pressure ( $\geq 0.40$  torr) yielded epitaxial film growth, while lower pressures gave rise to polycrystalline films.

The preferred orientation of thick BaTiO<sub>3</sub> films was found to depend on the deposition pressure<sup>[115]</sup>. A (100)-orientation was developed below 1 mTorr deposition pressure, while the (110)-orientation was found above 200 mTorr deposition pressure. During the deposition between 50 and 100 mTorr, the preferred orientation varied between (111), (110), and (100). It has been observed that the growth of a *c*-axis-oriented BaTiO<sub>3</sub> film is favoured by a lower oxygen pressure, while the growth of an *a*-axis-oriented BaTiO<sub>3</sub> film is favoured by a higher oxygen pressure<sup>[116]</sup>. The lattice constant normal to the substrate decreases with increasing oxygen pressure, probably due to a particle bombardment mechanism and/or thermal vibrations. Moreover, a higher deposition temperature results in an increased mobility of the adsorbed BaTiO<sub>3</sub> clusters and in a better film recrystallization.

Different temperature and oxygen pressure conditions which have been used by different groups are summarized in Table 3.2.

**Table 3.2:** Different deposition conditions for BaTiO<sub>3</sub> films used in PLD.

author[reference]	substrate	temperature (°C)	oxygen pressure (mbar)
Davis <sup>[112]</sup>	MgO (100)	575	-
	SrTiO <sub>3</sub> (110)	850	-
	LiF (100)	600	-
Ito <sup>[117]</sup>	MgO (100)	650 ÷ 700	0.05
Kim <sup>[115]</sup>	Pt/SiO <sub>2</sub> /Si	700	0.0013 ÷ 0.26
Gonzalo <sup>[114]</sup>	MgO (100)	700	1
	Si (100)	RT	10 <sup>-7</sup>
Hwang <sup>[118]</sup>	Pt/Ti/SiO <sub>2</sub> /Si (100)	750	0.13
Srikant <sup>[119]</sup>	MgO (001)	700 ÷ 750	0.13 ÷ 0.26
Kim <sup>[120]</sup>	MgO, LaAlO <sub>3</sub> , Pt/Ti/SiO <sub>2</sub> /Si	500 ÷ 800	0.4
Khan <sup>[121]</sup>	SrTiO <sub>3</sub> (100)	650	0.26
	sapphire (0001)	700	0.26
Suzuki <sup>[122]</sup>	SrTiO <sub>3</sub>	700	0.01
Beckers <sup>[123]</sup>	MgO (001)	1000	0.004
Lin <sup>[113]</sup>	MgO (001)	750	0.1
	SrTiO <sub>3</sub> (001)	750	0.1
	YBCO/CeO <sub>2</sub> /SrTiO <sub>3</sub> (001)	730	0.1
Liu <sup>[124]</sup>	MgO (100)	750	0.1
	YBCO/SrTiO <sub>3</sub> (001)	750	0.15
Boikov <sup>[125]</sup>	MgO, LaAlO <sub>3</sub> , SrRuO <sub>3</sub> (100)	740 ÷ 785	0.4

*Film-substrate lattice mismatch*

While the substrate temperature is an important parameter for deposition to obtain epitaxial films, the mismatch between the lattice constants of film and substrate is equally critical. The lattice mismatch is defined as shown in eq. 2.6. Epitaxial film growth occurs most readily when the lattice spacing and symmetry of the substrate closely match those of the desired film.

In fact, the requirements to the substrate are even more complicated. Thus, substrates should have thermal expansion coefficients close to that of the oxide film material, otherwise due to shock during thermal cycling, the grown films are known to develop microcracks leading to discontinuities in the films. Another requirement for the substrate material is to be chemically compatible in terms of the nature of the chemical bonds.

Several usual substrates and their mismatch with respect to the BaTiO<sub>3</sub> lattice constants have been summarized in Table 3.3.

**Table 3.3:** Lattice mismatch between BaTiO<sub>3</sub> film and several substrates.

Substrate	Structure	Lattice constant	Mismatch with BaTiO <sub>3</sub>
BaTiO <sub>3</sub>	tetragonal (perovskite structure)	$a = b = 3.994 \text{ \AA}$ $c = 4.038 \text{ \AA}$	
SrTiO <sub>3</sub>	cubic (perovskite structure)	$a_c = 3.905 \text{ \AA}$	2.28 % along $a$ -direction 3.4 % along $c$ -direction
MgO	cubic (NaCl structure)	$a_c = 4.212 \text{ \AA}$	-5.17 % along $a$ -direction -4.13 % along $c$ -direction
Al <sub>2</sub> O <sub>3</sub>	trigonal (sapphire structure)	$a = 5.14 \text{ \AA}$	-22.29 % along $a$ -direction -21.44 % along $c$ -direction
YSZ	cubic (fluorite structure)	$a_c = 5.16 \text{ \AA}$	-22.59 % along $a$ -direction -21.74 % along $c$ -direction
Si	cubic (diamond structure)	$a_c = 5.43 \text{ \AA}$	-26.44 % along $a$ -direction -25.63 % along $c$ -direction
YBa <sub>2</sub> Cu <sub>3</sub> O <sub>7</sub>	perovskite- -derived structure	$a = 3.83 \text{ \AA}$ $b = 3.89 \text{ \AA}$ $c = 11.68 \text{ \AA}$	4.28 % along $a$ -direction 2.67 % along $b$ -direction -65.42 % along $c$ -direction
LaAlO <sub>3</sub>	rhombohedral (perovskite structure)	$a = 5.364 \text{ \AA}$ $c = 13.11 \text{ \AA}$	-25.54 % along $a$ -direction -69.19 % along $c$ -direction

It was observed that epitaxial BaTiO<sub>3</sub> deposited by PLD shows different growth mechanisms on different substrates because of different lattice mismatch. For example, BaTiO<sub>3</sub> was reported to grow on MgO (cubic,  $a_c = 0.4231 \text{ nm}$ ) following an island growth mode<sup>[111]</sup>, whereas BaTiO<sub>3</sub> thin films grown on SrTiO<sub>3</sub> substrates seems to follow the layer-by-layer mode<sup>[6]</sup>.

A dependence of the lattice parameter on film thickness was reported for an epitaxial system with a small lattice mismatch such as BaTiO<sub>3</sub> on SrTiO<sub>3</sub><sup>[107, 126, 127, 73, 74]</sup>. In this case, if the thickness

of the BaTiO<sub>3</sub> film is under a certain critical value, the epitaxial film can grow two-dimensionally, whereas when the thickness exceeds a critical value misfit dislocations are introduced, lattice relaxation occurs, and the lattice parameter of the film becomes (almost) equal to that of the bulk.

#### *Target-substrate distance*

Thickness and composition of the thin films grown by PLD are functions of the distance between the target and the substrate. The laser-evaporated neutral and ionized particles travel at a speed of about 10<sup>6</sup> cm/s in vacuum<sup>[128]</sup>. As the oxygen partial pressure increases, the velocity of these particles decreases due to collisions. If the substrate-to-target distance is small, the grown films are known to contain large number of particulates (droplets).

An optimal distance of 4 - 7 cm was used by various groups.

#### *Laser energy and repetition rate*

When a target is bombarded with ions, electrons, single photons, or pulsed photons (called *laser pulses*), a mechanism of particle emission is generated. This mechanism is called *ablation* or *desorption*. Bombardments with pulses of particles (called *secondary* mechanism) differ fundamentally from bombardments with single particles (called *primary* mechanism) in which emitted particles often have a sufficiently high density to interact<sup>[129]</sup>. The secondary mechanism includes collisions, thermal and electronic processes, exfoliation, hydrodynamic processes, and condensation. All the above mentioned processes depend on whether the release is from a solid surface or from a loose powder reservoir, and they also depend on whether particles that are backscattered toward the surface are reflected or absorbed (i.e., recondensed).

At low laser energy densities, small quantities of emitted neutral and ionized material become detectable. For many materials, significant removal rates begin at high temperatures, which, in turn, necessitate high laser energy densities, called *threshold*<sup>1</sup> for laser ablation<sup>[130]</sup>. Increasing the laser energy usually results in two threshold effects: significant material removed and the appearance of the luminous plasma plume. These threshold effects are most often described by an evaporation and a subsequent absorption of a part of the laser pulse by the vapor phase.

The laser fluence can affect the chemical composition of the plume. However, the extent to which the laser will affect the incorporation of volatile constituents into the growing film is minor. An important criterion for the laser-assisted approach to be successful is to adjust the time delay between the two laser pulses, such that the firing of the second laser coincides with the arrival of the laser-ablated species at the substrate surface. The photons apparently stimulate the motion of atoms and small molecules on the film surface by increasing the local surface temperature. The advantage of PLD is that much lower average processing temperatures are required. The second laser pulse may

---

<sup>1</sup>The *ablation threshold* is defined as the energy density, in J/cm<sup>2</sup>, at which measurable material-removal begins.

even enhance the nucleation rate of the ferroelectric phase. Sometimes nucleation effects dominate the formation of a particular phase. Overcoming the activation energy for nucleation is usually accomplished through increased substrate temperatures. A competition between the formation of the various crystalline phases can exist.

Blank *et al.*[131, 132, 133] succeeded to enhance the layer-by-layer growth mechanism by increasing the time interval between the laser pulses in the so-called *pulsed laser interval deposition*, so that the film structure can reorganize or relax during the interval between two pulses.

A great amount of control of the film structure and orientation involves the optimization of all deposition parameters. It should be noted that the PLD parameters discussed above are not all independent. A change in a parameter may bring about a change in the others, and a reasonable variation even in one parameter calls for the optimization of the other parameters as well. In the present study, PLD parameters were optimized for each material under investigation.

### Experimental conditions used in the present study

The deposition conditions used in the present study for epitaxial BaTiO<sub>3</sub> and SrTiO<sub>3</sub> films grown on (001)-oriented Nb-doped SrTiO<sub>3</sub> (SrTiO<sub>3</sub>:Nb) substrates by PLD are summarized in table 3.4.

*Table 3.4: Deposition conditions used in the present study.*

Substrate material	Target material	Target-substrate distance	Deposition temperature	Oxygen pressure	Laser energy	Laser repetition rate
SrTiO <sub>3</sub> :Nb	BaTiO <sub>3</sub>	6 cm	700 °C	0.2 mbar	600 mJ	1 Hz
	SrTiO <sub>3</sub>	6 cm	700 °C	0.2 mbar	600 mJ	1 Hz

Commercial BaTiO<sub>3</sub> and SrTiO<sub>3</sub> targets were used in the present study (The BaTiO<sub>3</sub> target was supplied by Praxair Speciality Ceramics, and the SrTiO<sub>3</sub> target was made by Superconductive Components). Both BaTiO<sub>3</sub> and SrTiO<sub>3</sub> targets were prepared by a ceramic method. The BaTiO<sub>3</sub> target was prepared from powder, by cold-isostatically pressing and then sintering at a temperature of 1325 °C. A high-density BaTiO<sub>3</sub> target (purity of 99.9%) was encapsulated into a Cu cup using an alloy of In and Sn (90wt% In and 10wt% Sn) to prevent possible cracks. After sintering, the diameter and the surface of the BaTiO<sub>3</sub> target were machined to the final target thickness and dimension, in this way also removing any surface contamination that may have resulted from the previous handling steps. The SrTiO<sub>3</sub> target was prepared in the same way, from phase pure powder, and it was sintered for 4 - 8 hours at 1250-1350 °C in air. The target size is about 50 mm in diameter and 6 mm in height. Phase purity and the structure were confirmed by x-ray diffraction (Fig. 3.5).

In the present study, targets are kept in vacuum and they are polished regularly and then burned before each deposition to reduce the density of droplets.

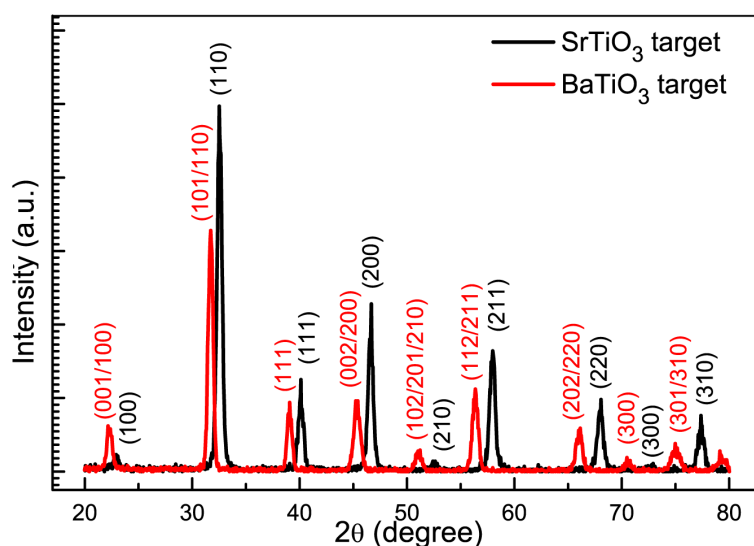


**Fig. 3.5:** X-ray diffraction patterns of polycrystalline  $\text{BaTiO}_3$  and  $\text{SrTiO}_3$  targets

The optimum temperature for the epitaxial  $\text{BaTiO}_3/\text{SrTiO}_3$  deposition was found from a temperature variation between  $550^\circ\text{C}$  and  $750^\circ\text{C}$ .  $\text{BaTiO}_3$  films with a poor epitaxial crystalline structure are growing at a deposition temperature of  $550^\circ\text{C}$  or  $600^\circ\text{C}$  (Fig. 3.6).

The deposition temperature was optimized at an oxygen pressure of 0.2 mbar, which had been determined to be the optimum oxygen pressure (Fig. 3.7). These films were cooled down after deposition in vacuum at a pressure of  $10^{-6}$  mbar.

The influence of different laser energies on the film orientation is presented in Fig. 3.8, where 400, 600, and 800 mJ of laser energy were used to deposit epitaxial  $\text{BaTiO}_3$  films. Different energies result in different thicknesses of the epitaxial  $\text{BaTiO}_3$  films, not in different qualities of these films. In the present study, an optimum energy of 600 mJ was used.

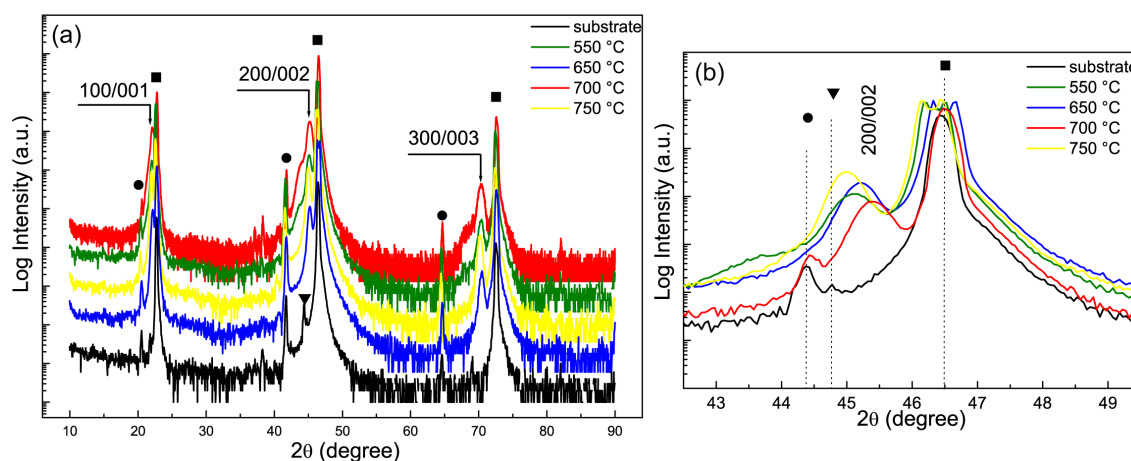


**Fig. 3.6:** (a) X-ray diffraction patterns of epitaxial  $\text{BaTiO}_3$  films deposited at  $550^\circ\text{C}$ ,  $650^\circ\text{C}$ ,  $700^\circ\text{C}$ , and  $750^\circ\text{C}$ . (b) Zoom-in area of the 002 peak of  $\text{SrTiO}_3$ . The peaks labelled as  $m00/00m$  are the  $\text{BaTiO}_3$  film peaks. Those labelled with squares are the  $\text{SrTiO}_3$  substrate peaks, while those labelled with circles and triangle are the substrate peaks originating from the remaining  $\text{Cu-K}_\beta$  radiation and from the  $\text{W-L}_\alpha$  radiation, respectively. The latter comes from the tungsten contamination of the x-ray target. All curves are displaced vertically by the same amount.

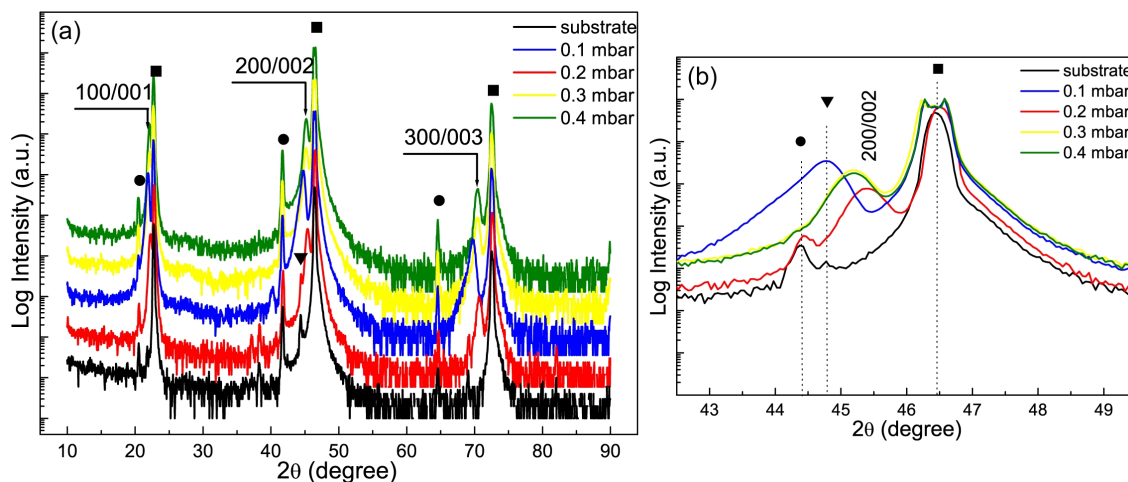


**Fig. 3.7:** (a) X-ray diffraction patterns of epitaxial  $\text{BaTiO}_3$  films deposited at 0.1, 0.2, 0.3, and 0.4 mbar oxygen partial pressures. (b) Zoom-in area of the 002 peak of  $\text{SrTiO}_3$ . The peaks labelled as  $m00/00m$  are the  $\text{BaTiO}_3$  film peaks. Those labelled with squares are the  $\text{SrTiO}_3$  substrate peaks, while those labelled with circles and triangle are the substrate peaks originating from the remaining  $\text{Cu-K}_\beta$  radiation and from the  $\text{W-L}_\alpha$  radiation, respectively.

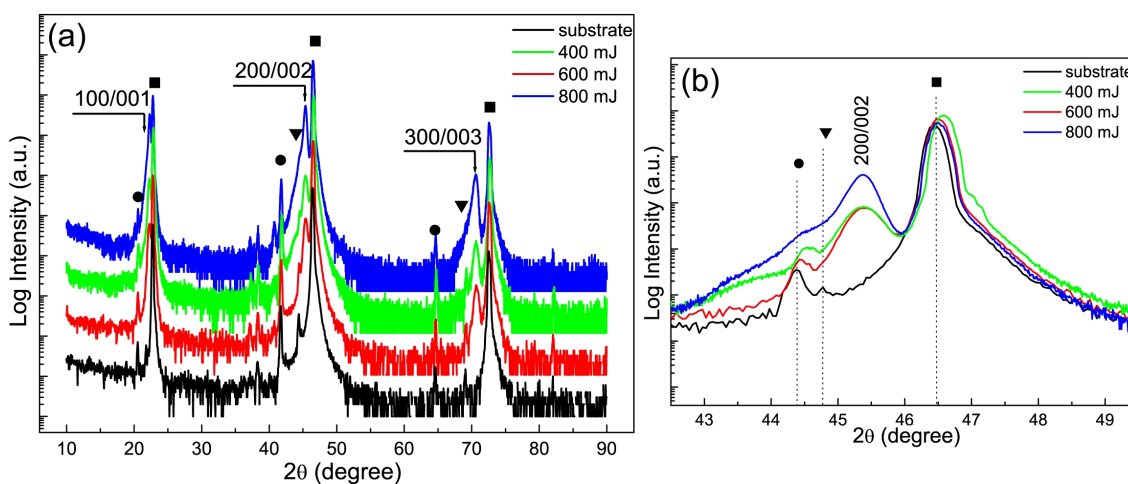


**Fig. 3.8:** (a) X-ray diffraction patterns of epitaxial  $\text{BaTiO}_3$  films deposited at 400, 600, and 800 mJ laser energies. (b) Zoom-in area of the 002 peak of  $\text{SrTiO}_3$ . The peaks labelled as  $m00/00m$  are the  $\text{BaTiO}_3$  film peaks (Fig. 3.8). Those labelled with squares are the  $\text{SrTiO}_3$  substrate peaks, while those labelled with circles and triangle are the substrate peaks originating from the remaining  $\text{Cu-K}_\beta$  radiation and from the  $\text{W-L}_\alpha$  radiation, respectively.

Despite the fact that the deposition conditions are the same for both materials, the deposition rate of SrTiO<sub>3</sub> (0.0797 nm/s) is lower than the deposition rate of BaTiO<sub>3</sub> (0.0987 nm/s). The thickness of the BaTiO<sub>3</sub> film and the SrTiO<sub>3</sub> film was measured by profilometer. The deposition rates of the BaTiO<sub>3</sub> material and the SrTiO<sub>3</sub> material were calculated from the slopes of two graphs (for each material in discussion) representing the thickness vs. time (or number of laser shots).

## 3.2 X-ray diffraction

### 3.2.1 Basic principle

A monochromatic x-ray beam is generated by the characteristic K<sub>α</sub> emission of a target element, possibly filtered by means of a certain absorption edge and possibly additionally sharpened in wavelength by the help of a crystal monochromator. In order to record a reflection of order  $n$  from a set of lattice planes ( $hkl$ ), the incidence angle  $\theta$  must meet Bragg's condition:

$$\sin\theta = n\lambda / 2d(hkl) \quad (3.1)$$

Setting the crystal to successive Bragg incidence angles is achieved by rotating it about an axis.

Since the penetration of x-rays into solids is limited to less than 0.1 mm in most solids, the x-ray diffraction spectra obtained from solids stem from a relatively thin layer close to the surface. In contrast to bulk samples, in thin films some properties must be taken explicitly into account such as thickness, density, and mass absorption<sup>[134]</sup>. Nevertheless, in practice there are many obstacles. The main problem is that of the texture. Whereas in bulk samples texture is largely a function of crystalline orientation and shape, in thin films that have a grain size of the same order of magnitude as the film thickness, preferred orientation is also a function of crystallite size due to an anisotropic growth rate<sup>[135]</sup>.

The film orientation or texture can be determined by several diffraction methods (e.g., a single crystal diffraction, a rotation method or a powder method). Data are then fed into the associated computer which sets the goniometer automatically for measuring the  $hkl$  reflection intensities and subtracting the background intensities. The various intensity corrections (polarising, Debye-Waller and geometric corrections) are integrated in the programs. Measurement of the  $hkl$  reflection angles leads to the determination of the lattice parameters. Indexing the  $hkl$  reflection and assessing the systematic film peak presence leads to the determination of the space group. Measuring the reflection intensities gives the position of the atoms in the crystal, i.e. finally the crystal structure.



### 3.2.2 Crystalline orientation analysis

#### General considerations

Each grain in a polycrystalline film normally has a crystalline orientation different from that of its neighbours. Considered as a whole, the orientations of all grains may be randomly distributed or they may tend to align into some particular orientation or orientations. That is called preferred orientation, or texture, which can be defined simply as a condition in which the distribution of crystal orientations is not random.

When most of the film grains are oriented with a certain crystallographic plane  $(hkl)_f$  exactly or roughly parallel to the substrate surface, and a certain direction  $[uvw]_f$  in that plane is exactly or roughly parallel to a certain direction  $[uvw]_s$  in the substrate surface  $(hkl)_s$ , the film orientation is described by the notation:

$$(hkl)_f [uvw]_f \parallel (hkl)_s [uvw]_s \quad (3.2)$$

The film orientation or texture can be determined by several diffraction methods which can be divided into two groups: transmission and reflection, both being necessary for a complete characterization. A full description of the texture requires the specification of three angles named  $\theta$ ,  $\phi$ , and  $\psi$ . Therefore,  $\theta$ - $2\theta$  scan, pole figure and  $\phi$  scan should be measured (see Fig. 3.9 later).

The film orientation or texture can be determined by measuring a pole figure, which is most similar to a stereographic projection, and by comparing it with a pole figure of the substrate. Pole figures show the variation of the diffraction intensity (“pole density”) with pole orientation for a selected set of crystal planes. If the film grains have a completely random orientation, these poles will be distributed uniformly over the projection. If a preferred orientation is present, the poles will tend to cluster in certain areas of the projection, leaving other areas virtually unoccupied. Although only a pole figure can provide a complete description of the preferred orientation, some information can be obtained fairly quickly by a comparison of calculated diffraction line intensities with those observed on an ordinary diffractometer scan. If a sample is examined in the diffractometer by the usual  $\theta$ - $2\theta$ -scan, then the only grains which can contribute to the  $hkl$  reflection are those whose  $(hkl)$  planes are parallel to the substrate surface. If the film texture is such that there are very few such grains, the intensity of the  $hkl$  reflection will be automatically low.

A pole figure analysis involves two rotations about  $\phi$  and  $\psi$  axes. Valuable information with respect to the crystallographic orientation of a film on a substrate can be obtained by a  $\phi$  scan taken at definite  $\theta$  and  $\psi$  values.

The crystallite size can also be measured by diffraction. When the size of the individual crystallites is less than 100 nm, the term *particle size* is usually used, but the term *crystallite size* is more precise. This size is given by measuring the Full Width at Half Maximum (FWHM) as follows:

$$FWHM = \frac{0.9\lambda}{t \cos\theta} \quad (3.3)$$

where  $\lambda$  is the wavelength,  $t$  is the diameter of the crystallites and  $\theta$  is the diffraction angle. An efficient method for measuring the size of small crystallites is the so-called “small-angle scattering” which uses a scattering angle close to  $0^\circ$  to observe the size of the film crystallites. The FWHM values are calculated from the width of a specific peak in the scattered intensity vs.  $2\theta$  graph.

The shape of the diffraction peak, i.e., the intensity as a function of the rotation of the sample, is termed *rocking curve*. A complete value of FWHM should be calculated from the rocking curve and compared with the one of the intensity vs.  $2\theta$  curve. The presence of linear or planar defects in the crystalline structure of the sample increases the width of the rocking curve. Measurement of rocking curves is, therefore, important for assessing the perfection of the structure of epitaxial films.

### XRD analysis performed in this study

In this study, crystallographic analyses of BaTiO<sub>3</sub> films and BaTiO<sub>3</sub>/SrTiO<sub>3</sub> multilayers deposited on SrTiO<sub>3</sub> substrates by PLD were performed by XRD  $\theta$ - $2\theta$  and  $\phi$  scans, and by recording pole figures using a Philips X’Pert MRD four-circle diffractometer with Cu K $\alpha$  radiation and a parallel plate collimator in front of the detector achieving a  $2\theta$  resolution of  $0.1^\circ$ . Pole figures were measured using an open Eulerian cradle.

The surface normal of the sample can be positioned to coincide with the diffractometer  $z$  axis ( $z$  rotation). In addition, using  $x$  and  $y$  rotations the sample position can be optimized with respect to the azimuthal angle ( $\phi$ ) and the tilt angle ( $\psi$ ), respectively. The data collection software can use the  $x$  and  $y$  rotations to adjust the sample position during texture measurements. These five monitored rotations are shown in Fig. 3.9. The adjustment of the surface of the sample is extremely important. A change in the volume of the diffracted material resulting in a change in absorption occurs when the sample is rotated to different  $\phi$  or  $\psi$  angles.

The following experimental procedure was followed in case of a  $\theta$ - $2\theta$ -scan:

- After loading the sample, the weakest or a weak reflection of the substrate peaks (to minimize the damage of detector from a strong beam of a single crystal substrate) has been chosen from the diffraction pattern table according to the Joint Committee on Powder Diffraction Standards (JCPDS, 1995). In case of SrTiO<sub>3</sub>, this pattern is presented in Table 3.5. In the measurements of the present work, the 300 reflection was considered for SrTiO<sub>3</sub> ( $2\theta = 72.5^\circ$ ).
- The optimization of  $\phi$  and  $\psi$  angles is performed in order to record a strong contribution from the film. Fixing these two angles, the sample will then be rotated in only one direction by the variation of the  $\theta$  angle.
- The measured intensity of a  $\theta$ - $2\theta$  scan was recorded by a computer connected to the diffractometer.
- The recorded intensity was plotted and analyzed using the PC-APD 4.0 software.

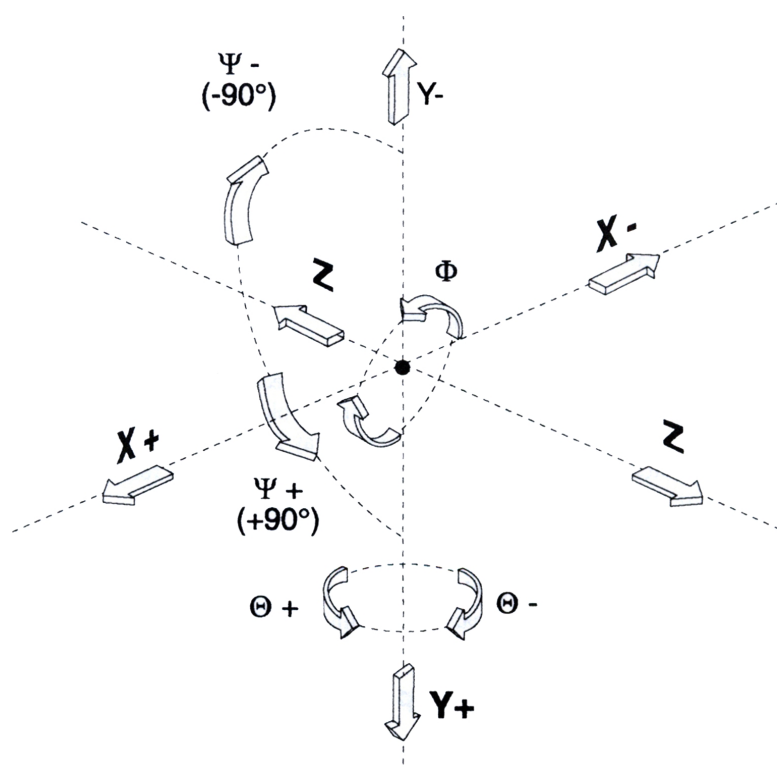


**Fig. 3.9:** The x-ray movements in order to project a set of (hkl) planes with respect to the goniometer axes  $\phi$  (azimuthal angle) and  $\psi$  (tilt angle) according to User Guide for Philips X'Pert MRD Systems, First Edition, 1995.

Finally, the identification of the crystalline planes of the film proceeds and the film orientation is determined. In order to resolve the film planes, the JCPDS data were considered again. In case of a  $\text{BaTiO}_3$  film, the diffraction pattern table is presented in Table 3.6.

Some parasitic peaks may occur in the XRD patterns due to contributions from  $\text{Cu}$  and  $\text{W}$  lines (see Table 3.7). The  $\text{Cu K}_\beta$  contribution can be excluded only by using a monochromator to eliminate the  $\text{Cu K}_\beta$  radiation. (In the present study, measurements were performed in order to get higher diffraction intensity, so that it is possible to see peaks coming from minor orientations or peaks with very low intensity, if they exist.). The  $\text{W}$  contributions are caused by an evaporation of tungsten from the filament (in the present study, a  $\text{W}$  filament was used to generate the electron beam in the x-ray tube).

In case of a  $\phi$  scan, after setting the  $\theta$  angle chosen from the film crystal structure data (which should not be close to a substrate angle) the optimization of the  $\psi$  angle is required. In order to compare the in-plane orientation of the film with the one of the substrate, a  $\phi$  scan for a substrate  $\theta$  angle is necessary. By recording  $\phi$  scans, it is possible to determine the film orientation, especially in case of epitaxial films. The  $\psi$  values presented above represent tilt angles of the sample with respect to the scattering direction and correspond to angles between two planes. Moreover, the number of peaks in  $\phi$  scans give information about the film or the substrate texture, so that one can determine the number of growth twins which can be present in the film structure. In the present study, various  $\phi$  scans were recorded at different  $\psi$  angles.

**Table 3.5:** Selected data on the SrTiO<sub>3</sub> (cubic structure - Pm3m symmetry group) diffraction pattern according to Swanson and Fuyat, Natl. Bur. Stand., Circular 539, 3, 44 (1954). Intensities are expressed as percentages of the strongest peak of the pattern.

2 $\theta$ (degree)	X-ray intensity (a.u.)	$h$	$k$	$l$	D spacing (Å)
22.783	12	1	0	0	3.900
32.424	100	1	1	0	2.7590
39.984	30	1	1	1	2.2530
46.483	50	2	0	0	1.9520
52.357	3	2	1	0	1.7460
57.794	40	2	1	1	1.5940
67.803	25	2	2	0	1.3810
72.543	1	3	0	0	1.3020
77.175	15	3	1	0	1.2350
81.721	5	3	1	1	1.1774
86.204	8	2	2	2	1.1273

Although several  $\theta$ - $2\theta$  and  $\phi$  scans are sufficient in order to determine and to confirm the film orientation with respect to the substrate orientation, it is rather difficult to determine whether the film has also other minor orientations, which can not be discriminated in a  $\theta$ - $2\theta$  scan (e.g., because of a relatively weak peak intensity or because of an overlapping of film peaks with substrate peaks). Therefore, it is necessary to record  $\phi$  scans at all  $\psi$  angles (from 0 to 90°). The result is a pole figure at a certain  $2\theta$  angle providing a chance to see other possible orientations and also to confirm the film orientation which was determined previously by recording the  $\theta$ - $2\theta$  scan.

During the pole figure measurement, the  $\theta$  angle is fixed for a chosen direction of the film crystal, and angles  $\phi$  and  $\psi$  are varied. All pole figures were plotted with the pole distance angle from  $\psi = 0^\circ$  (center) to  $\psi = 90^\circ$  (rim).  $\psi = 90^\circ$  corresponds to the substrate surface being parallel to the plane defined by the incident and reflected x-ray beams.

The FWHM values of the film used in the present study were calculated from both rocking curves and  $\phi$ -scan curves, comparing them with the FWHM of the substrate in order to evaluate the crystallinity and the in-plane alignment, respectively. This gives information about the “mozaicity” of the film.

**Table 3.6:** Selected data on the  $\text{BaTiO}_3$  (tetragonal structure -  $P4mm$  symmetry group) diffraction pattern according to Swanson and Fuyat, *Natl. Bur. Stand., Circular 539, 3, 45 (1954)*. Intensities are expressed as percentages of the strongest peak of the pattern.

$2\theta$ (degree)	X-ray intensity (a.u.)	$h$	$k$	$l$	D spacing ( $\text{\AA}$ )
22.038	12	0	0	1	4.030
22.262	25	1	1	0	3.990
31.497	100	1	0	1	2.838
31.646	100	1	1	0	2.825
38.887	46	1	1	1	2.314
44.855	12	0	0	2	2.019
45.377	37	2	0	0	1.997
50.613	6	1	0	2	1.802
50.976	8	2	0	1	1.790
51.099	7	2	1	0	1.786
55.953	15	1	1	2	1.642
56.251	35	2	1	1	1.634
65.753	12	2	0	2	1.419
66.121	10	2	2	0	1.412
70.357	5	2	1	2	1.337
70.661	2	3	0	0	1.332
74.334	5	1	0	3	1.275
75.092	7	3	0	1	1.264
75.162	9	3	1	0	1.263
78.765	3	1	1	3	1.214
79.470	5	3	1	1	1.205
83.490	7	2	2	2	1.1569
86.963	1	2	0	3	1.1194
87.385	1	[3	0	2]	1.1161
88.066	1	3	2	0	1.1082

**Table 3.7:** X-ray K-level emission lines of Cu and W according to ref. [136].

Element	Energy (keV)	$K_{\alpha 1}$ very strong	$K_{\alpha 2}$ strong	$K_{\beta}$ weak	$L_{\alpha 1}$
Cu	8.04	1.540562	1.544390	1.392218	13.336
W	58.87	0.20901	0.213828	0.184374	1.47639

### 3.3 Atomic force microscopy

An atomic force microscope (AFM) comprises two main components: the scanner and the AFM detection system. The operation principle of an AFM is based on the detection of a laser beam reflected by the edge of a soft cantilever where a sharp tip is situated (Fig. 3.10).

The cantilever oscillates in free air at its resonant frequency. A piezo stack excites the cantilever's substrate vertically, causing the tip to bounce up and down. As the cantilever bounces vertically, the reflected laser beam is deflected in a regular pattern over a photodiode array, generating a sinusoidal electronic signal. Although the piezo stack continues to excite the cantilever's substrate with the same energy, the tip is deflected in its encounter to the surface. The reflected laser beam reveals information about the vertical height of the sample surface and some characteristics of the sample materials itself, such as elasticity or the presence of magnetic and/or electric forces (Dimension 5000 Scanning Probe Microscope Instruction Manual, edited by Digital Instruments Inc., California, 1994).

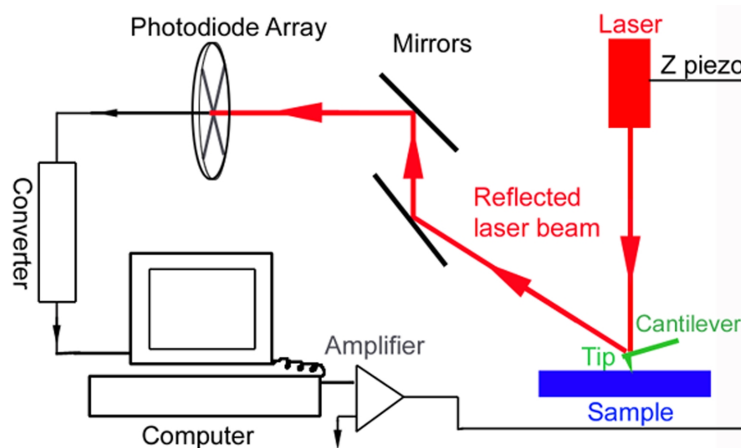


*Fig. 3.10: Principle of the AFM technique.*

An AFM can operate in two principal modes, viz. tapping (non-contact) mode and contact mode, depending on the interaction between the tip and the sample. The force between the tip and the sample is adjusted by the so-called “setpoint”. In contact mode, the tip senses the short-range repulsive forces exerted by the surface, while in tapping mode the tip senses the long-range forces approaching the sample surface. The forces act on the tip after approaching it to the surface causing a deflection of the cantilever. Usually, there are Van der Waals forces, but any other type of interaction in strong relation with the given tip and the studied sample should be taken into account. A 3D topography image of the surface can be obtained scanning the sample by keeping a constant deflection. In contact mode the tip altitude is adjusted to follow the surface height using the deflection signal, which is given by the effect of repulsive forces expressed by the cantilever bending. In tapping mode, the tip-sample forces are of attractive type, causing bending in the opposite direction than the repulsive forces. The strength of the attractive forces in tapping mode is much smaller than the repulsive forces in contact mode. Practically, the tapping mode is very easy to destabilize. If the tip meets a rough surface of the sample, the cantilever feels a higher force and bends more than before. The advantage of using the

tapping mode is due to the well-known fact that the sample surface state is not modified, while the contact mode is used nowadays to add or remove atoms from or to the sample surface. There is also a preference in using the tapping mode in order to record images of better resolution.

In this study, the surfaces of substrates and deposited films were studied by a Digital Instruments 5000 microscope working in tapping mode and using ultrasharp silicon tips. The tip characteristics are: height between 15 and 20  $\mu\text{m}$ , average resonance frequency about 350 kHz, typical force constant 40 N/m, according to the producer specifications (Silicon-MDT in cooperation with the MikroMasch company). These tips have a pyramidal shape with a radius of curvature less than 10 nm, and the full tip cone angle is less than  $20^\circ$ .

The surface roughness measured by AFM depends on the surface area, and the variation in height of the sample surface.

The root-mean-square-roughness (*RMS*) is defined as follows:

$$RMS = \sqrt{\frac{1}{N} \sum_{i=1}^N (Z_i - Z_{average})^2} \quad (3.4)$$

where  $Z_{average}$  is the average value of the height ( $Z$ ) values within the respective area,  $Z_i$  is the point height value and  $N$  is the number of points within the given area.

Some other roughness measures are considered by the AFM software, e.g. the maximum height of a given area which is calculated as the difference in height between the highest and the lowest point of the respective area.

It should be noted that the AFM images shown in the present study have been converted to planar images by “planefitting” or “flattening” (by fitting by a polynomial function with a selected order<sup>2</sup> each scan line of data which compose the final image). Then the polynomial component is subtracted from the scan line. This process is repeated for each scan line in the image eliminating the unwanted features from the scan lines, e.g. horizontal bands or image bow. The final image is a well-seen image, while the as-measured image shows a great contrast in black and white making the image not well visible. In order to give the reader the true values, all the RMS values presented in this paper are obtained for the as-measured images, even if they are included in figures together with planar images.

### 3.4 Transmission electron microscopy

Microstructure analysis of the interface between the BaTiO<sub>3</sub> film and the SrTiO<sub>3</sub> substrate, or between different layers of BaTiO<sub>3</sub>/SrTiO<sub>3</sub> multilayers was performed by cross-sectional high-resolution transmission electron microscopy (HRTEM). A JEOL 4010 electron microscope at a primary beam energy of 400 keV was used to study the interfaces.

<sup>2</sup>In the present study, only the first order of the polynomial function was consistently used. In this way, a first order least-square-fit was calculated for the selected area, then it was subtracted from each scan line of the final image preserving the image from the tall features in predominantly flat areas.

### Specimen preparation

In order to analyze the BaTiO<sub>3</sub> film deposited on a SrTiO<sub>3</sub> substrate by cross-section, specimens of these samples are prepared by polishing and ion milling techniques. The sample is cut into thin slices normal to the interfaces which are glued face-to-face. Then this sandwich is glued between two spacers which are usually pieces of SrTiO<sub>3</sub> substrates because they should have the same hardness. The whole sandwich is polished manually until the total width is about 100 μm. The specimen is then glued to a metallic grid. The next step is to thin the specimen by further dimple grinding. The specimen is then dimple-polished keeping a fixed radius of curvature in the center. A great advantage of this process is that one can control the thickness of the removed material by the depth of the dimple and interrupt the polishing when it is necessary, preventing specimen damage. Dimple-grinding both sides of the sandwich-specimen, the probability of a final perforation in the center increases. Therefore, it is preferably to polish one side and preserve the other. The final step consists of ion milling which involves bombarding the thin specimen using energetic Ar ions and remove material by sputtering until the film is thin enough to be observed in TEM. However, some implantation occurs so that the near-surface chemistry is changed. Therefore, the top layer becomes often amorphous. First, a rapid ion thinning is performed for about 2 h. After a careful investigation of the sample by an optical microscope, the last step consists of a fine polish for 4 - 7 s at 10° angle with respect to the surface (inclination helps to minimize the penetration of the ion beam) using an accelerating voltage of 2 - 4 keV. This step completes the cross-section specimen preparation for TEM investigation.

## 3.5 Electrical measurements

Pt top-electrodes with 100 nm thickness and 0.15 mm diameter were deposited by 5 min rf-sputtering through a metallic mask at 40 W power in an Ar atmosphere at room temperature. The sputtering machine uses a CESAR 133 rf-generator with a maximum frequency of 13.56 MHz and a maximum power of 300 W. Optimum power is adjusted by two variable tuning capacitors called Load ( $C_L$ ) and Tune ( $C_T$ ). In order to observe the possible fluctuations in reflected power, pre-sputtering was performed for 15 min prior to each deposition, keeping the reflected power around 1 W.

Electrical characterization was performed using a TF Analyzer 2000 ferroelectric tester (Aix-ACCT) and a Hewlett Packard HP 4195A Impedance/Gain-phase analyzer. C–V measurements were performed applying an *ac* signal with an amplitude of 10 mV at 1 MHz, while a *dc* bias was swept at a rate of 0.2 V/s from 0 to  $V_{max}$  and vice-versa with a delay time of 0.5 s. The maximum applied dc current/voltage is  $\pm 20$  mA/ $\pm 40$  V. Capacitance values were extracted from the measured absolute values of the impedance with an accuracy of 0.1% and a resolution of 4 1/2 digits. The measured capacitance was recorded applying a voltage ranging from negative values to positive values. The measured impedance values are calculated from the equivalent series circuit [ $R + jX$  or  $(R^2 + X^2)^{1/2}$ ], where  $R$  is the resistance and  $X$  is the reactance. The residual impedance was measured at 1



MHz. This value was then stored and used as offset data for subsequent measurements. The ambient temperature was considered equal to 23 °C.

# 4 Results and discussion

## 4.1 Vicinal SrTiO<sub>3</sub> substrate surfaces

### 4.1.1 General remarks

The surface state of the substrate has an important influence on the early stages of film growth. In order to properly study the growth mechanism, a well-defined reference surface morphology is required. Here, the implication that the perovskite (001) surface of ABO<sub>3</sub> perovskite single crystals either terminates by an AO plane, a BO<sub>2</sub> plane or a mixture, depending on the surface morphology, is of importance. In turn, this will affect the stacking of hetero-epitaxial perovskite thin films.

When a crystal is cut along some orientation, the atoms located in the few outer layers experience non-zero forces which are caused by the missing part of the crystal, or by the correspondingly broken bonds. Generally, the atoms do not remain at the positions fixed by the 3D-lattice. Point or extended defects may result, as well as lattice distortions. Despite of a rich literature, the structural properties of oxide surfaces are not fully elucidated. It is often difficult to prepare stoichiometric and defect-free surfaces, and the characterization is hindered by charging effects and by an uncertainty about the actual crystal termination.

A plane in a crystal is identified by three integers ( $h, k, l$ ), called the Miller indices. If several planes are structurally equivalent, as the six (100), (010), (001), ( $\bar{1}00$ ), ( $0\bar{1}0$ ), and ( $00\bar{1}$ ) planes in a cubic crystal structure like SrTiO<sub>3</sub>, this collection is denoted by  $\{100\}$  in curly brackets. However, real surfaces are rarely perfectly ordered. Depending on the conditions under which they are prepared (cutting, polishing, etc.), various defects may be found (ledges and terraces, kinks, ad-atoms, vacancies, etc.)<sup>[45]</sup> (see Fig. 4.1). For a ABO<sub>3</sub> crystal having a perovskite structure the  $\{100\}$  face is

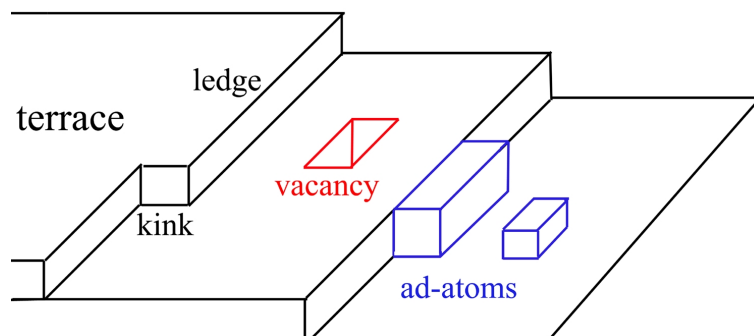


**Fig. 4.1:** Possible defects on surfaces.

the most stable surface. There exist two non-equivalent terminations with respective stoichiometries AO and BO<sub>2</sub> - i. e. SrO and TiO<sub>2</sub> for SrTiO<sub>3</sub>. In the surface layer, the transition metal cations B are five-fold coordinated, instead of six-fold in the bulk, and the cations A are surrounded by eight oxygens, instead of twelve in the bulk.

The single crystal SrTiO<sub>3</sub> substrates can be cut along the (001) plane with a small “miscut angle”<sup>1</sup> in the 010 direction. The resulting substrate surfaces consist of alternating layers of SrO and TiO<sub>2</sub> stacked in the *c*-direction ([001] direction). “Vicinal”<sup>2</sup> surfaces have terraces with regular ledges. The height of the ledges can be a multiple of the lattice cell of SrTiO<sub>3</sub> or a multiple of the half lattice cell of SrTiO<sub>3</sub>, depending on whether their terminations are TiO<sub>2</sub> or SrO. While the height of the ledge is independent of the miscut angle, the ledge density depends on the miscut angle. In fact, by increasing the miscut angle, the ledge density increases as will be shown in the next section. Smooth vicinal surfaces of the (001)-oriented SrTiO<sub>3</sub> substrates are obtained by a specific chemical and thermal treatment which will be discussed in detail in the next section.

#### 4.1.2 Preparation of vicinal SrTiO<sub>3</sub> substrate surfaces

As it was explained before, the surface state of the substrate has an important influence on the early stages of film growth. In order to properly study the growth mechanism, a substrate surface approaching a perfect substrate surface would be desired. The initial conditions for well-defined substrates before any deposition involve a clean surface and a controlled surface roughness as well as a well-defined reference surface morphology, especially when one is dealing with very thin films.

In the present study, (001)-oriented SrTiO<sub>3</sub>:Nb single crystal substrates with a Nb concentration of 0.1 wt% and a miscut angle varying from 0.1° to 1.5° were subjected to a specific chemical and thermal treatment in order to obtain vicinal surfaces with atomically flat single terminated terraces. Before and after each treatment, the surface morphology of the substrates was investigated by AFM as shown in Fig. 4.2.

For the experiments discussed in the following, only 0.1° vicinal SrTiO<sub>3</sub>:Nb substrates were chosen in order to avoid an additional parameter.

The height scale of 2 nm was consequently used for all the images included in the section of preparation of the vicinal SrTiO<sub>3</sub> substrate surfaces in order to facilitate the comparison between different topography images using different treatment parameters.

The RMS values presented in Fig. 4.2 are measured using eq. 3.4 for an given area of 2 x 2 μm<sup>2</sup> of each one of the three samples. It should be noted that all the RMS values presented in this paper are obtained for the AFM images before converting them into planar images, even if they are included in figures together with planar images.

<sup>1</sup>The *miscut angle* is defined as the angle between the actual surface plane and the (001) plane.

<sup>2</sup>The term *vicinal* defines a crystal plane whose position varies very little from that of the nearest low-index surface plane.

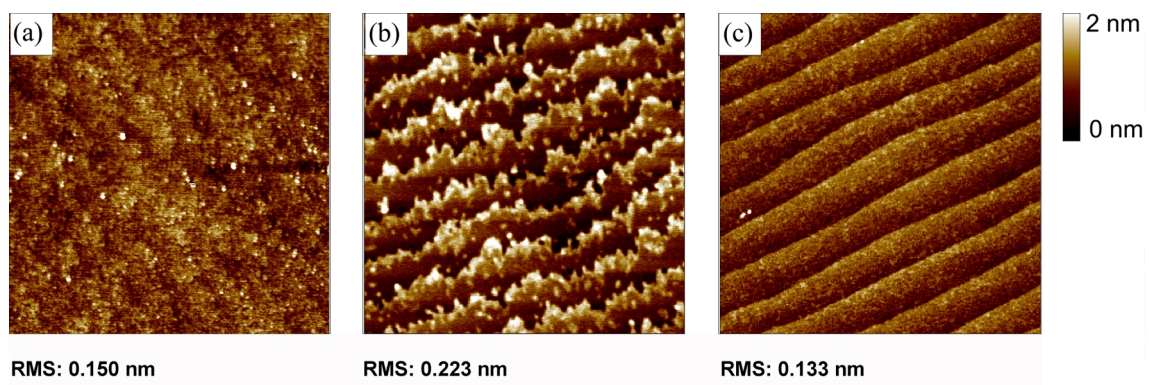


**Fig. 4.2:** AFM topography images ( $2 \times 2 \mu\text{m}^2$  area and 2 nm in height) (a) of an as-received SrTiO<sub>3</sub>:Nb substrate with  $0.1^\circ$  miscut, (b) after chemical etching by buffered hydro-fluoride (BHF) solution for 30 s, and (c) after 10 min thermal treatment at  $1200^\circ\text{C}$  following the chemical etching.

### Chemical treatment

The surface morphology of the as-received SrTiO<sub>3</sub>:Nb single crystal substrates consists of terraces with disordered steps and islands on the terraces, with typical step heights of 0.2 nm and 0.4 nm. The latter correspond to the half and the full lattice parameter of SrTiO<sub>3</sub>, which indicates the coexistence of both possible surface terminations - SrO and TiO<sub>2</sub> [Fig. 4.2(a)]. Preferably, the substrate surface has to be single terminated to impose one possible stacking sequence. Apart from this, domains with different terminations at the surface may result in different growth kinetics. From the point of view of the growth of a perfect thin film, or for a study of the growth mechanism, the simultaneous existence of both possible terminations is detrimental. It will affect any homo- or hetero-epitaxial growth process resulting in different stacking sequences within the same film.

In order to select only one possible stacking sequence of the film to be deposited, the substrate has to have a single termination<sup>[133]</sup>. Considering the coordination number of Sr (bulk 12, surface 8) and Ti (bulk 6, surface 5) in SrTiO<sub>3</sub>, it can be concluded that the TiO<sub>2</sub> surface is more stable because only fewer Ti-O bonds have to be broken in order to create the surface compared to the number of Sr-O bonds. On the other hand, shell model calculations predict a negligible difference in the surface energies of the two bulk-terminated surfaces<sup>[137]</sup>. If this is true, a surface obtained by cleaving or cutting should result in an equal amount of AO- and BO<sub>2</sub>-terminated domains separated by steps (ledges) half a unit-cell in height. The shell calculations performed by Chen *et al.*<sup>[137]</sup> indicate that for a relaxed SrO termination plane, the Sr ion is pulled out of the top plane, whereas experimentally the opposite has been observed<sup>[138]</sup>.

Because SrO is a basic oxide and TiO<sub>2</sub> is acidic, Kawasaki *et al.*<sup>[139]</sup> were able to show that by controlling the pH of the buffered hydrofluoride NH<sub>4</sub>F:HF (BHF) solution<sup>3</sup> it is possible to dissolve only one of the two atomic layers at the SrTiO<sub>3</sub> surface. Following this suggestion, in this work a chemical etching treatment was chosen to obtain only a TiO<sub>2</sub>-terminated surface [Fig. 4.2(b)].

<sup>3</sup>The pH value of BHF solution is given by a mixture of NH<sub>4</sub>F, H<sub>2</sub>O and HF used at appropriate ratios.

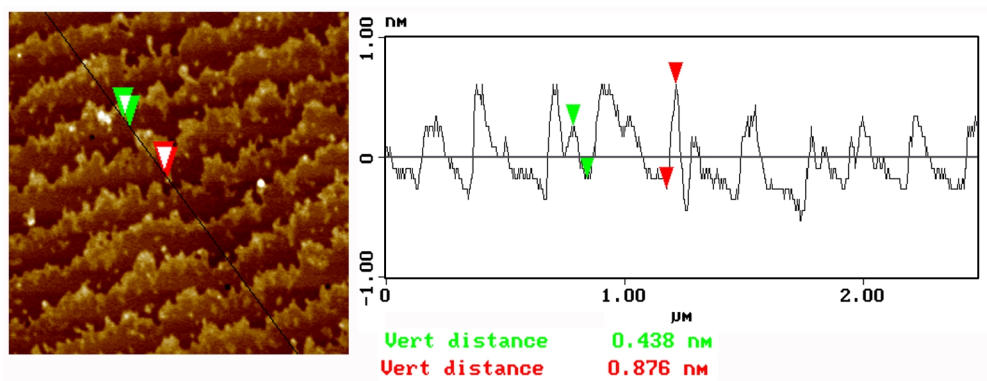


**Fig. 4.3:** AFM peak-to-valley section of a SrTiO<sub>3</sub> substrate ( $2.5 \times 2.5 \mu\text{m}^2$  area and 2 nm in height) with  $0.1^\circ$  miscut angle after a 30 s etch treatment performed in a BHF solution with pH = 4.5.

It is known that SrO reacts with H<sub>2</sub>O and CO<sub>2</sub> at room temperature forming compounds like Sr(OH)<sub>2</sub> [SrO + H<sub>2</sub>O  $\rightarrow$  Sr(OH)<sub>2</sub>] and SrCO<sub>3</sub> [Sr(OH)<sub>2</sub> + CO<sub>2</sub>  $\rightarrow$  SrCO<sub>3</sub> + H<sub>2</sub>O]. Hence, in the presence of atmospheric water the top layer of SrO forms a Sr-hydroxide compound which may be dissolved in an acid solution. Therefore, due to the enhancement of the selectivity in solubility by the formation of a Sr-hydroxide complex confined to the top SrO layer, the pH value of the BHF solution and the etching time are actually not very critical.

In this study, the SrTiO<sub>3</sub> substrates were immersed for 30 s in a BHF solution with a pH of 4.5, then rinsed with deionized water, and finally dried by blowing with dry nitrogen. The surface morphology of the substrates after chemical treatment was investigated by AFM (Fig. 4.3).

### Thermal treatment

The chemical treatment alone did not result in atomically flat substrate surfaces. Therefore, an additional thermal treatment was necessary in order to remove the remnants of the etching treatment and facilitate recrystallization.

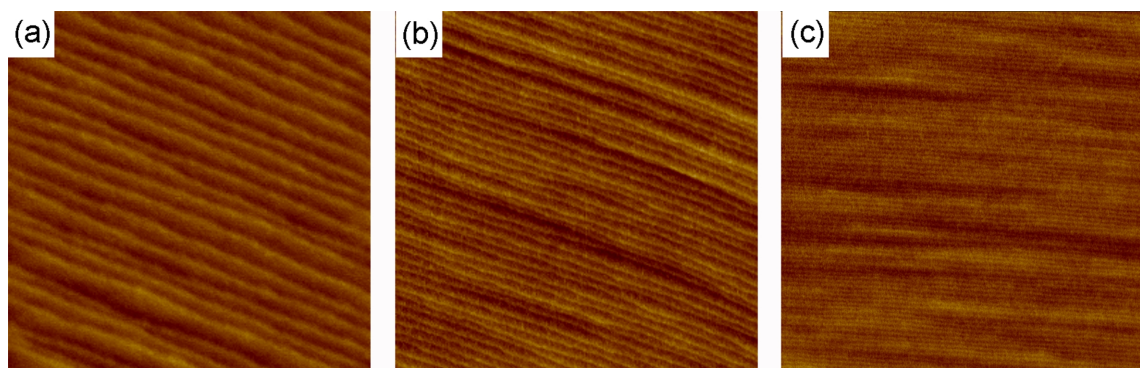


**Fig. 4.4:** AFM topography images ( $5 \times 5 \mu\text{m}^2$  area and 2 nm in height) (a) of vicinal SrTiO<sub>3</sub> substrates with (a)  $0.5^\circ$  miscut, (b)  $1^\circ$  miscut, and (c)  $1.5^\circ$  miscut. All these substrates were treated chemically and thermally.

Four different SrTiO<sub>3</sub>:Nb substrates with 0.1°, 0.5°, 1° and 1.5° miscut angles were used in the experiments of the vicinal surface preparation. Increasing the miscut angle, the density of steps increases (Figs. 4.4).

Thermal treatment experiments were performed at different temperatures, viz. 1100 °C, 1200°C, and 1300°C for 10 min or 1h.

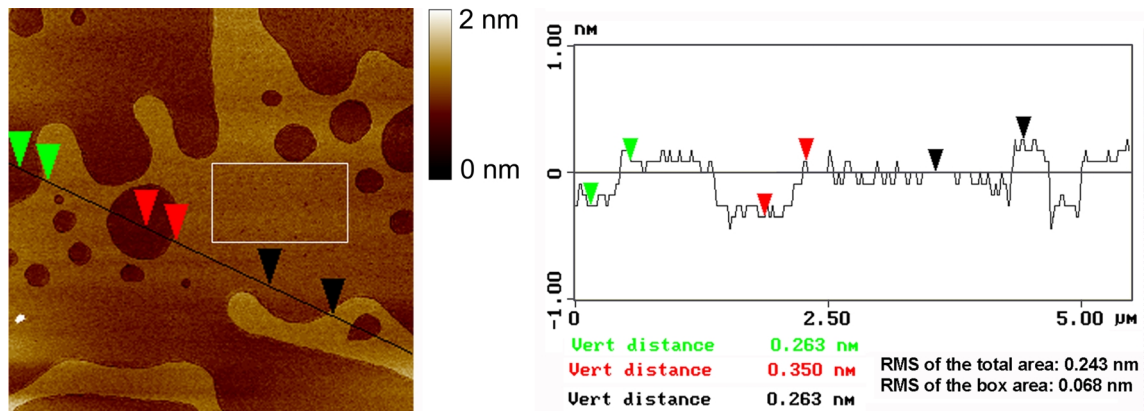


**Fig. 4.5:** AFM peak-to-valley section of a SrTiO<sub>3</sub> substrate ( $6 \times 6 \mu\text{m}^2$  area and 2 nm in height) with 0.1° miscut angle after etching and annealing treatments. Annealing treatment was performed at 1100°C for 1 h.

Meandering of step edges was observed after annealing at 1100 ° for 1 h (Fig. 4.5). In addition the formation of holes was observed on the terraces. These holes are perfectly circular shaped, one unit-cell deep and turn out to diffuse to the terrace edges with time. The terraces are about 0.4 nm in height corresponding to a full unit cell and indicating a unique surface termination. The RMS roughness on the terraces is 0.068 nm showing the smoothness of these terraces.

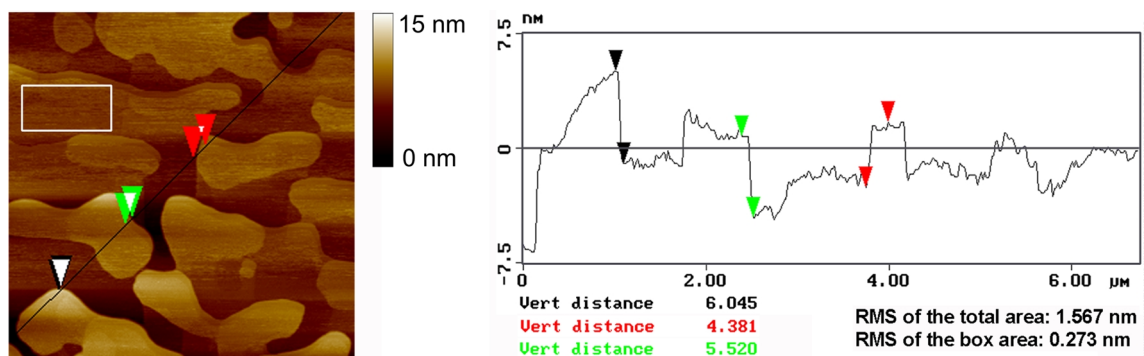


**Fig. 4.6:** AFM peak-to-valley section of a SrTiO<sub>3</sub> substrate ( $7 \times 7 \mu\text{m}^2$  area and 15 nm in height) with 0.1° miscut angle after etching and annealing treatments. Annealing treatment was performed at 1200°C for 1 h.

The changes in surface morphology become more pronounced at higher temperature or longer annealing time (Fig. 4.6). The RMS roughness of the irregularly formed terraces is still less than one single unit cell, indicating flat terraces. Overall the morphology of the SrTiO<sub>3</sub> substrate surface consists of bunching steps when the annealing treatment is performed for even longer annealing times.



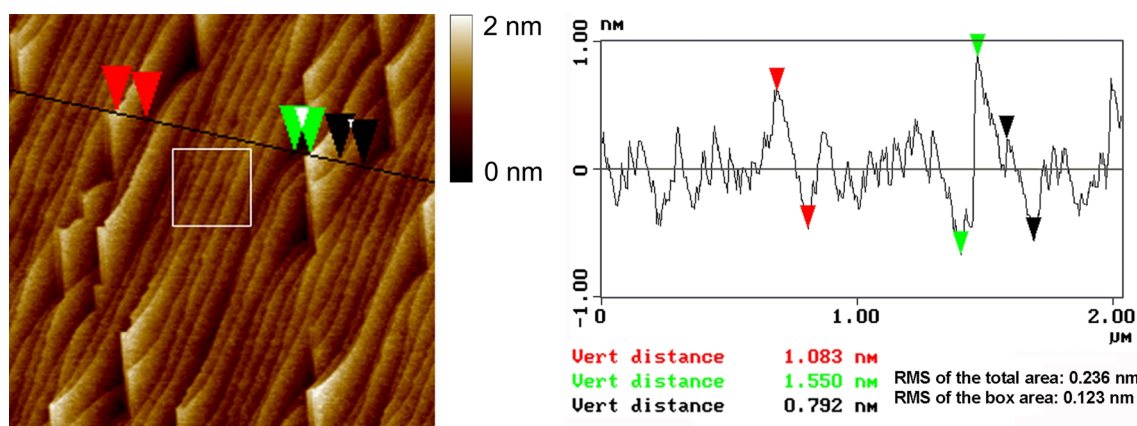


**Fig. 4.7:** AFM peak-to-valley section of a SrTiO<sub>3</sub> substrate ( $2 \times 2 \mu\text{m}^2$  area and 2 nm in height) with  $0.1^\circ$  miscut angle after etching and annealing treatments. Annealing treatment was performed at  $1300^\circ\text{C}$  for 10 min.

The differences in surface terminations are also expressed by the shape of the terrace edges. Annealing at a high temperature of  $1300^\circ\text{C}$  for 10 min results in sharp edges which are formed on the surface (Fig. 4.7). Although regular terraces form the morphology of the SrTiO<sub>3</sub> substrate surface, in this case their height varies from one to four unit cells.

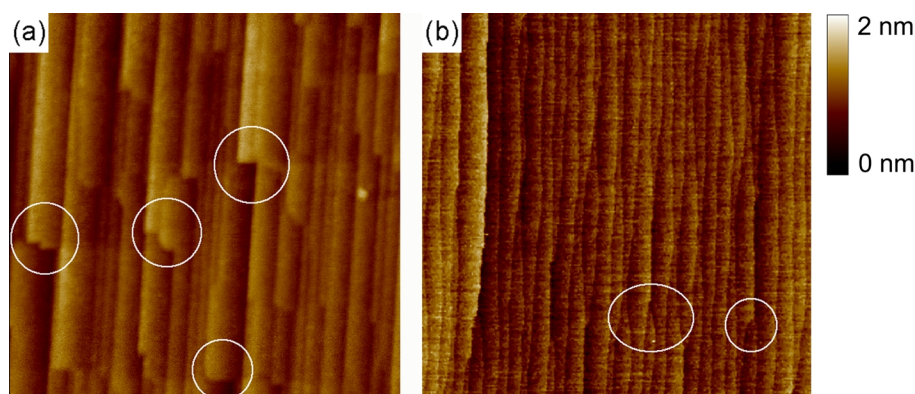


**Fig. 4.8:** AFM topography of defects appearing on vicinal SrTiO<sub>3</sub> substrates ( $5 \times 5 \mu\text{m}^2$  area and 2 nm in height) with  $0.1^\circ$  miscut angle.

Defects observed on the thermally treated surfaces include kink like termination of ledges [Fig. 4.8(a)] and extensive step bunching [Fig. 4.8(b)]. These kinds of defects were observed mainly on substrates of high miscut angle. In the literature, the formation of other phases at the surface have also been reported, especially in UHV atmosphere and at high temperatures<sup>[140, 141, 142]</sup>.

An annealing at  $1200^\circ\text{C}$  for 10 min was found to be optimal for the SrTiO<sub>3</sub>:Nb substrates used in this study. The surface morphology of the vicinal substrates treated chemically and thermally following the optimal procedure consists of well-defined terraces of a width of 150 nm to 250 nm with straight and sharp terrace edges [Fig. 4.2(c)]. The height of the steps is 0.4 nm which corresponds to one unit cell of SrTiO<sub>3</sub>, indicating a unique surface termination. AFM analysis shows a nearly perfect single-terminated surface with very straight terrace edges (Fig. 4.9). The scan-line shows only single

unit-cell steps of SrTiO<sub>3</sub>. Typical for these surfaces is their homogeneous morphology. As one can see in a non-flat image (not shown), the terrace edges are round features which can be associated with the minimization of the edge energy by decreasing the surface area of the step<sup>[138]</sup>.

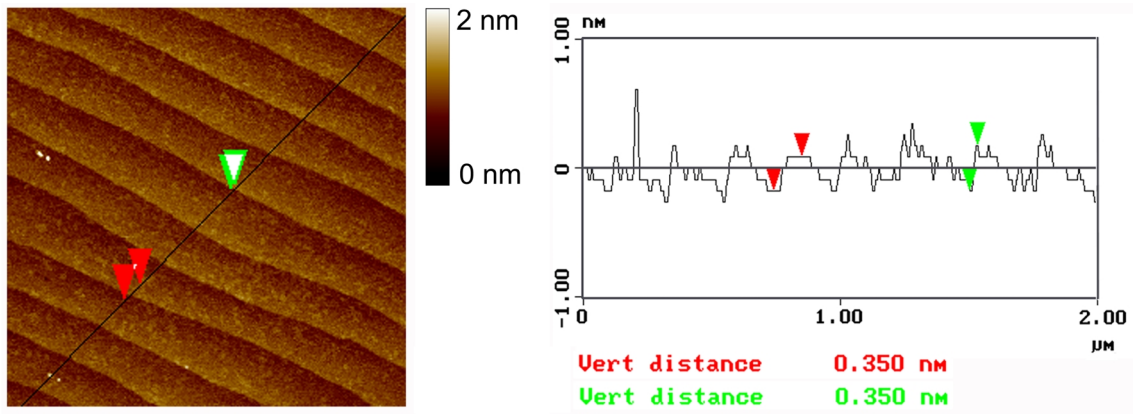


**Fig. 4.9:** AFM peak-to-valley section of a SrTiO<sub>3</sub> substrate ( $2 \times 2 \mu\text{m}^2$  area and 2 nm in height) with  $0.1^\circ$  miscut angle after etching and annealing treatments. Annealing treatment was performed at  $1200^\circ\text{C}$  for 10 min.

It turned out that the success of this thermal treatment depends on the annealing temperature and annealing time. Preparation of single terminated SrTiO<sub>3</sub> (001)-oriented substrate surfaces of a miscut angle of  $0.1^\circ$  with regular and sharp edge terraces was performed by controlling rigorously the above mentioned parameters.

In order to have a unique surface as reference for further thin film deposition, vicinal SrTiO<sub>3</sub> substrate surfaces with  $0.1^\circ$  miscut angle have been used for thin film deposition. Owing to the structural compatibility and close lattice match, it was possible to grow high quality epitaxial BaTiO<sub>3</sub> films onto atomically flat, vicinal SrTiO<sub>3</sub> (001)-oriented substrates by PLD.



## 4.2 Epitaxial BaTiO<sub>3</sub> thin films

### 4.2.1 Initial growth stages of BaTiO<sub>3</sub> thin films on SrTiO<sub>3</sub> surfaces

The details of the growth of epitaxial BaTiO<sub>3</sub> thin films are generally influenced by a number of parameters including growth method, substrate temperature, oxygen pressure, film thickness, and lattice mismatch. This requires a comprehensive analysis of the growth mechanism including detailed studies of the *initial growth stages*. As BaTiO<sub>3</sub> is considered to be the prototype of perovskite ferroelectrics, considerable attention has been given so far to the properties of as-grown and/or annealed films explaining them in terms of advanced growth or (re)crystallization stages, while the initial stages of film growth including the growth mechanism have up to now not been studied in sufficient detail. In the literature, there are only few studies on the initial growth stages of complex oxides. The growth mechanism in the BaTiO<sub>3</sub>/SrTiO<sub>3</sub> system is still contradictory. It is still not clarified whether BaTiO<sub>3</sub> is growing in a layer-by-layer growth mode<sup>[6]</sup> or in an island growth mode<sup>[9]</sup> on SrTiO<sub>3</sub> substrates when grown by PLD. Layer-by-layer growth has been shown to be a principally possible growth mechanism taking into account the binding energies between layer and substrate obtained by theoretical electronic structure calculations and taking into account the surface charge neutrality<sup>[10]</sup>.

Epitaxial BaTiO<sub>3</sub> thin films with *nominal thickness*<sup>4</sup> from 1 nm to 1 μm were deposited onto the chemically and thermally treated vicinal SrTiO<sub>3</sub>:Nb substrates. The surfaces of the deposited films were studied by AFM, and their structure by cross-sectional high-resolution TEM. The results will be discussed as a function of the nominal thickness, starting with the 1 nm thick film and increasing the thickness<sup>5</sup>. In case of relatively thick films, the thickness of the BaTiO<sub>3</sub> films was measured first by profilometer and then confirmed by cross-sectional TEM analysis. In case of thin films, the profilometer measurement could not be performed and the thickness was measured only by cross-sectional TEM. An overview of the evolution of the morphology of the BaTiO<sub>3</sub> films with increasing thickness is shown in Fig. 4.10 and can be summarized as follows:

- up to 1 nm, a grainy layer uniformly covers the substrate, with the terrace steps still being visible [Fig. 4.10(a)];
- at 5 nm, individual grains become visible [Fig. 4.10(b)];
- up to 25 nm, the density of those small grains increases [Figs. 4.10(c)-(f)];
- at 40 nm, some of these small grains grow further into larger grains [Fig. 4.10(g)];

---

<sup>4</sup>The *nominal thickness* is defined as the typical thickness the film would have if it would grow in the layer-by-layer mode, thus being a measure of the amount of deposited material.

<sup>5</sup>It should be noted that the experimental study was performed starting with relatively thick films and ending with a nominal thickness of the BaTiO<sub>3</sub> film of 1 nm by reducing gradually the thickness of the deposited material. In order to give the reader a better understanding of the initial growth stages of BaTiO<sub>3</sub> films grown on (001)-oriented SrTiO<sub>3</sub> substrates, this order is here inverted.

- further on, up to 260 and 320 nm, the film morphology does not principally change [Figs. 4.10(k) and 4.10(l)].

The above results suggest a Stranski-Krastanov growth mechanism of BaTiO<sub>3</sub> on SrTiO<sub>3</sub>. In the early growth stage, a very thin, complete BaTiO<sub>3</sub> layer uniformly covers the substrate surface. As

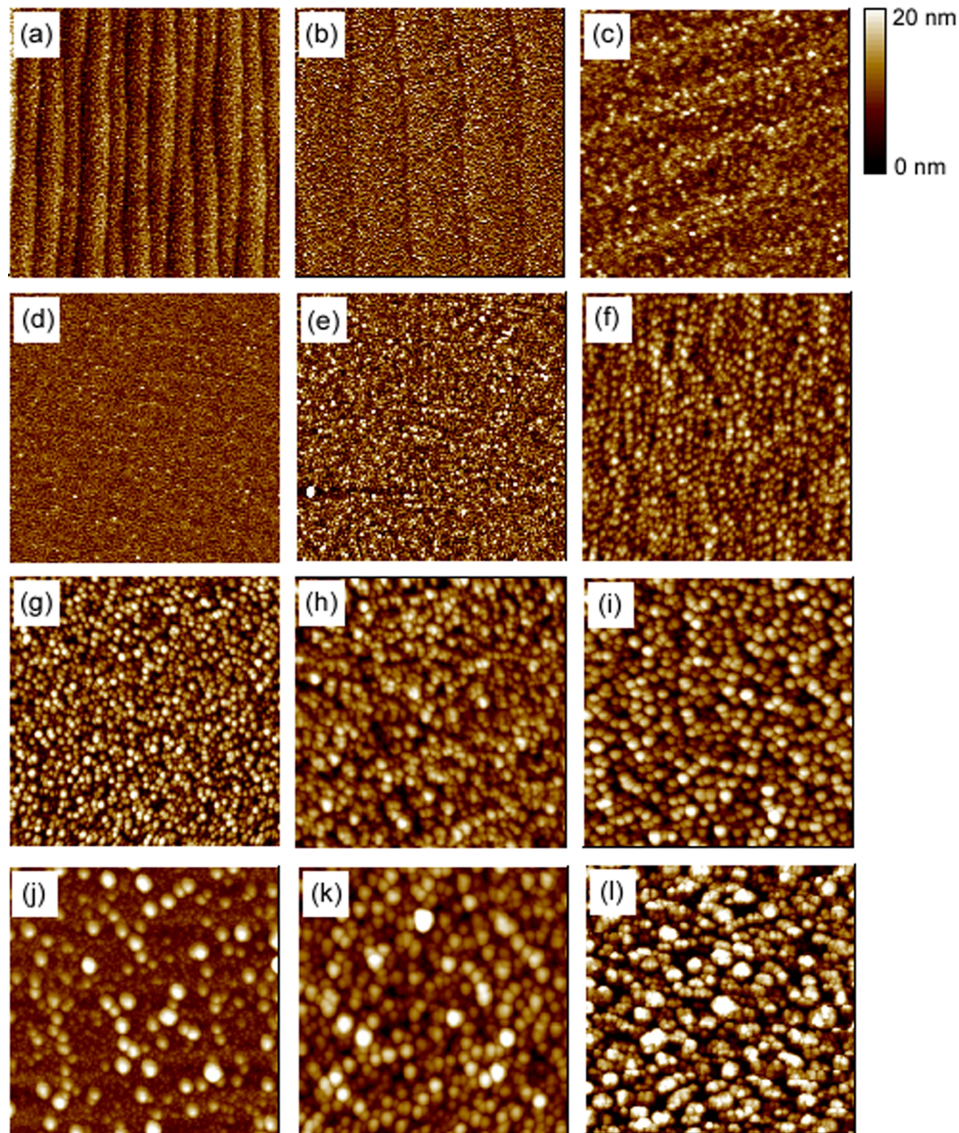


**Fig. 4.10:** AFM topography images of epitaxial BaTiO<sub>3</sub> films ( $2 \times 2 \mu\text{m}^2$  area and 20 nm in height) deposited on vicinal SrTiO<sub>3</sub>:Nb substrates. Different deposition times of 0.2, 1, 2, 5, 10, 15, 20, 25, 30, 45, 60, and 180 min were used to grow films having nominal thicknesses of (a) 1, (b) 5, (c) 10, (d) 15, (e) 20, (f) 25, (g) 40, (h) 75, (i) 110, (j) 150, (k) 260, and (l) 320 nm, respectively.

described in the previous section of this chapter, the terrace height of the initial vicinal substrate surface corresponded to one lattice constant of SrTiO<sub>3</sub> (0.4 nm). After deposition of 1 nm of BaTiO<sub>3</sub>, the terraces are still visible. The surface is now covered with BaTiO<sub>3</sub>, and the step height has now been determined to be between 0.44 and 0.53 nm. This indicates that BaTiO<sub>3</sub> units are added not only along the terrace edges, but also on the terraces. Generally, a model of film formation can be

as follows: When the diffusing ad-atoms encounter a terrace<sup>[143]</sup>, they can either be reflected and remain on the same terrace, or go across the terrace and be incorporated into sites at the terrace edges (see Fig. 4.11). If all the terraces are non-reflective for the diffusing ad-atoms or clusters, the growth

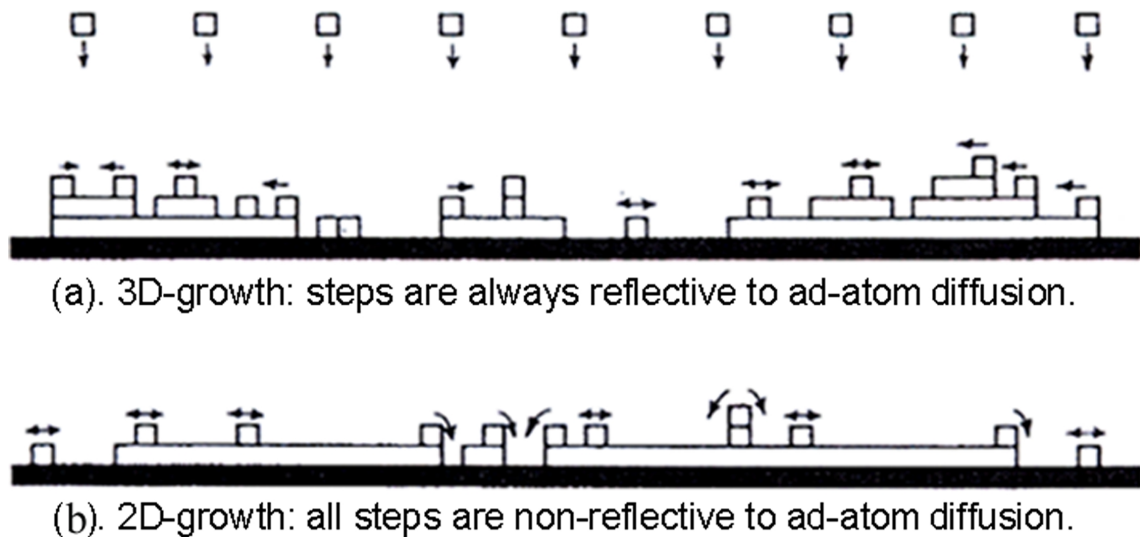


**Fig. 4.11:** Different growth modes on terraces during heteroepitaxial growth, adapted after Ref.<sup>[143]</sup>.

process will be 2D, because atoms will be attached to the edges of the terraces where the energy is at minimum. Alternatively, if the terraces are reflective, the atoms diffuse on the terraces finally covering the entire surface with a very thin uniform layer. Since after deposition of 1 nm of BaTiO<sub>3</sub>, the terrace height has increased with respect to the height before deposition, but by only 0.1 nm and not by 1 nm, both these processes should have occurred in this case. In this study, the roughness of the initial SrTiO<sub>3</sub> surface was about 0.133 nm, while after 1 nm deposition of BaTiO<sub>3</sub> the roughness was only slightly increased up to 0.164 nm, indicating a smooth top-surface of the BaTiO<sub>3</sub> layer (Fig. 4.12).

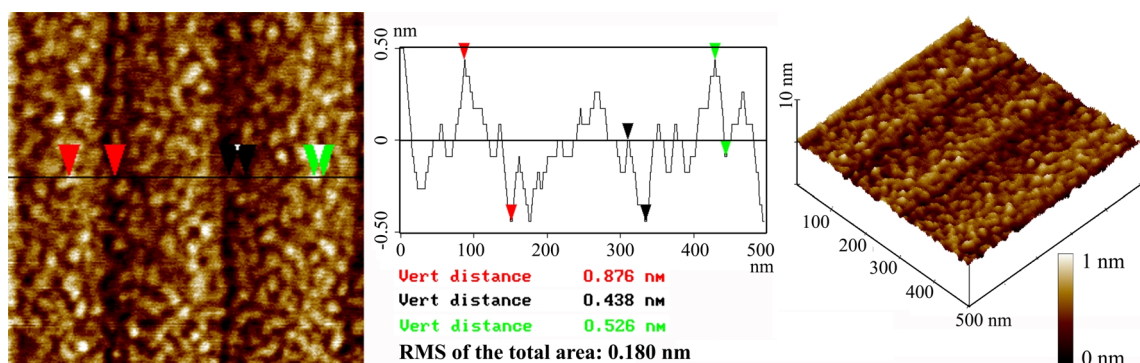


**Fig. 4.12:** Zoom-in topography image ( $0.5 \times 0.5 \mu\text{m}^2$  area and 1 nm in height) of the nominally 1 nm thick BaTiO<sub>3</sub> film presented in Fig. 4.10(a).

A close inspection of the topography of the 1 nm thick BaTiO<sub>3</sub> film surface showed that the terrace edges are not very well defined. This shows that the BaTiO<sub>3</sub> layer partially covers also the terrace



edges, and not only the top surface of the terrace. The maximum peak-to-valley height<sup>6</sup> on the terrace edge is 0.876 nm, again less than the film thickness, confirming that the BaTiO<sub>3</sub> layer is continuous. In fact, this continuous uniform layer is a grainy layer composed by small grains with a height of about 0.5 nm, formally corresponding to one and half unit cell of BaTiO<sub>3</sub>. Knowing that the vicinal SrTiO<sub>3</sub> surface is TiO<sub>2</sub> terminated, one can assume that the one and half unit cells of BaTiO<sub>3</sub> actually form a BaO terminated BaTiO<sub>3</sub> film (Fig. 4.13). One should, however, also take into account the accuracy of the AFM measurement at this very low height. Indeed, the 0.16 nm average roughness can be correlated with half of a BaTiO<sub>3</sub> unit cell leaving the possibility that the grainy BaTiO<sub>3</sub> layer which covers the substrate surface is terminated with both possible terminations - BaO and TiO<sub>2</sub>.

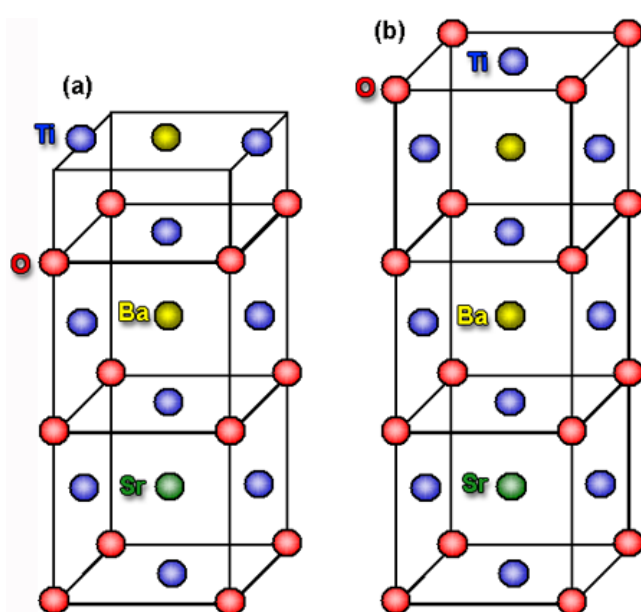


**Fig. 4.13:** Model of different terminations of the BaTiO<sub>3</sub> layer grown on a TiO<sub>2</sub>-terminated SrTiO<sub>3</sub> substrate surface: (a) BaO - termination (one and half BaTiO<sub>3</sub> unit cell in thickness) and (b) TiO<sub>2</sub> - termination (two BaTiO<sub>3</sub> unit cells in thickness).

Cross-sectional TEM investigations confirm the conclusions drawn from the AFM investigations. Figure 4.14 shows a HRTEM image of an epitaxial BaTiO<sub>3</sub> film of 1 nm in nominal thickness. The film/substrate interface is well-defined and sharp. A uniform continuous BaTiO<sub>3</sub> layer is observed confirming that the initial growth mode is layer-by-layer growth.

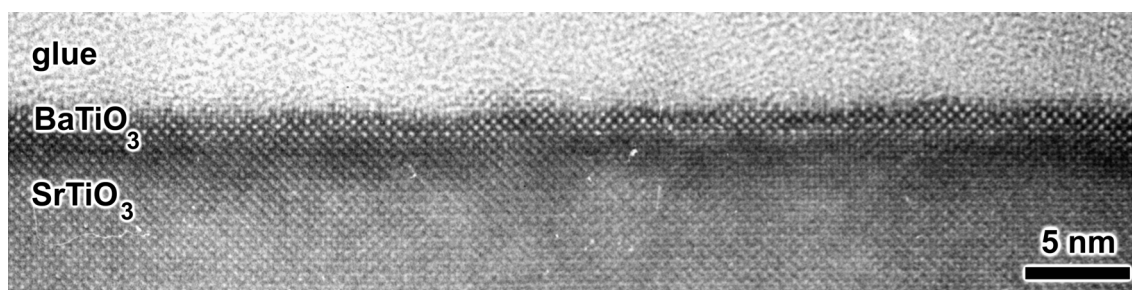


**Fig. 4.14:** Cross-sectional HRTEM image of an epitaxial BaTiO<sub>3</sub> thin film of 1 nm nominal thickness deposited on a vicinal SrTiO<sub>3</sub>:Nb substrate by PLD.

<sup>6</sup>The peak-to-valley height was measured from the highest point to the lowest point of the scan line.

As already mentioned, the layer-by-layer growth was shown to be a possible growth mechanism for BaTiO<sub>3</sub> by theoretical electronic structure calculations taking into account the surface charge neutrality<sup>[10]</sup>. Molecular dynamics simulations were performed by Wunderlich *et al.*<sup>[144]</sup>. He found a critical thickness, at which the growth mechanism changes from pseudomorphic growth without defects to a relaxed epitaxial film by introducing misfit dislocations, and estimated this critical thickness to be at about four monolayers. Since no evidence for the presence of misfit dislocations was found in the 1 nm thin BaTiO<sub>3</sub> film shown in Fig. 4.14, this observation is in good agreement with the molecular dynamics simulations performed by Wunderlich. The 1 nm thickness of the BaTiO<sub>3</sub> film is well below the critical thickness of four unit cells (about 1.6 nm).

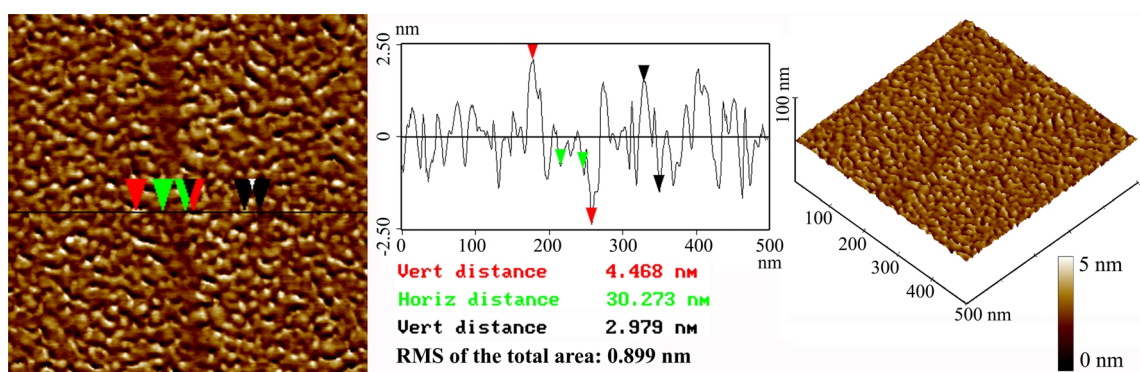


**Fig. 4.15:** Zoom-in topography image ( $0.5 \times 0.5 \mu\text{m}^2$  area and 5 nm in height) of the nominally 5 nm thick BaTiO<sub>3</sub> film presented in Fig. 4.10(b).

At a film thickness of about 5 nm, small nuclei start to grow on top of the previous uniform “wetting” layer. The RMS roughness of the film surface suddenly increases up to 0.847 nm ( $\approx 2$  unit cells of BaTiO<sub>3</sub>) in an area including the terrace edge, while on the terrace it reaches 0.480 nm ( $\approx 1$  unit cell of BaTiO<sub>3</sub>), indicating almost one unit cell difference in height between the top surface of the terraces and the terrace edge. The terraces are covered with small grains leaving the terrace steps still visible. Again, the terrace edges are not straight having a width of about 30 nm (Fig. 4.15), the terrace width being about 500 nm in this case.

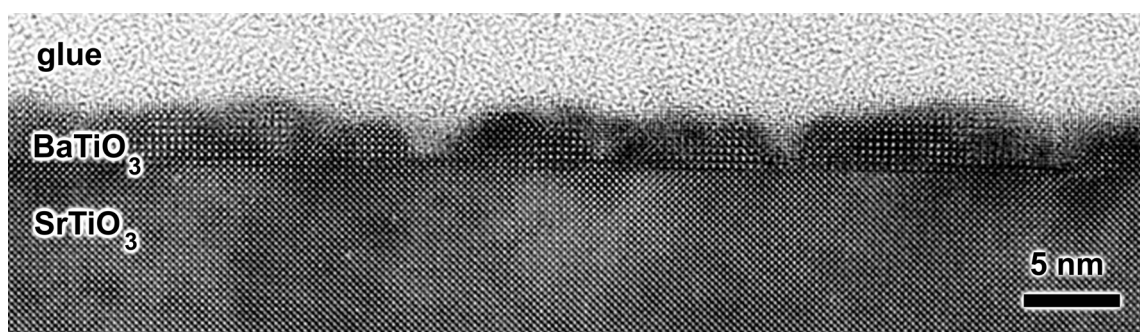


**Fig. 4.16:** Cross-sectional HRTEM image of an epitaxial BaTiO<sub>3</sub> thin film of nominal 5 nm thickness deposited on a vicinal SrTiO<sub>3</sub>:Nb substrate by PLD.

The height of the individual grains is about 3 nm, and they have a lateral size of about 5 nm. These values were measured first by AFM and then confirmed by the cross-sectional high-resolution TEM investigations.

Fig. 4.16 shows the continuous layer and the small grains on top of it. The continuous layer is two unit cells in height, thus corresponding to the 1 nm thick BaTiO<sub>3</sub> film shown in Fig. 4.14. This layer represents a continuous template for the grains which are growing on top of it. Their height is about 3 to 4 nm, and their lateral size is of the order of 5 nm.

Obviously, the thickness of 5 nm represents the turning point, when individual grains begin to grow, and the film stress relaxes.

Further on, on the 10 nm thick BaTiO<sub>3</sub> film terraces are still visible and small islands are uniformly distributed on the surface [see Fig. 4.10(c)]. Their density is, however, larger compared with the previous stage. Their height varies from 2 to 4 nm and their lateral size is about 60 nm. The maximum peak-to-valley height measured by AFM on the 10 nm thick BaTiO<sub>3</sub> film surface is 3.85 nm confirming again that now an island growth has developed on top of the previous smooth layer.

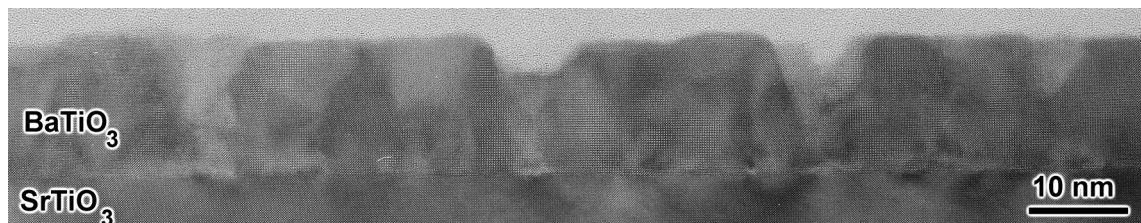


**Fig. 4.17:** Cross-sectional HRTEM image of an epitaxial BaTiO<sub>3</sub> thin film of 10 nm thickness deposited on a vicinal SrTiO<sub>3</sub>:Nb substrate by PLD.

Cross-sectional HRTEM investigations (Fig. 4.17) confirm that the height of the grains has increased compared to the earlier stage of a nominal thickness of 5 nm.

The density of the grains increases by further deposition, as shown by the film of 15 nm nominal thickness [see Fig. 4.10(d)].

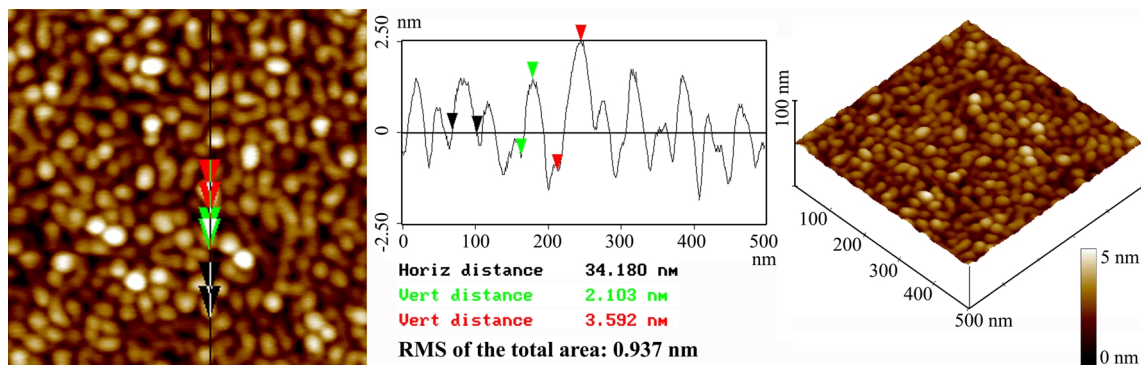


**Fig. 4.18:** Zoom-in topography image ( $0.5 \times 0.5 \mu\text{m}^2$  area and 5 nm in height) of the 20 nm thick BaTiO<sub>3</sub> film presented in Fig. 4.10(c).



In addition, for 20 nm nominal thickness, terraces are fully covered and no edges are visible any more [see Fig. 4.10(e)]. The increase of the film roughness is a common feature of the films deposited by PLD and it will be discussed later considering the thickness-dependence on the average RMS roughness. Island dimensions are now about 35 nm in lateral size and their height varies between 3.5 nm and 5 nm (Fig. 4.18).

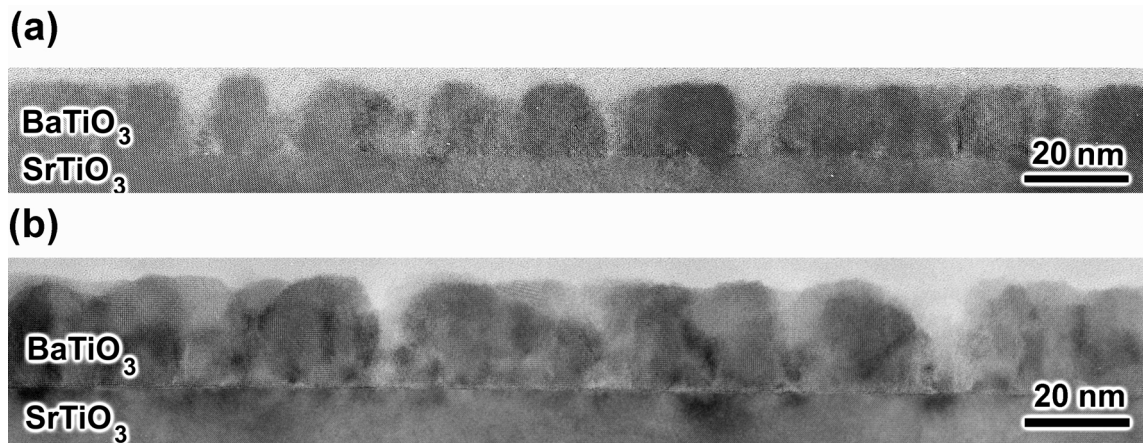


**Fig. 4.19:** Cross-sectional HRTEM images of an epitaxial BaTiO<sub>3</sub> film deposited on a vicinal SrTiO<sub>3</sub>:Nb substrate and having (a) 20 nm and (b) 25 nm in nominal thickness.

More information about the grains was obtained by HRTEM. Their density increased from the growth stage of 20 nm nominal thickness [Fig. 4.19(a)] to that of 25 nm nominal thickness [Fig. 4.19(b)].

### 4.2.2 Analysis of the crystallographic orientation

Crystallographic analyses were performed by XRD  $\theta$ - $2\theta$  and  $\phi$  scans and by pole figures in order to globally demonstrate the epitaxial relationship between the BaTiO<sub>3</sub> film and the SrTiO<sub>3</sub> substrate. It is well known that BaTiO<sub>3</sub> has a tetragonal structure and SrTiO<sub>3</sub> has a cubic structure. The  $a$ -orientation

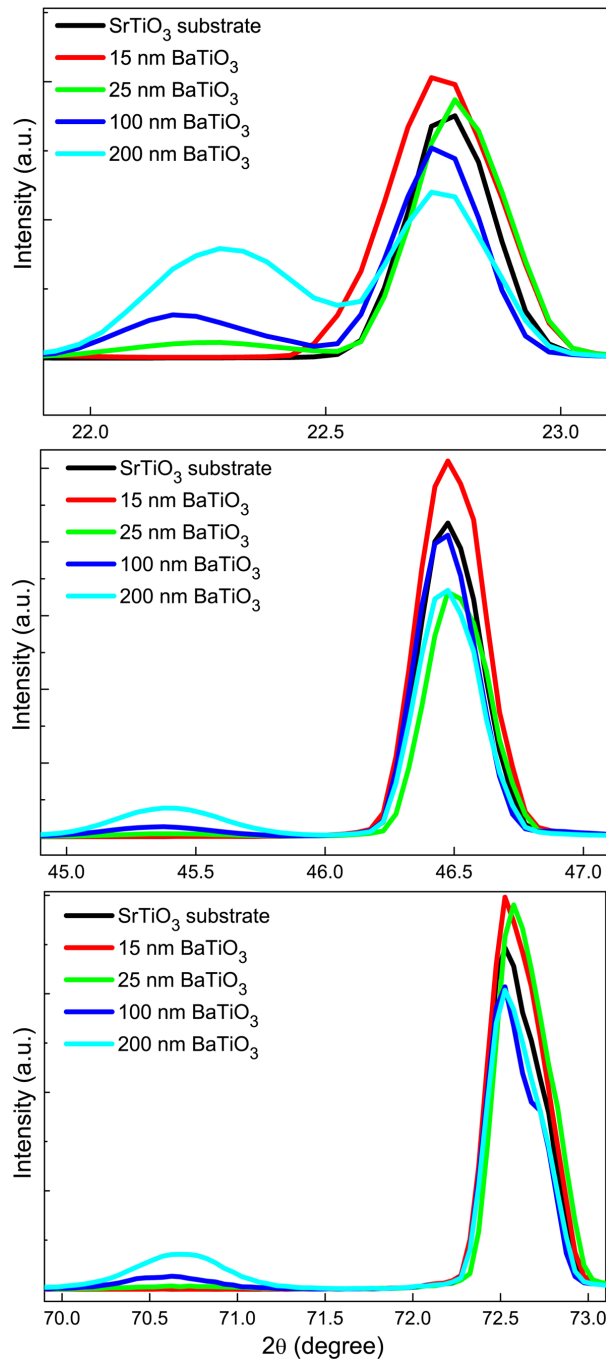


**Fig. 4.20:** Zoom into the XRD  $\theta$ - $2\theta$  scan (in linear scale) of epitaxial BaTiO<sub>3</sub> films with nominal thicknesses of 15, 25, 100 and 200 nm for the 001/100, 002/200, and 300/003 couples of peaks.

is defined as follows:

$$(100) \text{ BaTiO}_3 \parallel (001) \text{ SrTiO}_3; [001] \text{ BaTiO}_3 \parallel [100] \text{ SrTiO}_3 \quad (4.1)$$



The  $c$ -orientation is defined as follows:

$$(001) \text{ BaTiO}_3 \parallel (001) \text{ SrTiO}_3; [100] \text{ BaTiO}_3 \parallel [100] \text{ SrTiO}_3 \quad (4.2)$$

Unfortunately below a nominal thickness of 25 nm it is difficult to perform XRD measurements, because the BaTiO<sub>3</sub> diffraction peaks are very close to the SrTiO<sub>3</sub> peaks and the intensity of the BaTiO<sub>3</sub> peaks is very low. In fact the difference angle between the 100 peak of BaTiO<sub>3</sub> and the 100 peak of SrTiO<sub>3</sub> is only 0.521°, and the difference angle between the 200 peak of BaTiO<sub>3</sub> and the 200 peak of SrTiO<sub>3</sub> is only 1.106°. The difference angle between the 300 peak of BaTiO<sub>3</sub> and the 300 peak of SrTiO<sub>3</sub> is 1.882°. Fig. 4.20 presents the x-ray  $\theta$ - $2\theta$  scan for different thicknesses of the BaTiO<sub>3</sub> films. Below a nominal thickness of 25 nm, the BaTiO<sub>3</sub> peaks are shoulders of the corresponding SrTiO<sub>3</sub> peaks. Another inconvenience is the low intensity of the BaTiO<sub>3</sub> peaks in comparison with the substrate peaks. Also it is impossible to distinguish between  $a$ -orientation and  $c$ -orientation of BaTiO<sub>3</sub>, because the difference is less than 1°, exactly 0.224° between the 100 peak and the 001 peak and 0.522° between the 200 peak and the 002 peak.

In addition to the XRD  $\theta$ - $2\theta$  scans presented above, various pole figure analyses were performed to confirm the crystallographic orientation (Fig. 4.21). The simple fourfold symmetry shown in Fig. 4.21(a) was obtained for the 110 reflection of BaTiO<sub>3</sub> which is very close to the 101 reflection (see Table 3.6 in the previous chapter). A more complicated fourfold symmetry is shown in Fig. 4.21(b) which was recorded for the 211 reflection of BaTiO<sub>3</sub> which is very close to the 112 reflection (see Table 3.6). The symbols  $\ast\{112\}\ast$  and  $\ast\{211\}\ast$  are explained in Table 4.1.

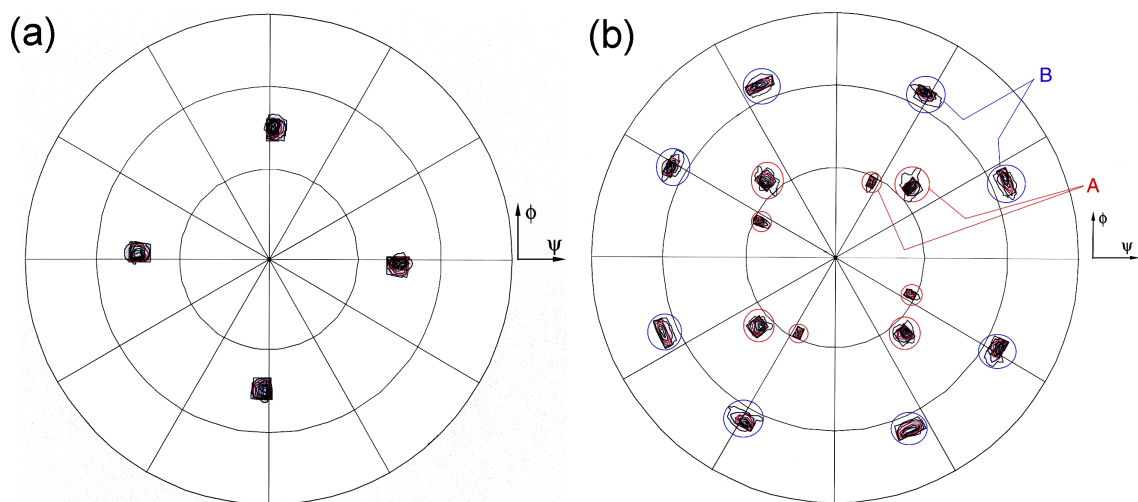


**Fig. 4.21:** XRD pole figures of a nominally 25 nm thick BaTiO<sub>3</sub> film grown on SrTiO<sub>3</sub> (001). (a) The fixed  $2\theta$  angle was 31.65° corresponding to the 110 reflection of BaTiO<sub>3</sub>. (b) The fixed  $2\theta$  angle was 56.25° corresponding to the 211 reflection of BaTiO<sub>3</sub> which is very close to the 112 reflection. The A and B symbols are explained in Table 4.1.

**Table 4.1:** Possible reflections in the pole figure of Fig. 4.21(b). The symbol  $\ast\{112\}\ast$  comprises the reflections  $112$ ,  $1\bar{1}2$ ,  $11\bar{2}$ , and  $1\bar{1}\bar{2}$ , and the symbol  $\ast\{211\}\ast$  comprises the reflections  $211$ ,  $2\bar{1}1$ ,  $21\bar{1}$ , and  $2\bar{1}\bar{1}$ .

Symbol	$c$ -orientation	$a$ -orientation
A	$\ast\{112\}\ast$ ( $\psi = 35.56^\circ$ )	$\ast\{211\}\ast$ ( $\psi = 35.117^\circ$ )
B	$\ast\{211\}\ast$ ( $\psi = 66.138^\circ$ )	$\ast\{112\}\ast$ ( $\psi = 65.717^\circ$ )

Those symbols are used in order to define all possible reflections in case of the 211/112 reflection of BaTiO<sub>3</sub> taking into account that it is impossible to distinguish between the (100) and (001) orientations of the BaTiO<sub>3</sub> film (see Table 4.2). The pole figures confirm that the entire BaTiO<sub>3</sub> film has grown epitaxially, i.e. with the same crystallographic orientation everywhere.

**Table 4.2:** Angles between different reflections considered for (100) and/or (001)-oriented BaTiO<sub>3</sub> film grown on SrTiO<sub>3</sub>.

angle(°)			angle(°)		
{001}	{211}	35.117	{001}	{211}	66.138
	{ $\bar{2}11$ }	144.88		{ $\bar{2}11$ }	66.138
	{ $2\bar{1}1$ }	35.117		{ $2\bar{1}1$ }	66.138
	{ $21\bar{1}$ }	35.117		{ $21\bar{1}$ }	113.861
	{ $\bar{2}\bar{1}1$ }	144.88		{ $\bar{2}\bar{1}1$ }	66.138
	{ $\bar{2}\bar{1}\bar{1}$ }	144.88		{ $\bar{2}\bar{1}\bar{1}$ }	113.861
	{ $2\bar{1}\bar{1}$ }	35.117		{ $2\bar{1}\bar{1}$ }	113.861
	{100}			{001}	
{112}	65.717	{112}	35.56		
{ $\bar{1}12$ }	114.282	{ $\bar{1}12$ }	35.56		
{ $1\bar{1}2$ }	65.717	{ $1\bar{1}2$ }	35.56		
{ $11\bar{2}$ }	65.717	{ $11\bar{2}$ }	144.439		
{ $\bar{1}\bar{1}2$ }	114.282	{ $\bar{1}\bar{1}2$ }	35.56		
{ $\bar{1}\bar{1}\bar{2}$ }	114.282	{ $\bar{1}\bar{1}\bar{2}$ }	144.439		
{ $1\bar{1}\bar{2}$ }	65.717	{ $1\bar{1}\bar{2}$ }	144.439		

Further on,  $\phi$  scans of the BaTiO<sub>3</sub> film and the SrTiO<sub>3</sub> substrate, respectively (Fig. 4.22) were recorded in order to establish the in-plane orientation relationships of the BaTiO<sub>3</sub> film with respect to the underlying SrTiO<sub>3</sub> substrate. Three  $\phi$  scans were recorded from the same sample with 25 nm nominal BaTiO<sub>3</sub> film thickness<sup>7</sup> grown on SrTiO<sub>3</sub> (001) using the SrTiO<sub>3</sub> 222 reflection ( $2\theta = 86.2^\circ$  and  $\psi = 54.6^\circ$ ), the BaTiO<sub>3</sub> 211 reflection ( $2\theta = 56.2^\circ$  and  $\psi = 34.9^\circ$ ), and the BaTiO<sub>3</sub> 110 reflection ( $2\theta = 31.6^\circ$  and  $\psi = 45.0^\circ$ ). The  $\phi$  scans using the 211 and 110 reflections include also

<sup>7</sup>As it was mentioned before, the 25 nm represent the minimum thickness of the BaTiO<sub>3</sub> film from which diffraction patterns can be distinguished.

the contribution from the 112 ( $2\theta = 55.9^\circ$ ) and 101 ( $2\theta = 31.5^\circ$ ) reflections of the other orientation (*c*- vs. *a*-orientation), respectively, since these are close to each other. The peaks from BaTiO<sub>3</sub> (110)

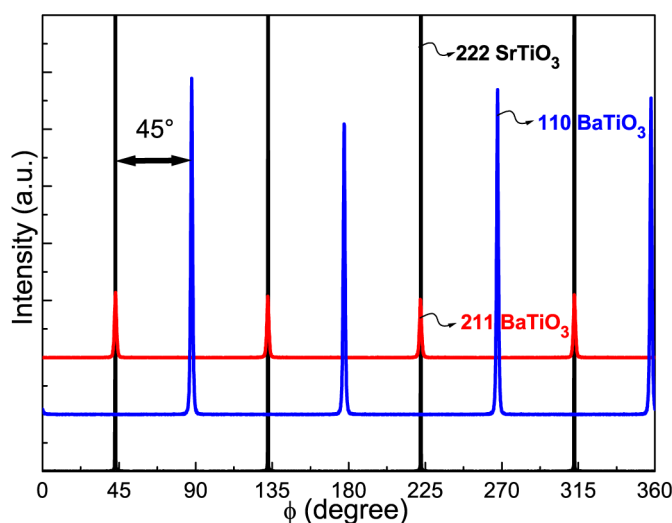


*Fig. 4.22: XRD  $\phi$  scan of a nominally 25 nm thick BaTiO<sub>3</sub> film grown on SrTiO<sub>3</sub> (001). These plots were recorded using the 222 reflection of the SrTiO<sub>3</sub> substrate, and the 112/211 and 101/110 reflections of the BaTiO<sub>3</sub> film.*

are delayed by  $45^\circ$  with respect to those of SrTiO<sub>3</sub> (222), which clearly shows that the  $\phi$  position of the pole of the (110) plane of the BaTiO<sub>3</sub> film and that of the pole of the (222) plane of the SrTiO<sub>3</sub> substrate have a difference angle  $\Delta\phi = 45^\circ$ . This clearly points to the cube-on-cube orientation. Peaks occur every  $90^\circ$ , demonstrating the good in-plane BaTiO<sub>3</sub> orientation.

The full-width at half maximum (FWHM) of the BaTiO<sub>3</sub> 110 reflection is  $\Delta\phi = 1.16^\circ$  which includes contributions from both 110 and 101 reflections and is thus a good value. (The FWHM of the 222 peak of the SrTiO<sub>3</sub> substrate is  $\Delta\phi = 0.16^\circ$ ). The epitaxial relationship of the BaTiO<sub>3</sub> films on the (001) SrTiO<sub>3</sub> substrates determined by XRD  $\phi$  scans clearly show that the locally (by TEM investigations) determined orientation relationship is valid for the entire film. Moreover, in rocking curves of the BaTiO<sub>3</sub> 200/002 peak, FWHM values are ranging from  $0.225^\circ$  to  $0.303^\circ$  confirming the good overall crystallinity of the BaTiO<sub>3</sub> films [see Fig. 4.34(a) below].

### 4.2.3 Later growth stages

No further drastic changes in the morphology of the epitaxial BaTiO<sub>3</sub> films were observed on increasing the film thickness. At a nominal film thickness of 75 nm some of the previous small grains start to grow in size and incorporate the surrounding grains. At this stage of growth, round large grains form the topography of the BaTiO<sub>3</sub> film [see Fig. 4.10(h)]. Their height varies from 10 to 15 nm, while their lateral size increases to about 100 nm (Fig. 4.23). The nominal thickness of 75 nm represents

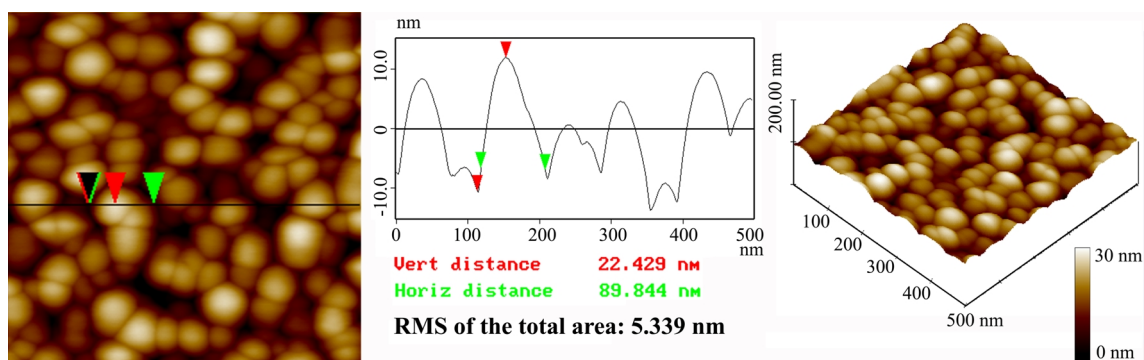


**Fig. 4.23:** Zoom-in topography image ( $0.5 \times 0.5 \mu\text{m}^2$  area and 30 nm in height) of the 75 nm thick BaTiO<sub>3</sub> film presented in Fig. 4.10(h).

the turning point when small grains coalesce together into large grains. This is an important feature not only for the study of the growth mechanism. Dielectric constant properties of epitaxial BaTiO<sub>3</sub> films will be correlated with this change in the morphology which was observed by AFM.

XRD analysis of BaTiO<sub>3</sub> films of higher nominal thickness as presented in Fig. 4.24 confirm the epitaxial film growth for thick films.

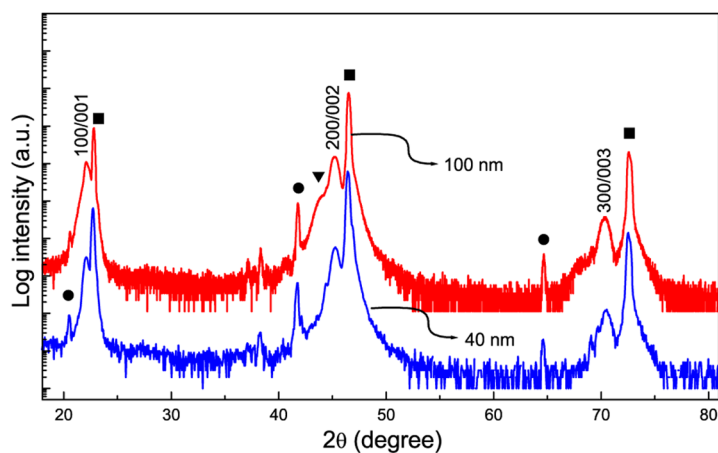


**Fig. 4.24:** XRD  $\theta$ - $2\theta$  scan of nominally 40 nm (blue curve) and 100 nm (red curve) thick BaTiO<sub>3</sub> films. The peaks labelled as  $m00/00m$  are the BaTiO<sub>3</sub> film peaks. Those labelled with squares are the SrTiO<sub>3</sub> substrate peaks, while those labelled with circles and triangle are the substrate peaks originating from the remaining Cu-K $\beta$  radiation and from the W-L $\alpha$  radiation, respectively. The latter comes from the tungsten contamination of the x-ray target. Logarithmic scale of diffraction intensity is used, which enables some very weak diffraction peaks to be displayed.

With the increase of the film thickness, the film is occupied with larger grains with round shapes as they coalesce and merge together. At 150 nm nominal thickness of the BaTiO<sub>3</sub> film, AFM topography images show grains with more different sizes than at the previous stages of film growth. The height of the grains has values up to 22.7 nm and their lateral size is about 150 nm [Fig. 4.10(j)]. In a detailed

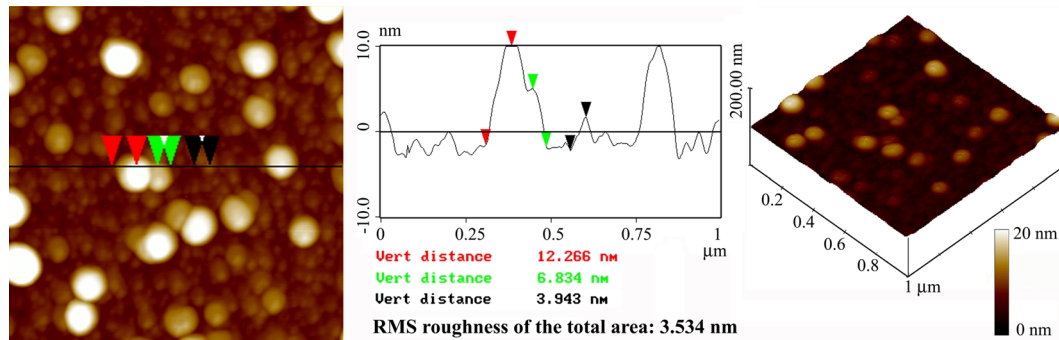


**Fig. 4.25:** Zoom-in topography image ( $1 \times 1 \mu\text{m}^2$  area and 20 nm in height) of the nominally 150 nm thick BaTiO<sub>3</sub> film presented in Fig. 4.10(j).

area of the film top surface, large grains can be observed (Fig. 4.25). Further on, a columnar structure develops (Fig. 4.26).

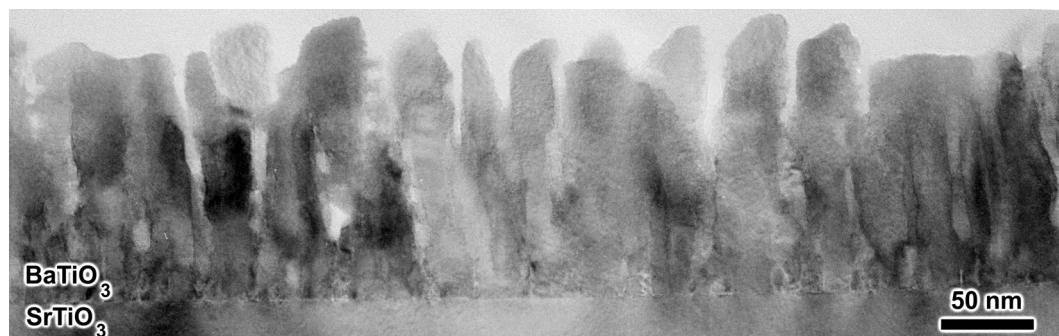


**Fig. 4.26:** Cross-sectional TEM image of an epitaxial BaTiO<sub>3</sub> thin film of 150 nm nominal thickness deposited on a vicinal SrTiO<sub>3</sub>:Nb substrate by PLD.

The process of coalescence which results in larger grains is well seen in Fig. 4.27, where it can be observed how the columnar structure begins with a small lateral size of the columns, and then proceeds towards larger lateral sizes with increasing film thickness.

When the film thickness further increases, the shapes and the lateral sizes of the grains become irregular, and the roughness of the epitaxial BaTiO<sub>3</sub> film increases. After 2.5 h deposition, the BaTiO<sub>3</sub> nominal thickness is about 320 nm and the RMS roughness is about 10.5 nm (Fig. 4.28).

However, with the increase of the film thickness, the average grain size is kept at about 100 nm. At this stage of growth, Fig. 4.29 shows an image demonstrating how several grains are connected and grow together as a large grain.

A study of the early growth stages of epitaxial PLD-grown Pb(Zr<sub>0.52</sub>Ti<sub>0.48</sub>)O<sub>3</sub> films on SrTiO<sub>3</sub> substrates by Goh *et al.*<sup>[145]</sup> revealed a three-dimensional island growth mode. The initial small



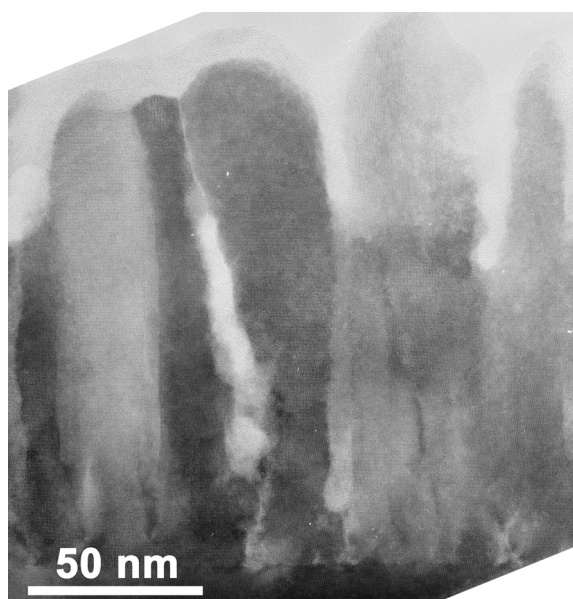


**Fig. 4.27:** Cross-sectional TEM image illustrating the coalescence process in a nominally 150 nm thick BaTiO<sub>3</sub> film.

nuclei of 25–30 nm in lateral size were found to merge into large grains of 100–120 nm size resulting in a two-layer structure of the film. Increasing the thickness of the Pb(Zr<sub>0.52</sub>Ti<sub>0.48</sub>)O<sub>3</sub> film from 50 nm to 115 nm, a columnar-like growth mode was found to dominate the film morphology.

Indeed, a columnar film structure is observed by cross-sectional TEM analysis in BaTiO<sub>3</sub> films, too. Fig. 4.30 shows a nominally 320 nm thick epitaxial BaTiO<sub>3</sub> film. A close inspection of the image shows that the film/substrate interface is sharp and that a columnar BaTiO<sub>3</sub> structure develops [Fig. 4.30(a)]. This is a typical column-like structure that is often observed in laser-ablated epitaxial thin films of complex oxides [e.g., Pb(Zr<sub>x</sub>Ti<sub>1-x</sub>)O<sub>3</sub><sup>[145]</sup> or YBa<sub>2</sub>Cu<sub>3</sub>O<sub>7-δ</sub><sup>[146]</sup>]. But also, in films with less complex composition (e.g., CeO<sub>2</sub><sup>[147]</sup>), the apparent grain size usually increases with the film thickness. It is expected that this trend of columnar-structure growth still dominates in thicker BaTiO<sub>3</sub> films, as long as the deposition conditions are not changed.

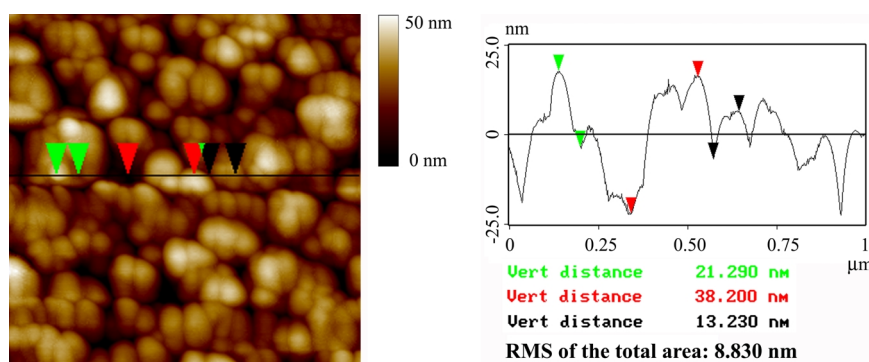


**Fig. 4.28:** Zoom-in topography image ( $1 \times 1 \mu\text{m}^2$  area and 50 nm in height) of the 320 nm thick BaTiO<sub>3</sub> film presented in Fig. 4.10(1).

A schematic model of the columnar growth is shown in Fig. 4.31 after ref.<sup>[145]</sup>. The “wetting” layer is not present in this case where Pb(Zr<sub>0.52</sub>Ti<sub>0.48</sub>)O<sub>3</sub> grows with an island mechanism, and also the lateral size of the columns showed higher values than the values found in the present study. The

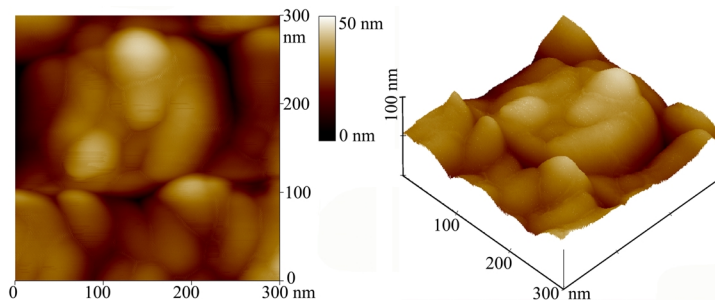


**Fig. 4.29:** Zoom-in topography image ( $0.3 \times 0.3 \mu\text{m}^2$  area and 50 nm in height) of the nominally 320 nm thick BaTiO<sub>3</sub> film presented in Fig. 4.10(l).

electron diffraction patterns taken from an area around the film/substrate interface reveals the following orientation relationship (see Fig. 4.30(b)):

$$(001)/(100) \text{ BaTiO}_3 \parallel (001) \text{ SrTiO}_3; [100]/[001] \text{ BaTiO}_3 \parallel [100] \text{ SrTiO}_3 \quad (4.3)$$

This relationship is in accordance with the XRD  $\theta$ - $2\theta$  scans measured for thick BaTiO<sub>3</sub> films and shown in Fig. 4.32.

The resolution of the TEM diffraction patterns makes it difficult to resolve the tetragonality of the BaTiO<sub>3</sub> lattice, i.e. to differentiate between, e.g., 400 and 004 BaTiO<sub>3</sub> reflections. In diffraction patterns taken from a sample region around the film/substrate interface [Fig. 4.30(b)], the reflections of BaTiO<sub>3</sub> and SrTiO<sub>3</sub> are well separated, indicating a well relaxed state of the BaTiO<sub>3</sub> lattice. The relative width of BaTiO<sub>3</sub> and SrTiO<sub>3</sub> reflections indicates a small out-of-plane orientational variation. A corresponding misorientation of  $2^\circ$  between two BaTiO<sub>3</sub> grains can be observed in Fig. 4.33.

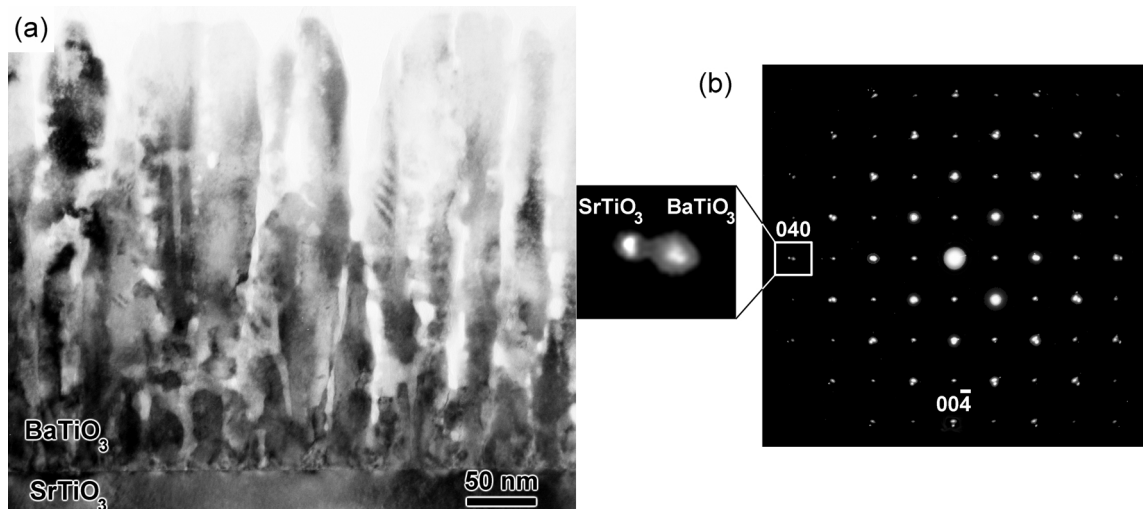


**Fig. 4.30:** (a) Cross-sectional TEM image of an epitaxial BaTiO<sub>3</sub> thin film of 320 nm thickness deposited on a vicinal SrTiO<sub>3</sub>:Nb substrate by PLD. (b) Diffraction pattern taken from the interface region between the BaTiO<sub>3</sub> film and the SrTiO<sub>3</sub> substrate.

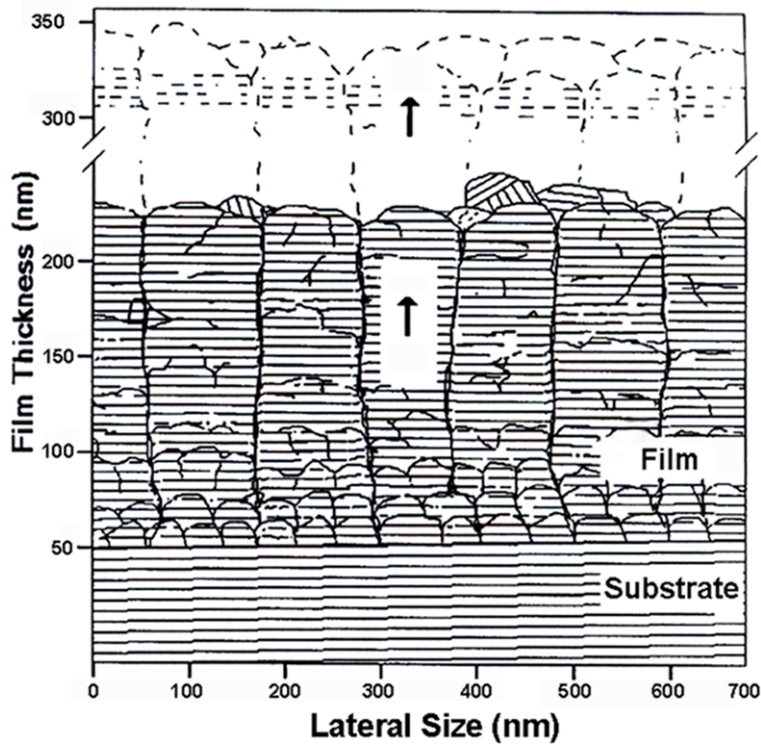


**Fig. 4.31:** Schematic model of columnar growth developed for  $Pb(Zr_{0.52}Ti_{0.48})O_3$  film grown on vicinal  $SrTiO_3$  substrate, according to ref.<sup>[145]</sup>.

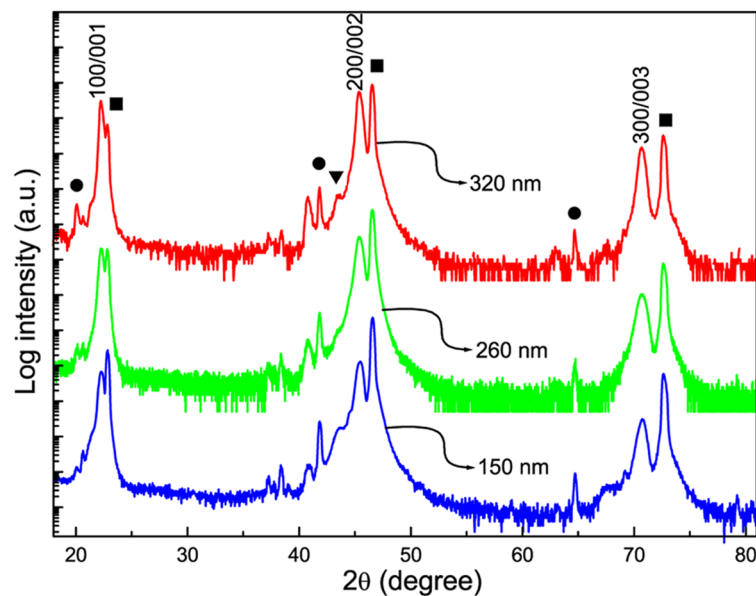


**Fig. 4.32:** XRD  $\theta$ - $2\theta$  scan of nominally 150 nm (blue curve), 260 nm (green curve), and 320 nm (red curve) thick  $BaTiO_3$  films. The peaks labelled as  $m00/00m$  are the  $BaTiO_3$  film peaks. Those labelled with squares are the  $SrTiO_3$  substrate peaks, while those labelled with circles and triangle are the substrate peaks originating from the remaining  $Cu-K_\beta$  radiation and from the  $W-L_\alpha$  radiation, respectively. The latter comes from the tungsten contamination of the x-ray target.



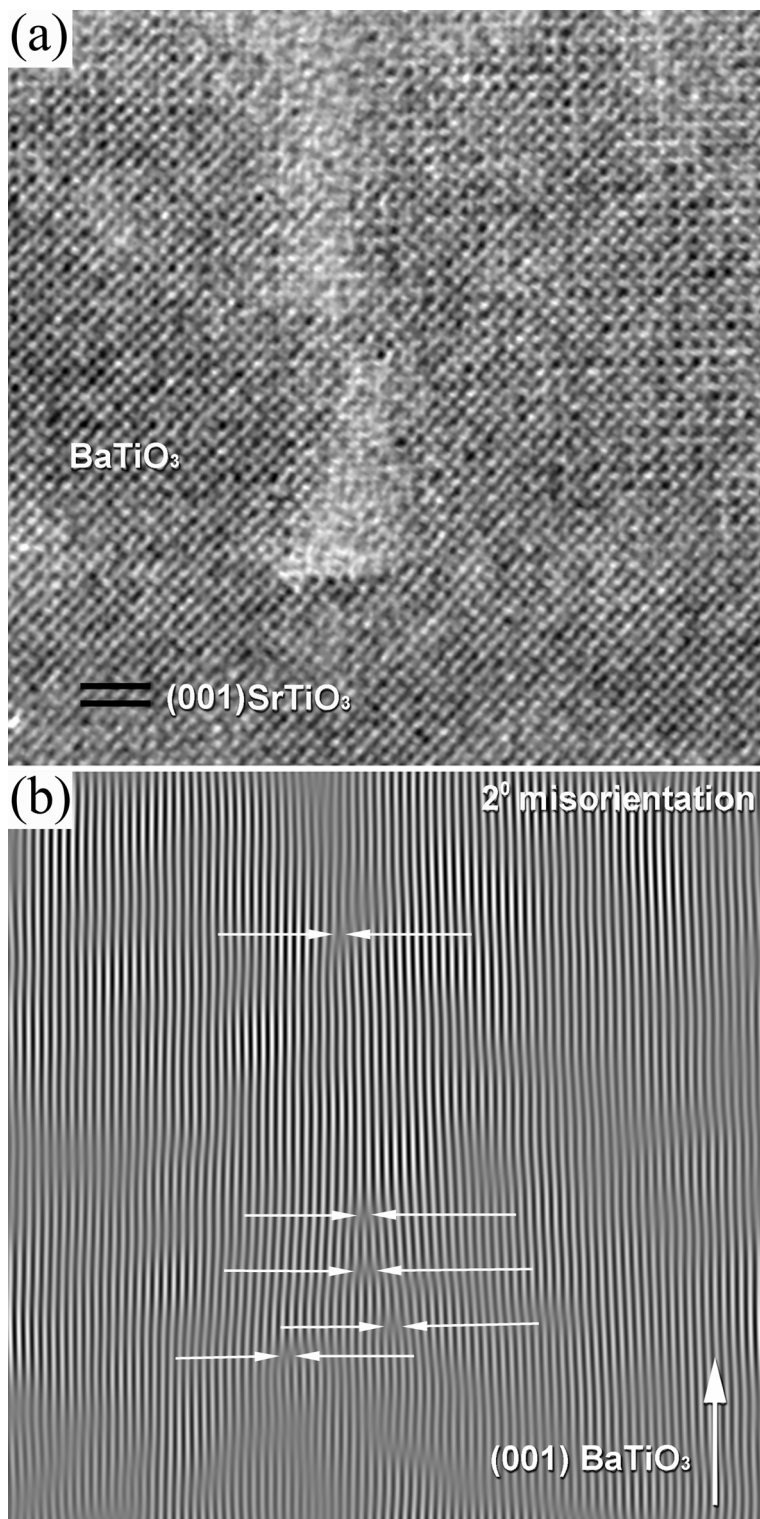


**Fig. 4.33:** (a) Cross-sectional HRTEM image of the interface between the epitaxial BaTiO<sub>3</sub> film and the SrTiO<sub>3</sub> substrate showing a 2° misalignment between two BaTiO<sub>3</sub> grains. The corresponding dislocations in the low-angle grain boundary are marked below by arrows. (b) Fourier-filtered image using (100)/(000) filter masks.

Increasing the deposition time even more does not show any further increase of island sizes. However, the surface roughness tends to increase further with increasing deposition time. The average in-plane size of the larger grains does not significantly increase above 100 nm on increasing film thickness, while the root mean square (RMS) roughness of the BaTiO<sub>3</sub> films increases from 0.17 nm to 4.6 nm as the nominal film thickness increases from 0.6 nm to 320 nm [Fig. 4.34(a)]. The average root-mean-square (RMS) roughness was obtained from several 2 x 2 μm<sup>2</sup> AFM images. Cross-sectional TEM investigations showed that, for the initial growth stages, the real film thicknesses corresponds well to the respective nominal film thickness values. The RMS roughness increases slowly up to the thickness of 40 nm of the BaTiO<sub>3</sub> film. Then it increases quickly up to 75 nm, followed by a relative saturation up to a nominal thickness of 320 nm. From 320 nm in thickness, the RMS roughness is again abruptly increasing.

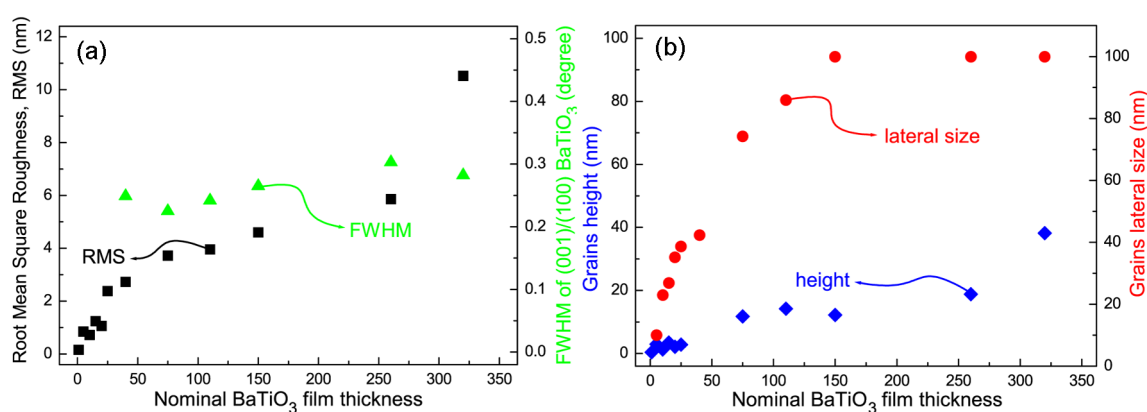


**Fig. 4.34:** (a) Dependence of the RMS roughness (black dots) of BaTiO<sub>3</sub> films and of the Full Width at Half Maximum (FWHM) (green dots) of the BaTiO<sub>3</sub> 200/002 peak measured in rocking curves ( $\omega$ -scan). (b) The height (blue dots) and lateral sizes (red dots) of BaTiO<sub>3</sub> film grains versus film thickness. BaTiO<sub>3</sub> films were grown on 0.1° vicinal SrTiO<sub>3</sub>:Nb substrates.

#### 4.2.4 Concluding remarks

The present work provides the first study of the *layer-then-island* (*Stranski-Krastanov*) growth mode of epitaxial BaTiO<sub>3</sub> films grown onto SrTiO<sub>3</sub> substrates. Among the diversity of deposition techniques, the PLD method was used to grow BaTiO<sub>3</sub> films. Following the results presented in detail in this section, the initial stages of the growth mechanism of epitaxial BaTiO<sub>3</sub> films on (001) SrTiO<sub>3</sub> substrates were studied by using a combination of investigation techniques. In order to analyze the surface morphology, the crystalline orientation, the microstructure and the film/substrate interface morphology a combined application of AFM, HRTEM, and XRD proved to be useful to highlight the BaTiO<sub>3</sub> growth mechanism.

It was shown that a surface reference before any deposition was required for a proper study of the initial growth stages, and to provide a well-defined surface for the epitaxial thin films further deposited. Therefore, an atomically flat surface of the (001)-oriented SrTiO<sub>3</sub> substrate with 0.1° miscut angle was prepared by a definite chemical and thermal treatment. The surfaces should not be only smooth, but also single terminated in order to enhance a unique growth sequence. The TiO<sub>2</sub>-terminated vicinal surface consists of well-defined regular terraces with the height of 0.4 nm, and the width ranging from 150 nm to 250 nm.

The results on the different growth stages observed on BaTiO<sub>3</sub> films varying the film thickness from 1 nm to 1 μm can be summarized as follows:

1. In the early growth stage, a *complete grainy layer* clearly seen by a cross-sectional HRTEM investigation uniformly covers the SrTiO<sub>3</sub> substrate surface at a BaTiO<sub>3</sub> nominal thickness of 1 nm. It was shown by AFM investigations that BaTiO<sub>3</sub> unit cells are added both to the terrace steps and on the terraces.
2. Further on, *small grains* were observed to grow onto the previous wetting layer at a nominal thickness of the BaTiO<sub>3</sub> film of 5 nm. Their height is about 3 nm, and their lateral size is about 5 nm. The RMS roughness of the film surface suddenly increased confirming the change in the film morphology. It was concluded that this nominal thickness represents the turning point, when individual grains begin to grow and film stress relaxes.
3. The density of the small grains was observed to increase by further deposition, covering the vicinal terraces. No further important changes in the film morphology was observed increasing the film thickness up to 75 nm.
4. In the later growth stages, the previous small grains were shown to become larger by coalescence of several neighbouring grains. At a nominal thickness of 75 nm, round grains of 10 to 15 nm in height and about 100 nm in lateral size form the film morphology. This is an important feature resulting in a *columnar* structure developing for thicker films. By further deposition, these large grains were observed to grow in height and in lateral size.

The epitaxy of BaTiO<sub>3</sub> films was proven by XRD  $\theta$ - $2\theta$ -scans, pole figures and  $\phi$  scans, and by the TEM diffraction pattern taken from the interface region between the BaTiO<sub>3</sub> film and the SrTiO<sub>3</sub> substrate. The following orientation relationship was revealed:

$$(001)/(100) \text{ BaTiO}_3 \parallel (001) \text{ SrTiO}_3; [100]/[001] \text{ BaTiO}_3 \parallel [100] \text{ SrTiO}_3$$

Despite of theoretical calculations of other authors which showed that the layer-by-layer mode is a possible growth mode in the BaTiO<sub>3</sub>/SrTiO<sub>3</sub> system, the present study gives evidence of the Stranski-Krastanov growth mode under specific deposition conditions, pointing to new evidences (e.g., roughness) which were not taken into account up to now.

## 4.3 Epitaxial BaTiO<sub>3</sub>/SrTiO<sub>3</sub> multilayers

### 4.3.1 Expected stresses in BaTiO<sub>3</sub>/SrTiO<sub>3</sub> multilayers

One has to consider that for a thin BaTiO<sub>3</sub> layer, stresses are expected to arise along both interfaces with the SrTiO<sub>3</sub> substrate and perpendicular to it<sup>[6]</sup> (Fig. 4.35). Therefore, tensile stress is expected

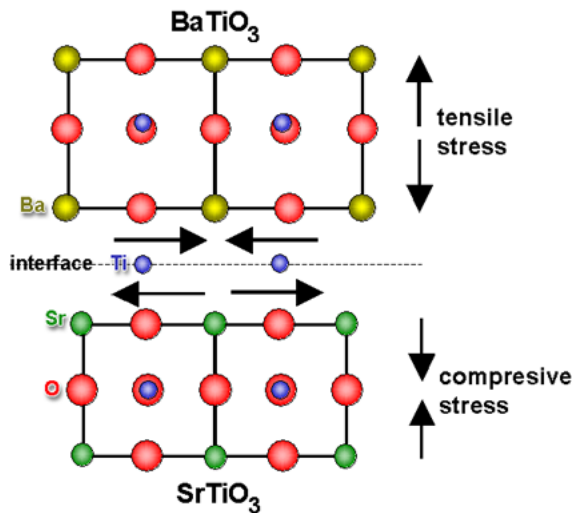


*Fig. 4.35: A schematic drawing of the stress which appears at the BaTiO<sub>3</sub> film / SrTiO<sub>3</sub> substrate interface, according to ref.<sup>[148]</sup>.*

to occur in the BaTiO<sub>3</sub> layer in the perpendicular direction to the interface, while compressive stress is expected to occur along the interface. The inverse situation is expected to occur in the SrTiO<sub>3</sub> layer of a BaTiO<sub>3</sub>/SrTiO<sub>3</sub> multilayer system. Compressive stress occurs in the SrTiO<sub>3</sub> layer in the perpendicular direction to the interface with a BaTiO<sub>3</sub> layer, while tensile stress is expected to occur along the interface (Fig. 4.35). A schematic diagram of the stresses in BaTiO<sub>3</sub>/SrTiO<sub>3</sub> multilayers is shown in Fig. 4.36.

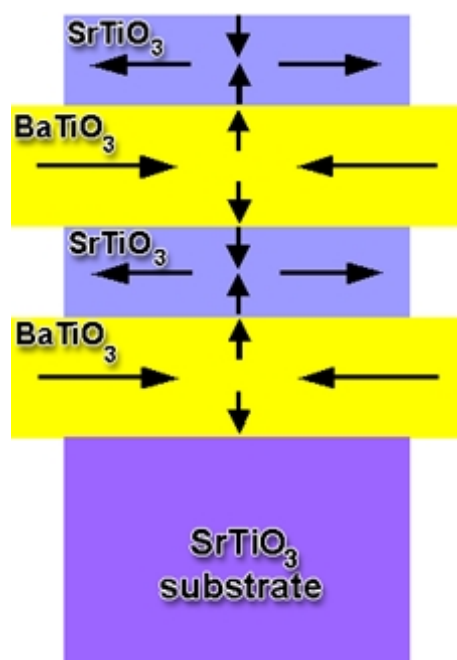


*Fig. 4.36: Diagram of the tensile and compressive stresses which are expected to occur at the BaTiO<sub>3</sub> film / SrTiO<sub>3</sub> substrate interface, as well as at the BaTiO<sub>3</sub> layer/SrTiO<sub>3</sub> layer interfaces, according to ref.<sup>[148]</sup>.*

The strain introduced into the BaTiO<sub>3</sub> layer by the in-plane mismatch between BaTiO<sub>3</sub> and SrTiO<sub>3</sub> is relaxed with increasing thickness of the BaTiO<sub>3</sub> layer<sup>[127]</sup>. A related dependence of the lattice parameter on film thickness in an epitaxial system with a small lattice mismatch such as BaTiO<sub>3</sub> on SrTiO<sub>3</sub> was indeed reported<sup>[148, 149, 73]</sup>. As it was mentioned before, the lattice mismatch between BaTiO<sub>3</sub> and SrTiO<sub>3</sub> is 2.28 % along the *a* direction, while along the *c* direction it is 3.4 %. An expansion of a BaTiO<sub>3</sub> layer of 100 nm in thickness along the *c* axis was observed<sup>[148]</sup>. This feature indicates that there is a pressure effect at the interface due to the lattice mismatch. Above a certain thickness of the individual layers, misfit dislocations are introduced<sup>[144]</sup>, so that the epitaxial stresses are relaxed. Stress-related modifications of the dielectric properties can therefore be expected only for layer thicknesses below this critical thickness. Wunderlich<sup>[144]</sup> theoretically estimated this critical thickness to four monolayers.

### 4.3.2 Growth, structure and morphology of BaTiO<sub>3</sub>/SrTiO<sub>3</sub> multilayers

Epitaxial BaTiO<sub>3</sub>/SrTiO<sub>3</sub> multilayers were deposited by PLD. The BaTiO<sub>3</sub> layers of these multilayers were deposited under the same deposition conditions as the epitaxial BaTiO<sub>3</sub> films discussed in the previous section of this chapter. The epitaxial SrTiO<sub>3</sub> layers were deposited at 700 °C in an oxygen pressure of 0.2 mbar using a laser energy of 600 mJ and a repetition rate of 1 Hz.

In this section, epitaxial BaTiO<sub>3</sub>/SrTiO<sub>3</sub> multilayers are discussed in terms of surface morphology, microstructure of individual layers, and structure of the interfaces between BaTiO<sub>3</sub> and SrTiO<sub>3</sub> layers.

Again chemically and thermally treated vicinal surfaces of SrTiO<sub>3</sub> (001) single crystal substrates were used to grow the multilayers [Fig. 4.37(a)]. The morphology of several epitaxial BaTiO<sub>3</sub>/SrTiO<sub>3</sub> multilayers with *overall thicknesses*<sup>8</sup> of 15, 25, 50, 75, and 125 nm deposited by PLD using different deposition times of 5, 10, 20, 25, and 30 min, respectively, is shown in Figs. 4.37(b)-(f).

The morphology of BaTiO<sub>3</sub>/SrTiO<sub>3</sub> multilayers shows the same features as for the epitaxial BaTiO<sub>3</sub> films studied in the previous section of this chapter. Taking into account the details of surface morphology one can assume that the same Stranski-Krastanov mode governs the growth of a BaTiO<sub>3</sub> layer on a previous SrTiO<sub>3</sub> layer in a BaTiO<sub>3</sub>/SrTiO<sub>3</sub> multilayer system, as well as on the SrTiO<sub>3</sub> substrate as follows:

- film atoms initially form one or several complete monolayers on the substrate surface [Fig. 4.37(b)];
- subsequently 3D clusters are nucleating on these layers due to the stress induced by the lattice mismatch [Fig. 4.37(c)];
- grains become larger due to coalescence of several small grains which grow together by further deposition [Figs. 4.37(d) and 4.37(e)];

<sup>8</sup>The *overall thickness* of a BaTiO<sub>3</sub>/SrTiO<sub>3</sub> multilayer is defined as the sum of the nominal individual thicknesses of all the layers involved.

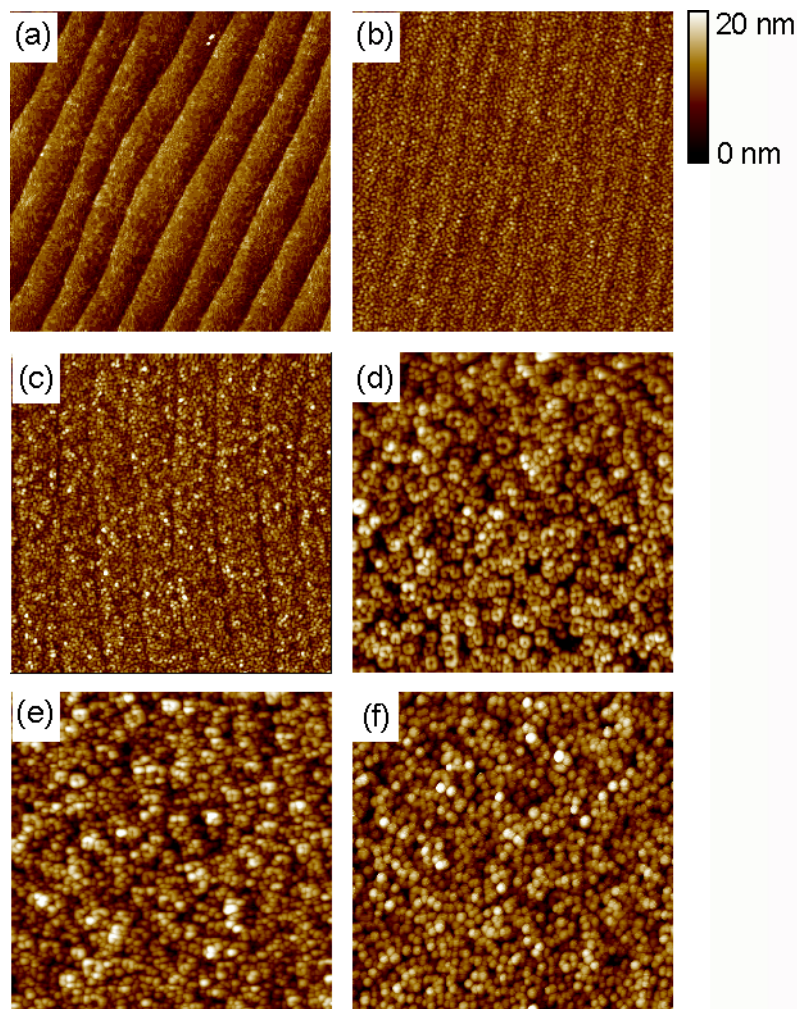


**Fig. 4.37:** AFM topography images ( $2 \times 2 \mu\text{m}^2$  area) of (a) a SrTiO<sub>3</sub>:Nb substrate with  $0.1^\circ$  miscut prepared by chemical and thermal treatment, and (b)–(f) BaTiO<sub>3</sub>/SrTiO<sub>3</sub>/BaTiO<sub>3</sub> multilayers grown on substrates of this type. Different deposition times of 5, 10, 20, 25, and 30 min were used to grow the multilayers of nominal overall thicknesses of (b) 15, (c) 25, (d) 50, (e) 75, and (f) 125 nm, respectively. The same deposition time has been used to grow each layer of BaTiO<sub>3</sub> or SrTiO<sub>3</sub>.

- a columnar structure develops for thicker films [Fig. 4.37(f)].

Structure and morphology of the grown multilayers were studied by cross-sectional HRTEM. Figure 4.38 shows three different cross-sectional images of the epitaxial BaTiO<sub>3</sub> film, BaTiO<sub>3</sub>/SrTiO<sub>3</sub>/BaTiO<sub>3</sub> and BaTiO<sub>3</sub>/SrTiO<sub>3</sub>/BaTiO<sub>3</sub>/SrTiO<sub>3</sub>/BaTiO<sub>3</sub> multilayers having the same overall thickness as the BaTiO<sub>3</sub> film. The interface between the first BaTiO<sub>3</sub> layer and the SrTiO<sub>3</sub> substrate is well-defined and sharp [Fig. 4.38(a)].

Fig. 4.38(b) shows the beginning of BaTiO<sub>3</sub> island formation (arrows) on a uniform, continuous BaTiO<sub>3</sub> layer of about 3 to 4 nm in thickness on top of a 5 nm thick SrTiO<sub>3</sub> layer. This observation is an indication for a Stranski-Krastanov growth mechanism followed by the BaTiO<sub>3</sub> layers growing on the deposited SrTiO<sub>3</sub> layers.

In the diffraction pattern of a multilayer with 5 nm thickness of the individual layers taken from a sample region around the film/substrate interface, the reflections of BaTiO<sub>3</sub> and SrTiO<sub>3</sub> are well separated, indicating a well relaxed state of the BaTiO<sub>3</sub> lattice (Fig. 4.39). This corresponds well to the formation of individual islands seen in Fig. 4.38(b). The same orientation relationship between BaTiO<sub>3</sub> layers and SrTiO<sub>3</sub> layers was revealed by the diffraction pattern taken from the BaTiO<sub>3</sub>/SrTiO<sub>3</sub> interface, as well as from the BaTiO<sub>3</sub> layer/SrTiO<sub>3</sub> substrate interface (see eq. 4.3).



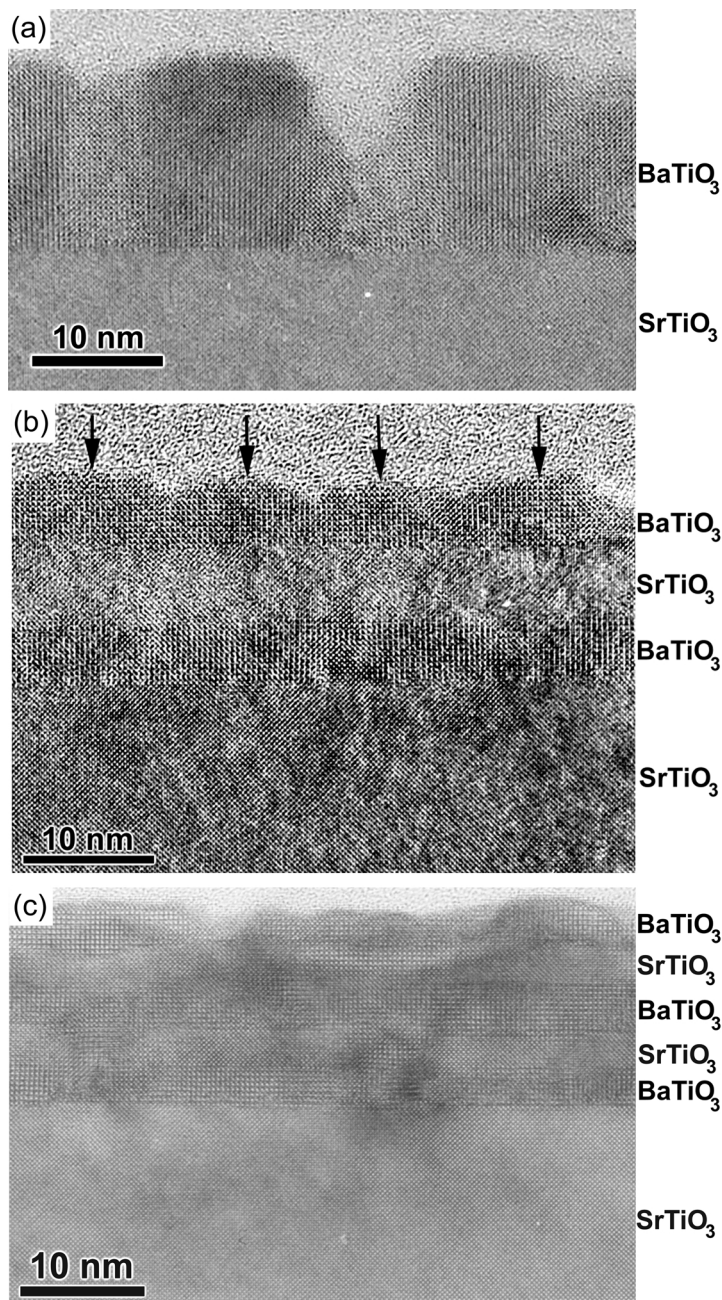


**Fig. 4.38:** Cross-sectional HRTEM view of multilayers of 15 nm overall thickness. (a) epitaxial BaTiO<sub>3</sub> film, (b) epitaxial BaTiO<sub>3</sub>/SrTiO<sub>3</sub>/BaTiO<sub>3</sub> multilayer (5 nm nominal thickness of each layer), (c) epitaxial BaTiO<sub>3</sub>/SrTiO<sub>3</sub>/BaTiO<sub>3</sub>/SrTiO<sub>3</sub>/BaTiO<sub>3</sub> multilayer (3 nm nominal thickness of each layer).

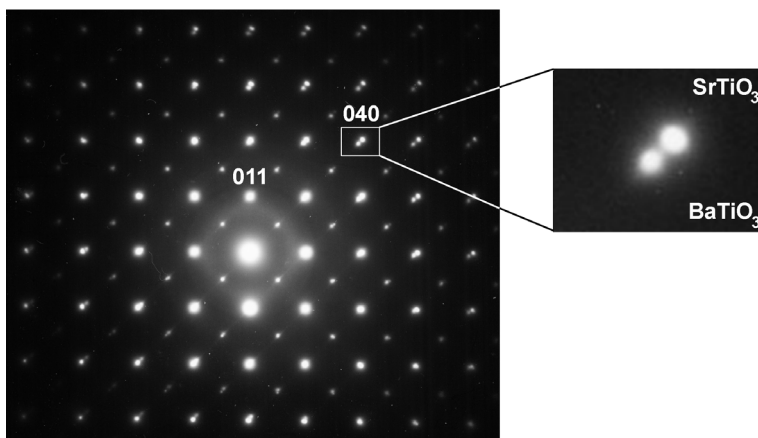


**Fig. 4.39:** Cross-sectional diffraction pattern taken from the sample area shown in Fig. 4.38(b).



The XRD analysis of BaTiO<sub>3</sub>/SrTiO<sub>3</sub> multilayers did not show any significant differences with respect to the BaTiO<sub>3</sub> films. The only difference was an increase of the intensity of the SrTiO<sub>3</sub> peaks due to the contribution of the SrTiO<sub>3</sub> layers (Fig. 4.40).

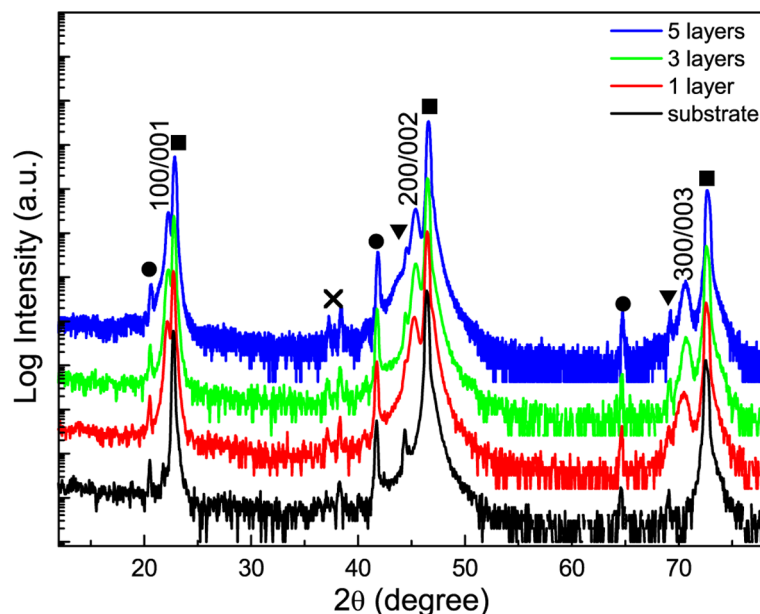


**Fig. 4.40:** XRD  $\theta$ – $2\theta$  scan of SrTiO<sub>3</sub> (001)-oriented substrate, of a nominally 40 nm thick BaTiO<sub>3</sub> layer, and of two multilayers of 40 nm thickness consisting of 3 and 5 individual layers, respectively. The peaks labeled as  $m00/00m$  are the BaTiO<sub>3</sub> film peaks. Those labeled with squares are the SrTiO<sub>3</sub> substrate peaks, while those labeled with circles and triangle are the substrate peaks originating from the remaining Cu- $K_{\beta}$  radiation and from the W- $L_{\alpha}$  radiation, respectively. The latter stems from the tungsten contamination of the x-ray target. The couple of peaks labeled as X are present also in the substrate pattern, so one can conclude that they are not from the BaTiO<sub>3</sub> film. Their origin is unclear.

Most interesting, the morphology of the BaTiO<sub>3</sub>–on–SrTiO<sub>3</sub> interfaces is different from that of the SrTiO<sub>3</sub>–on–BaTiO<sub>3</sub> interfaces. While the former interfaces are plane and sharp, the latter are rather rough, displaying a certain periodicity of the morphology (“waviness”). A similar asymmetry has recently been described by Dubourdieu *et al.*<sup>[2]</sup> showing that Ba penetrates far into the neighbouring SrTiO<sub>3</sub> layer, while Sr does not enter the neighbouring BaTiO<sub>3</sub> layer. The feature observed in Fig. 4.41 can most probably be explained by a different growth mechanism of the two materials, or by a difference in the morphological stability of the growth surfaces caused by different surface energies of BaTiO<sub>3</sub> and SrTiO<sub>3</sub> and by different mobilities of the Ba and Sr atoms reaching the SrTiO<sub>3</sub> and BaTiO<sub>3</sub> layer, respectively. As had been shown first by Mullins and Sekerka<sup>[150]</sup> for the case of crystal growth from a liquid phase, the morphological stability of a crystal surface during the growth of the crystal is determined by the relation between the interface energy (interface stress) and the lateral diffusivity of the condensing crystal species. A high interface energy acts in favour of a small interface area, i.e. in favour of a plane interface, while a low interface energy permits a wavy interface morphology to occur. On the other hand, a high lateral diffusivity of the arriving species contributes to a smoothening of the interface, while short diffusion paths prevent the smoothening of the inter-

face. Similar approaches were later applied to other cases, for example to a solid-solid interface by Martin<sup>[151]</sup>. In addition to the expected reduction of strain with increasing thickness of the individual

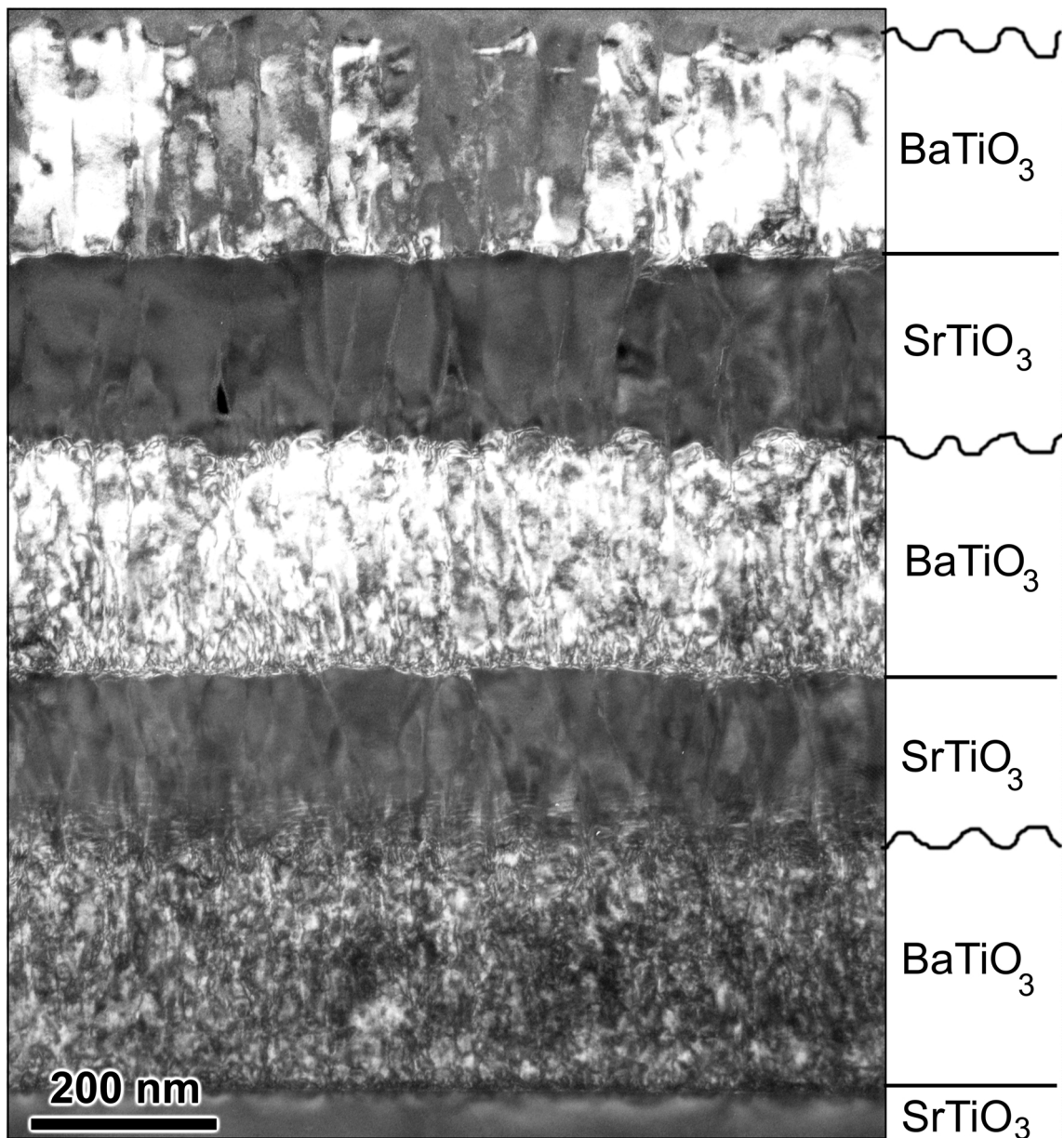


**Fig. 4.41:** Cross-sectional TEM image of an epitaxial BaTiO<sub>3</sub>/SrTiO<sub>3</sub> multilayer grown on a SrTiO<sub>3</sub> (001) substrate. The thickness of the individual BaTiO<sub>3</sub> layers is about 260 nm, and that of the individual SrTiO<sub>3</sub> layers is about 210 nm.

BaTiO<sub>3</sub> layers, the development of a columnar structure in thick layers has to be taken into account. Fig. 4.41 shows this columnar structure in the individual layers of a thick multilayer consisting of 260 nm thick BaTiO<sub>3</sub> layers and about 210 nm thick SrTiO<sub>3</sub> layers.

If the surface energies of BaTiO<sub>3</sub> and SrTiO<sub>3</sub> are largely different, and the diffusivity of the species arriving from the "BaTiO<sub>3</sub>" and "SrTiO<sub>3</sub>" plasma plumes are also largely different, the morphological stability of the growing BaTiO<sub>3</sub> surface may be quite different from that of the growing SrTiO<sub>3</sub>

surface. This effect could contribute to the difference in morphology observed between the BaTiO<sub>3</sub>-on-SrTiO<sub>3</sub> and SrTiO<sub>3</sub>-on-BaTiO<sub>3</sub> interfaces of thick multilayers shown, e.g., in Fig. 4.41.

To establish, whether this effect also occurs in very thin films, two experiments have been performed. In the first, a BaTiO<sub>3</sub>/SrTiO<sub>3</sub>/BaTiO<sub>3</sub> three-layer system was deposited onto SrTiO<sub>3</sub> (001), with an individual layer thickness of 15 nm. Second, a multilayer with increasing BaTiO<sub>3</sub> layer thickness from 1 to 16 nm thickness [2 to 40 monolayers (ML)] was deposited, while the thickness of the individual SrTiO<sub>3</sub> layer has been kept constant at 15 nm. A close look into Fig. 4.42 (first experiment)

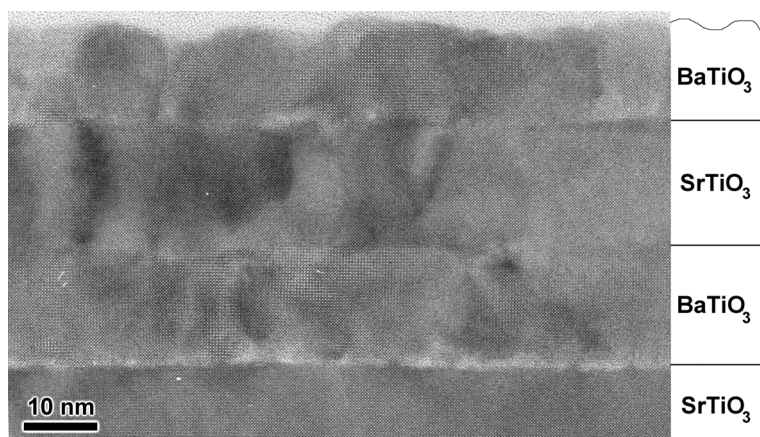


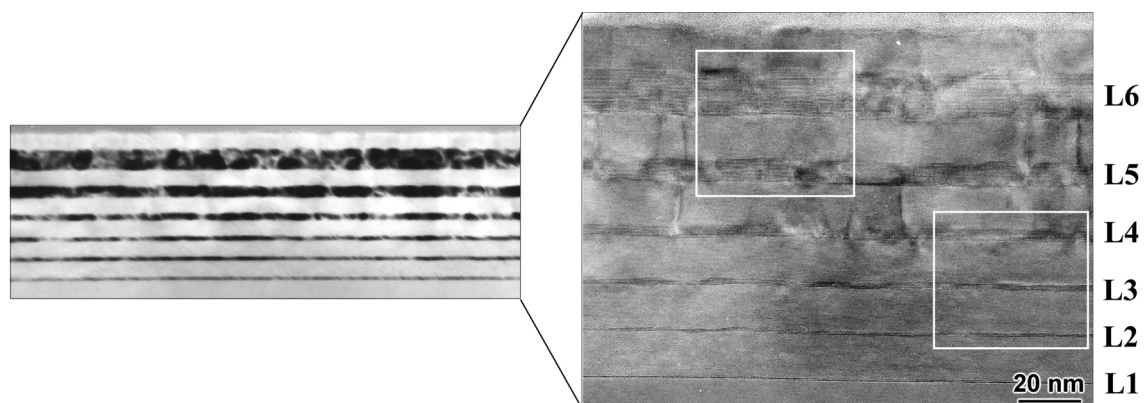
**Fig. 4.42:** Cross-sectional HRTEM image of epitaxial BaTiO<sub>3</sub>/SrTiO<sub>3</sub>/BaTiO<sub>3</sub> multilayer showing different interfaces between different layers. The overall thickness is about 45 nm (each layer is about 15 nm in thickness).

shows that the top surface of the first BaTiO<sub>3</sub> layer is a flat and sharp interface with the SrTiO<sub>3</sub> layer on top of it, while the top surface of the second BaTiO<sub>3</sub> layer is rough, most probably due to the relaxation process forming grains which start to nucleate on top of the complete layer, explained before as an indication of a Stranski-Krastanov growth mechanism. This feature can be explained in terms of relaxation of the second BaTiO<sub>3</sub> layer, while the first BaTiO<sub>3</sub> layer is under stress, suppressed in between the SrTiO<sub>3</sub> substrate and the SrTiO<sub>3</sub> layer. Alternatively, the rough surface in Fig. 4.42 may be an effect of the morphological stability as described before.

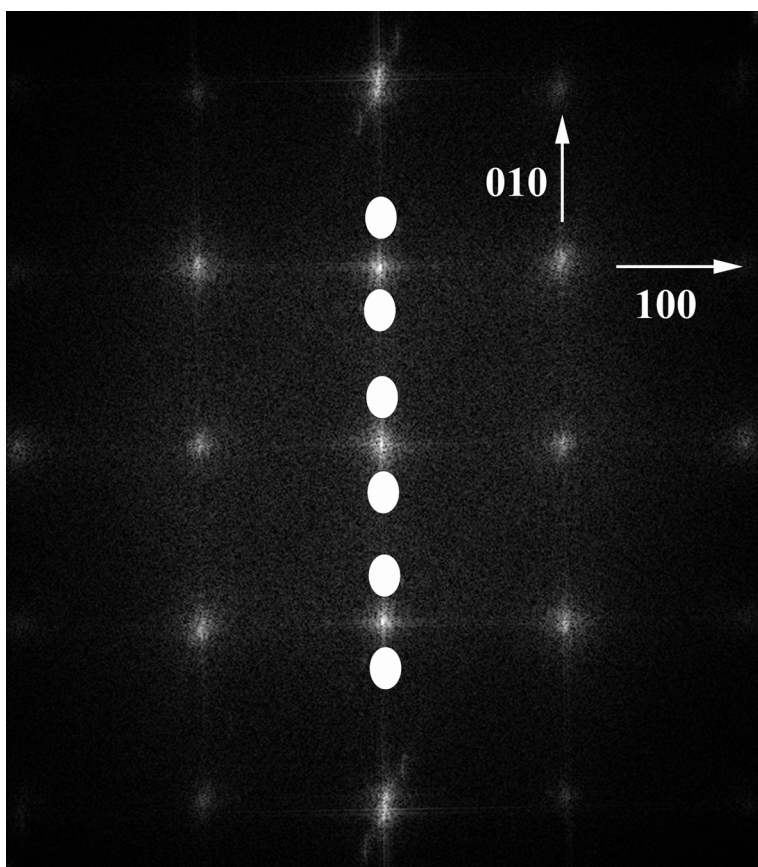
An important feature of the BaTiO<sub>3</sub>/SrTiO<sub>3</sub> multilayers is it that up to 6 nm in thickness, the BaTiO<sub>3</sub> layers show no defects and have sharp BaTiO<sub>3</sub>/SrTiO<sub>3</sub> interfaces. This feature is significant in view of actual efforts to grow epitaxial superlattices involving very thin individual layers of BaTiO<sub>3</sub> and/or SrTiO<sub>3</sub>. Moreover, it has been observed that the epitaxial SrTiO<sub>3</sub> film inserted in between two BaTiO<sub>3</sub> layers promotes a good crystallinity of the second BaTiO<sub>3</sub> layer.

Figure 4.43 (second experiment) shows a cross-section TEM image and a more detailed HRTEM image of a BaTiO<sub>3</sub>/SrTiO<sub>3</sub> multilayer with increasing thickness of the BaTiO<sub>3</sub> layers in between SrTiO<sub>3</sub> layers of constant thickness. Multilayers of this type should reveal effects related to the relaxation of strain with increasing BaTiO<sub>3</sub> layer thickness as it was mentioned before.

In order to check whether there is a change in the interface flatness also for the sample of Fig. 4.43, a fast Fourier transformation (FFT) (see Fig. 4.44) was performed on a selected section of the cross-sectional image presented in Fig. 4.43. The filtered, reconstructed pictures are presented in Fig. 4.45 showing the different degree of flatness of the different interfaces between BaTiO<sub>3</sub>/SrTiO<sub>3</sub> layers depending on the BaTiO<sub>3</sub> film thickness.



**Fig. 4.43:** Cross-sectional TEM view (left) and HRTEM view (right) of epitaxial  $\text{BaTiO}_3/\text{SrTiO}_3$  multilayers with different thickness of the individual  $\text{BaTiO}_3$  layers of 2 ML (L1), 4 ML (L2), 8 ML (L3), 12 ML (L4), 20 ML (L5), and 40 ML (ML–monolayer) (L6).



**Fig. 4.44:** Filter masks (ovals) applied to the Fourier pattern taken from one of the sample areas marked with squares in Fig. 4.43.

In Figs. 4.45 (a) and (c), filter masks were used around the reflections  $\pm (100)$ ,  $\pm (010)$ , and  $(000)$  in order to suppress the noises. The two different lattices (BaTiO<sub>3</sub> and SrTiO<sub>3</sub>) are clearly discernable in these two images, while the morphology of the interfaces is not easily derivable from these two images. To highlight the interfaces, in Figs. 4.45 (b) and (d), filter masks have been put solely on the vertical streaks occurring near the  $\pm (010)$  reflections (Fig. 4.44). Such streaks originate from interfaces perpendicular to the streak direction. As it can be seen in Figs. 4.45 (b) and (d), the morphology of the interfaces is more clearly visible in these two images than in the subfigures (a) and (c). The BaTiO<sub>3</sub> layers L2 to L4 (4 ML to 12 ML individual layer thickness) have plane top and bottom interfaces. Starting from the BaTiO<sub>3</sub> layer L5 (20 ML, i.e. about 8 nm thickness), the upper interface is clearly rough, while the lower interface keeps to be smooth. The transition from a smooth SrTiO<sub>3</sub>-on-BaTiO<sub>3</sub> interface to a rough one thus occurs at about 6 to 8 nm thickness of the BaTiO<sub>3</sub> layer. In view of the fact that the transition from the layer growth to the island growth of BaTiO<sub>3</sub> under our conditions had been found to occur at about 1 to 2 nm nominal BaTiO<sub>3</sub> thickness, the value of 6 to 8 nm found in Fig. 4.45 rather points to the morphological stability argument as an explanation for the difference in morphology between the SrTiO<sub>3</sub>-on-BaTiO<sub>3</sub> and the BaTiO<sub>3</sub>-on-SrTiO<sub>3</sub> interfaces. The fact that the morphological instability (the rough SrTiO<sub>3</sub>-on-BaTiO<sub>3</sub> interface) is not occurring below a thickness of about 6 to 8 nm could most probably be explained by the influence of the stress exerted by the upper and lower thick SrTiO<sub>3</sub> layers on the rather thin BaTiO<sub>3</sub> layer. This influence of the stress will decrease with increasing BaTiO<sub>3</sub> layer thickness.

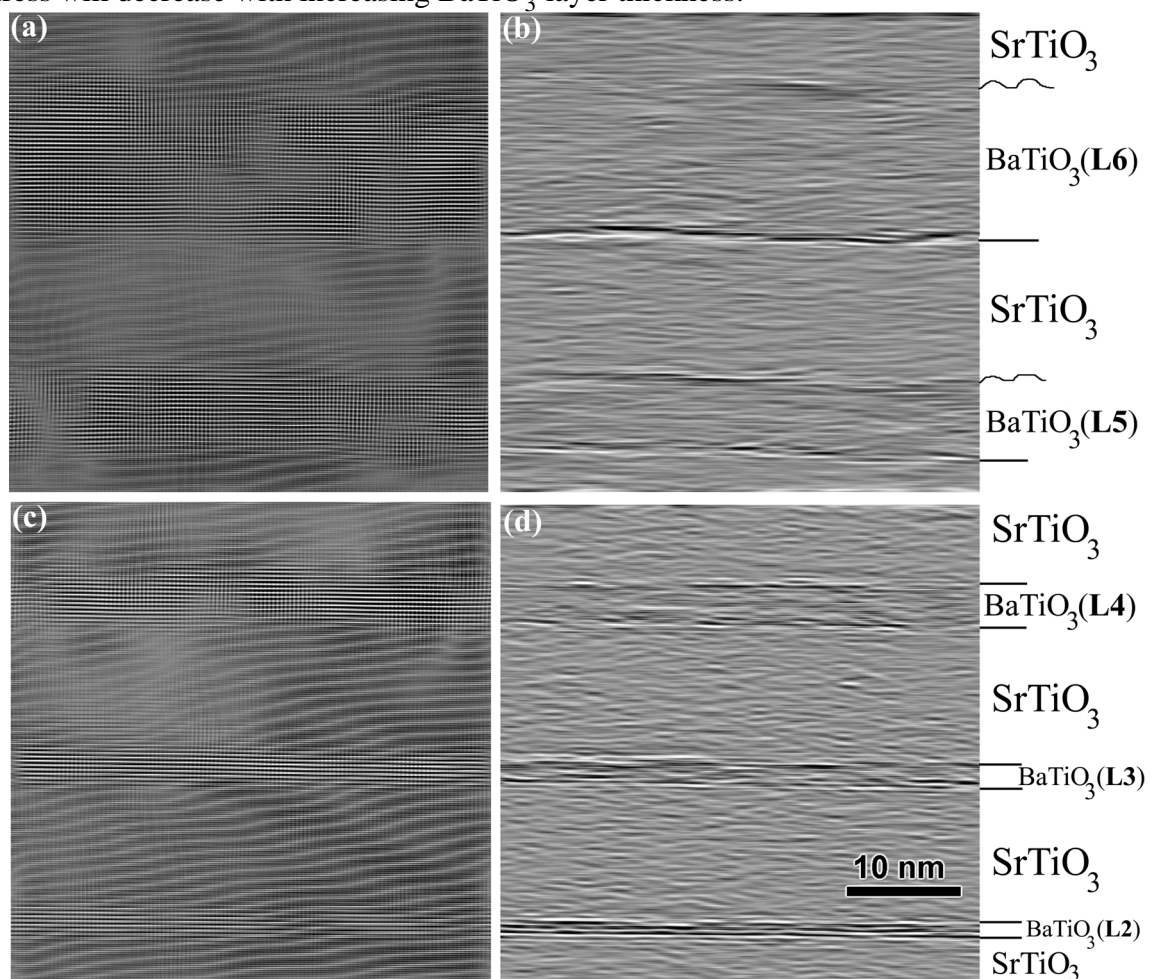


**Fig. 4.45:** Fourier filtered reconstructed images of the cross-sectional image presented in Fig. 4.43 showing the different degree of flatness of the different interfaces between BaTiO<sub>3</sub>/SrTiO<sub>3</sub> layers (BaTiO<sub>3</sub> layers have different thicknesses and are marked as L2, L3, L4, L5, and L6).

### 4.3.3 Concluding remarks

- The present study is relevant to actual efforts to grow smooth and defect free multilayers and superlattices of perovskite layers. The Stranski-Krastanov growth mechanism was found to govern not only the growth of individual BaTiO<sub>3</sub> films, as it was shown in the previous section of this chapter, but also the growth of the BaTiO<sub>3</sub> layers in a BaTiO<sub>3</sub>/SrTiO<sub>3</sub> multilayer system.
- The most significant feature is that of the asymmetry in the morphology of the SrTiO<sub>3</sub>-on-BaTiO<sub>3</sub> interface (rough interface) and of the BaTiO<sub>3</sub>-on-SrTiO<sub>3</sub> interface (sharp interface). This asymmetry was explained taking into account the difference in the morphological stability of the growth surfaces most probably caused by different surface energies of BaTiO<sub>3</sub> and SrTiO<sub>3</sub> and by different mobilities of the Ba and Sr atoms reaching the SrTiO<sub>3</sub> layer and the BaTiO<sub>3</sub> layer, respectively.
- Another important feature of the BaTiO<sub>3</sub>/SrTiO<sub>3</sub> multilayer system is that BaTiO<sub>3</sub> layers were free of defects and the SrTiO<sub>3</sub>-on-BaTiO<sub>3</sub> interfaces were plane and sharp when the BaTiO<sub>3</sub> thickness was below 6 nm. As a consequence, BaTiO<sub>3</sub> layers with a thickness below 6 nm can be assumed as growing layer-by-layer in a BaTiO<sub>3</sub>/SrTiO<sub>3</sub> multilayer system. This result may be of importance for future applications of BaTiO<sub>3</sub>/SrTiO<sub>3</sub> multilayers or superlattices.

## 4.4 Dielectric properties

Dielectric measurements were performed on Pt/BaTiO<sub>3</sub>/SrTiO<sub>3</sub>:Nb and Pt/BaTiO<sub>3</sub>/.../SrTiO<sub>3</sub>/BaTiO<sub>3</sub>/SrTiO<sub>3</sub>:Nb heterostructures with different thickness of the individual BaTiO<sub>3</sub> and SrTiO<sub>3</sub> layers.

### 4.4.1 BaTiO<sub>3</sub> films

A dependence of the dielectric constant,  $\epsilon$ , and the dielectric loss tangent,  $\tan \delta$ , on the BaTiO<sub>3</sub> film thickness is shown in Fig. 4.46. Both  $\epsilon$  and  $\tan \delta$  show an approximately linear dependence on the BaTiO<sub>3</sub> film thickness, however with two different rates of increase above and below a thickness of 75 nm, respectively. Below 75 nm,  $\epsilon$  and  $\tan \delta$  linearly decrease with decreasing film thickness

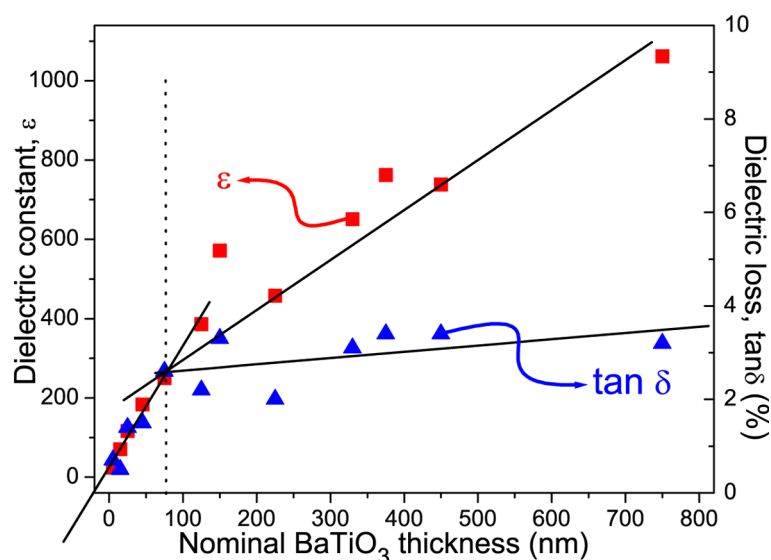


**Fig. 4.46:** Thickness dependence of the dielectric constant and the dielectric loss tangent measured on Pt/BaTiO<sub>3</sub>/SrTiO<sub>3</sub>:Nb heterostructures for different thickness of the BaTiO<sub>3</sub> film. The lines are only to guide the eye.

on a clearly higher rate than above 75 nm. One reason of the reduction in dielectric constant with decreasing film thickness in the case of films may be a decreasing overall quality of the dielectric throughout the film, caused by factors such as increasing stress or increasing number of defects with decreasing film thickness, particularly such defects to which the ferroelectric properties are sensitive. However, in the present study no indication of a deteriorating structure of the films was observed by TEM with decreasing film thickness. Moreover, in case of thick films, the value of the dielectric constant is close to the bulk value, which confirms the good crystallinity of the films: A maximum value of 1000 for the dielectric constant was, e.g., measured on thick BaTiO<sub>3</sub> film by Hayashi *et al.*[152]. For this reason, a different origin should be responsible for the decrease of  $\epsilon$  with film thickness. It is interesting to note that the dielectric loss almost saturates for thicknesses above 300 nm, but abruptly decreases below a thickness of 75 nm. This thickness represents the turning point at which also the dielectric constant changes its thickness dependence. Consequently, this points to a



common origin of both effects. A close look to the AFM and TEM results shows that at this thickness the morphology of BaTiO<sub>3</sub> films changes from small grains to large grains formed by coalescence of several small neighbouring grains, as it was shown previously in this work. A corresponding change of properties is present, actually, in all thickness dependencies, including RMS roughness, grain dimensions (height and lateral size), and also the dielectric constant. Thus it is most likely that the turnover point at 75 nm seen in Fig. 4.46 is caused by the sudden change of the morphology of the grains.

The decrease in dielectric constant with film thickness was recently modeled by assuming the existence of so-called “dead layers” at the electrode-ferroelectric interfaces having a severely depressed dielectric constant. These interfacial dead layers act as parasitic capacitors in series<sup>[153]</sup> or in parallel<sup>[154]</sup> with the bulk-like ferroelectric. Various models have been proposed, viz. low-dielectric-constant space-charge-layers<sup>[155]</sup>, oxygen-depletion zones adjacent to metals with a high-oxygen affinity<sup>[156]</sup>, formation of surface states<sup>[156]</sup>, local diffusion of electrode material into the ferroelectric<sup>[157, 158]</sup>, lattice-mismatch-induced ion vacancy formation<sup>[159]</sup>, chemically distinct surface phase<sup>[160]</sup>, intrinsic surface polarization effects<sup>[161, 162]</sup>, depolarization fields due to incomplete screening by the electrodes<sup>[163, 164]</sup>, intrinsic suppression of polarization at the electrode<sup>[165]</sup>, a formation of a Schottky barrier and an associated depletion layer as a result of band bending at the ferroelectric-electrode interface<sup>[166]</sup>.

In order to explain the thickness dependence of the dielectric constant, two approaches are considered in the present study. First, a series capacitor model<sup>[153]</sup> was taken into account considering both the bulk of the ferroelectric and the ferroelectric-electrode interfaces. In this model, the effective capacitance of the dielectric layer is given by the following relation:

$$\frac{1}{C_{eff}} = \frac{1}{C_b} + \frac{1}{C_{Pt}} + \frac{1}{C_{SrTiO_3:Nb}} \quad (4.4)$$

where the *eff* subscript represents the effective value experimentally measured, *b* means the bulk value, *Pt* refers to the Pt/BaTiO<sub>3</sub> top interface, and *SrTiO<sub>3</sub>:Nb* to the SrTiO<sub>3</sub>:Nb/BaTiO<sub>3</sub> bottom interface.

To simplify the calculations the two metal-dielectric interfaces are considered as being identical. Since we are not able to calculate the contribution of the SrTiO<sub>3</sub>:Nb/BaTiO<sub>3</sub> interface this contribution to the effective value of the capacitance is assumed to be equal to the contribution of the Pt electrode – BaTiO<sub>3</sub> interface<sup>[167]</sup>. Thus:

$$\frac{1}{C_{eff}} = \frac{1}{C_b} + \frac{2}{C_i} \quad (4.5)$$



where  $C_i$  is the interface capacitance. Considering the thickness of the interfacial dead layer being independent of the total film thickness results in:

$$\frac{d}{\epsilon_{eff}} = \frac{d_b}{\epsilon_b} + 2\frac{d_i}{\epsilon_i} \quad (4.6)$$

where  $d$  is the nominal thickness of the film,  $d_b$  is the bulk thickness, and  $d_i$  is the thickness of the film-electrode interface. Considering the total thickness  $d$  being equal to

$$d = d_b + 2d_i \quad \implies \quad d_b = d - 2d_i \quad (4.7)$$

equation 4.6 becomes:

$$\frac{d}{\epsilon_{eff}} = \frac{d}{\epsilon_b} + 2d_i\left(\frac{1}{\epsilon_i} - \frac{1}{\epsilon_b}\right) \quad (4.8)$$

It is usually assumed that either  $\epsilon_b \gg \epsilon_i$  or  $d_b \gg d_i$ [153].

Taking into account the first case, we can write:

$$\frac{d}{\epsilon_{eff}} = \frac{d}{\epsilon_b} + 2d_i\frac{1}{\epsilon_i} \quad (4.9)$$

Using the experimental data for the dielectric constant of Fig. 4.46 and recalculating them into  $d/\epsilon$  values for the two different thickness regions (below and above 75 nm) results in Fig. 4.47, where the red curves represent the linear fits to the experimental values. Two different slopes are obtained for different thicknesses of the BaTiO<sub>3</sub> film in the Pt/BaTiO<sub>3</sub>/SrTiO<sub>3</sub>:Nb heterostructures. The  $(d_i/\epsilon_i)$  and

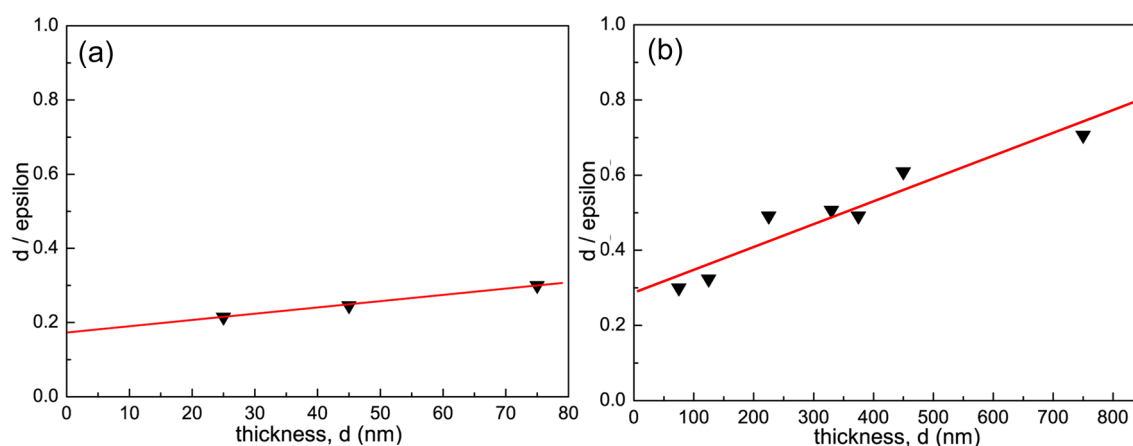


**Fig. 4.47:** Measured ratio  $d/\epsilon$  as a function of the BaTiO<sub>3</sub> film thickness showing different slopes for films with thickness (a) below 75 nm and (b) above 75 nm.

$\epsilon_b$  values can be estimated from the y interception and the slope of the fitted graph presented in Fig. 4.47 according to eq. 4.9. As a result, in the case of thin films (below 75 nm),  $(d_i/\epsilon_i)$  is  $0.085 \pm 0.003$  and  $\epsilon_b$  is  $581.5 \pm 82$ , while in the case of thick films (above 75 nm)  $(d_i/\epsilon_i)$  is  $0.128 \pm 0.03$  and  $\epsilon_b$  is  $1519 \pm 144$ . The last value is in good agreement with the usual bulk dielectric constant of BaTiO<sub>3</sub>.

In the literature, the values of  $(d_i/\epsilon_i)$  measured for (Ba,Sr)TiO<sub>3</sub> films using different electrodes are ranging from a value of 0.887 for Al/(Ba,Sr)TiO<sub>3</sub>/Al [168] to a value of 0.05 for Pt/(Ba,Sr)TiO<sub>3</sub>/Pt [169]. However, the fact that  $d_i$  and  $\epsilon_i$  are not independent in the conventional series capacitor model means that neither the dead-layer thickness nor the dielectric constant is well defined up to this stage of this study. It will be demonstrated in the following that both the thickness and the dielectric constant of the dead layer can actually be well established in the present work.

Coming back to eq. 4.8 and assuming that  $d_b \gg d_i$ , another model is suitable to the experimental data on thick BaTiO<sub>3</sub> films. That is the “dead layer” model developed recently for (Ba,Sr)TiO<sub>3</sub> films by Sinnamon *et al.* [170] to investigate the possibility of a dead layer which acts as a parasitic capacitor.

One aspect vividly discussed in the “dead layer debate” is the influence of film grain size of the ferroelectric film on the dielectric behavior. The film is composed of columnar grains as it was shown in the previous sections of this chapter. Assuming a perfectly columnar structure there is no series capacitor component, and the grain boundary and bulk-like material simply act in parallel (Fig. 4.48). Thus it is possible to calculate the area fractions of the defective material in the grain boundary and of the bulk-like material in a columnar grain of circular section.

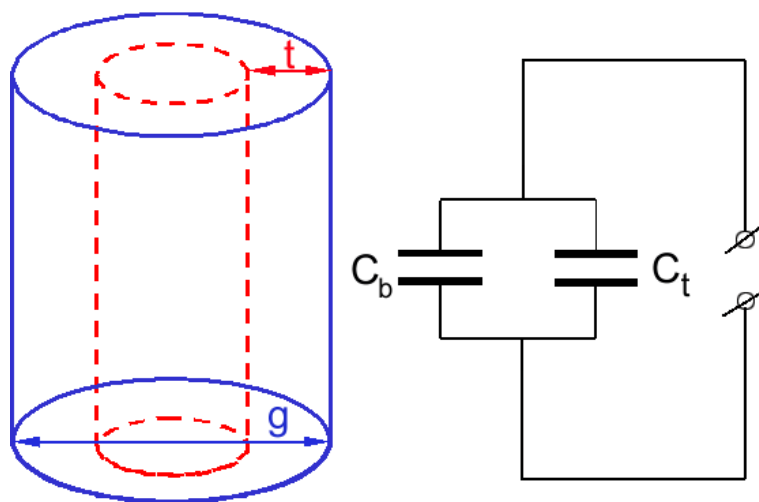


**Fig. 4.48:** A simple schematic of the “dead-layer” acting as a capacitor in parallel to the bulk [170].  $C_b$  is the bulk capacitance,  $C_t$  is the dead layer capacitance,  $g$  is the grain diameter (the grain has a circular section), and  $t$  is the radius of the dead layer (the dead layer has a circular-shaped section).

The effective dielectric constant,  $\epsilon_{eff}$ , is given by the relative area of each capacitor multiplied with its dielectric constant as follows:

$$\epsilon_{eff} = \epsilon_b \left[ \frac{\pi(\frac{g}{2} - t)^2}{\pi(\frac{g}{2})^2} \right] + \epsilon_t \left[ \frac{\pi(\frac{g}{2})^2 - \pi(\frac{g}{2} - t)^2}{\pi(\frac{g}{2})^2} \right] = \frac{4t^2}{g^2} (\epsilon_b - \epsilon_t) - \frac{4t}{g} (\epsilon_b - \epsilon_t) + \epsilon_b \quad (4.10)$$

where  $\epsilon_b$  is the relative dielectric constant of the bulk material,  $t$  is the thickness of the dead layer (grain boundary material) parallel to the grain boundaries,  $g$  is the diameter of the columnar grains, and  $\epsilon_t$  is their relative dielectric constant.

This model is able to reproduce the measured dielectric constant as a function of the lateral size of the grains. Considering this model for  $\text{BaTiO}_3$  films with thickness above 75 nm and fitting the experimental data (shown in Fig. 4.49) with a polynomial function of second order in  $(1/g)$ , the following parameters can be calculated:  $t = 11.95$  nm,  $\epsilon_t = 143.7$ , and  $\epsilon_b = 1254$ . In other words, the thickness of the dead layer is about 12 nm.

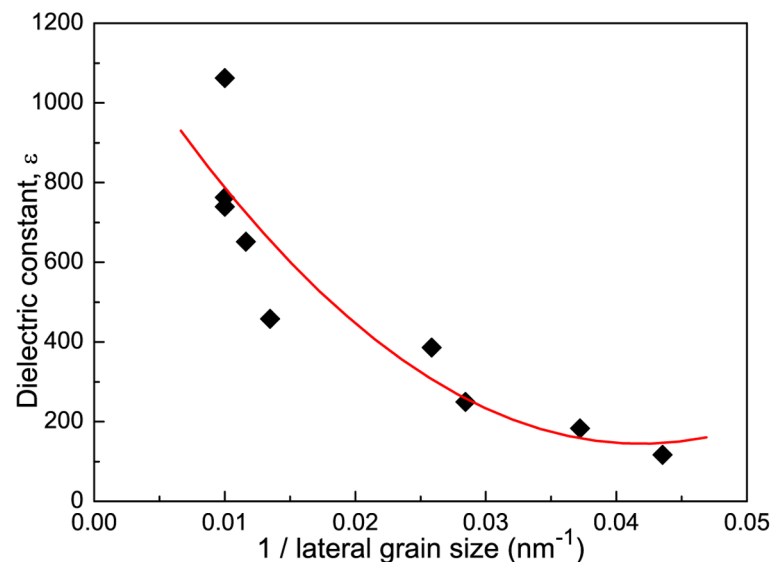


**Fig. 4.49:** Measured dielectric constant as a function of the lateral size of the  $\text{BaTiO}_3$  grains (points) and the polynomial fit (red curve) according to the model of Sinnamón<sup>[170]</sup>.

A natural limit of applicability of the dead-layer model is given by the limiting case when the defective boundary region takes up the entire grain (i.e. when  $t = g/2$ ). At this point  $\epsilon_{eff} = \epsilon_t$  and it will be constant for any further decrease in grain size.

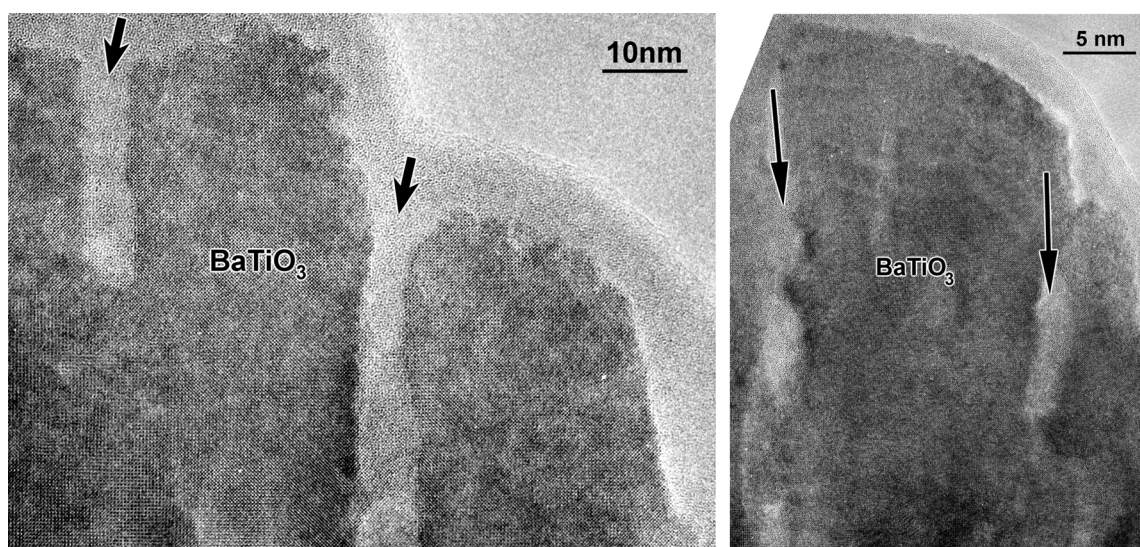


**Fig. 4.50:** Cross-sectional HRTEM images of a thick  $\text{BaTiO}_3$  film showing the presence of grain boundaries and of the dead layer near the grain boundaries. The  $\text{BaTiO}_3$  film thickness is 150 nm.

In conclusion, the assumption of dead layers at the grain boundaries rather than at the ferroelectric/electrode boundaries can be completely rationalized in case of a columnar film structure explaining the decrease in the dielectric constant. In case of BaTiO<sub>3</sub> films presented in this study, the dead layer thickness was calculated as 12 nm.

It should be possible to prove the existence of the dead layers at the grain boundaries, for example, by HRTEM. In the present study, the diameter of the circular section for different film thicknesses was experimentally measured by AFM and confirmed by cross-sectional HRTEM. From Fig. 4.50 taken from a thick BaTiO<sub>3</sub> film (150 nm) dead layers of about 8 nm thickness can be seen (cf. also Fig. 4.30). This value is in rather fair correspondence to the above calculated value of 12 nm, confirming the applicability of Sinammon's model to the films presented in this study.

The applicability of the dead-layer model is restricted to the columnar structure, i.e. above 75 nm film thickness. Therefore this model can not be applied for thin films where no columns occur.

### 4.4.2 BaTiO<sub>3</sub>/SrTiO<sub>3</sub> multilayers

With the background of the above studied dielectric properties of BaTiO<sub>3</sub> films, BaTiO<sub>3</sub>/SrTiO<sub>3</sub> multilayers will be discussed next. Two series of multilayers were prepared, one consists of a BaTiO<sub>3</sub>/SrTiO<sub>3</sub>/BaTiO<sub>3</sub> three-layer system, the other consists of a BaTiO<sub>3</sub>/SrTiO<sub>3</sub>/BaTiO<sub>3</sub>/SrTiO<sub>3</sub>/BaTiO<sub>3</sub> five-layer system. An example of capacitance-voltage measurements performed on thick BaTiO<sub>3</sub>/SrTiO<sub>3</sub> multilayers is presented in Fig. 4.51. The measurement was performed on the sample presented in Fig. 4.41. Figures 4.52(a) and 4.52(b) show the dependence of the effective di-

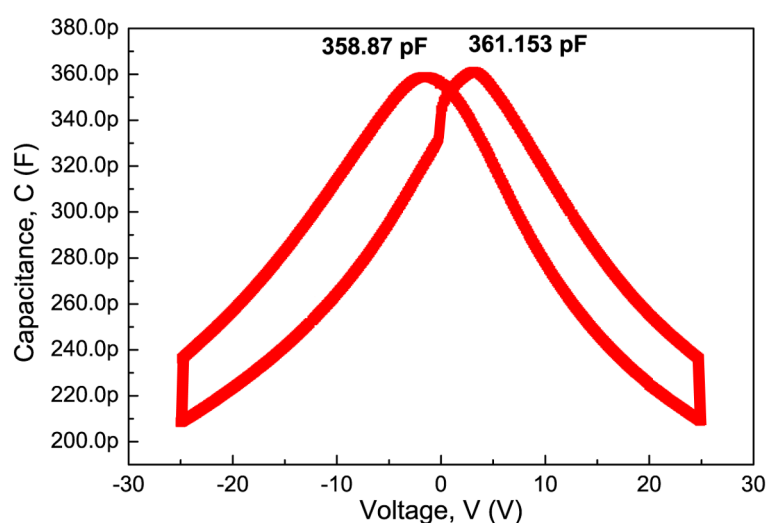


**Fig. 4.51:** Dependence of the capacitance on the applied voltage in case of the thick multilayer sample presented in Fig. 4.41.

electric constant and the dielectric loss tangent on the overall film thickness of the two series of BaTiO<sub>3</sub>/SrTiO<sub>3</sub> multilayers compared with BaTiO<sub>3</sub> films. The turning point at 75 nm is present again, a feature which points to some changes occurring also in BaTiO<sub>3</sub>/SrTiO<sub>3</sub> multilayers at this thickness value. The dielectric loss tangent of the multilayers saturates for a thickness above 300 nm, while below an overall thickness of 75 nm, the dielectric constant linearly decreases with decreasing overall thickness, and this behaviour is independent on the number of multilayers, pointing to some interface effect again.

Somewhat larger values of the dielectric constant were measured for samples consisting of 5 multilayers in comparison with those consisting of 3 multilayers - a fact which is consistent with the literature. Also, the values of the dielectric constant of BaTiO<sub>3</sub>/SrTiO<sub>3</sub> multilayers presented in this study are in good accordance with the values published by other groups: The literature values of the dielectric constant are ranging from 240 [5] to 900 [6] for BaTiO<sub>3</sub>/SrTiO<sub>3</sub> multilayer thicknesses of 30 nm and 100 nm with a periodicity of 5/5 and 4/4 unit cells. The periodicity of the BaTiO<sub>3</sub> and the SrTiO<sub>3</sub> layers has an important influence on the dielectric properties. The dielectric constant decreases from 900 to 500 when the periodicity is changed from 4/4 to 1/1 BaTiO<sub>3</sub>/SrTiO<sub>3</sub> unit cells

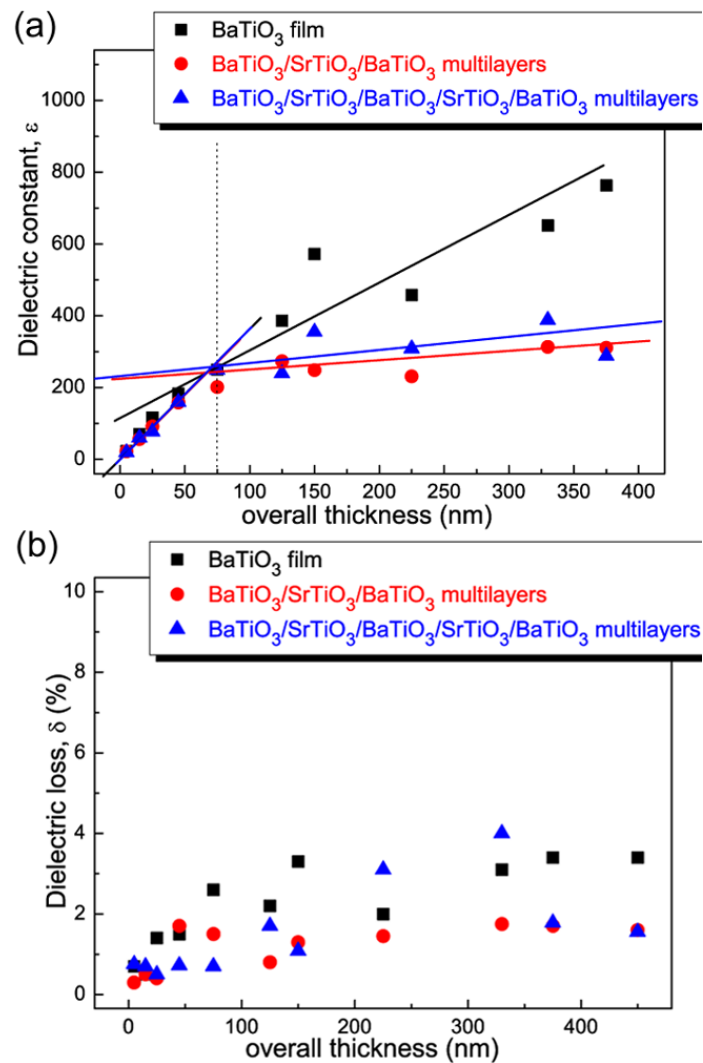


**Fig. 4.52:** Dependence of (a) the effective dielectric constant and (b) dielectric loss tangent on the overall thickness of BaTiO<sub>3</sub>/SrTiO<sub>3</sub> multilayers of the two series explained in the text.

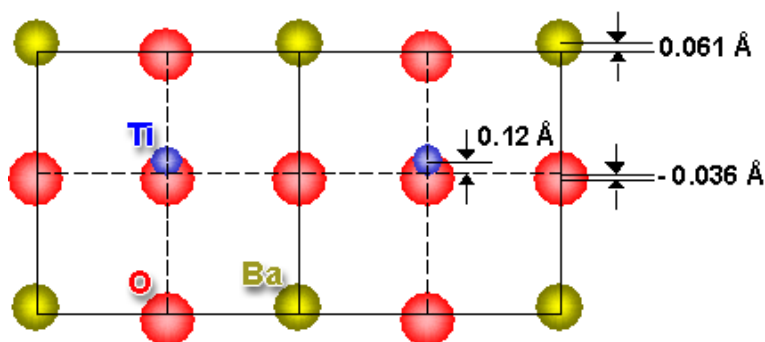


**Fig. 4.53:** Ferroelectric distortions present in BaTiO<sub>3</sub>, according to ref. [6].

due to the stress at the interface which is larger for the 1/1 periodic structure than for the 4/4 periodic structure.

A large dielectric dispersion has been reported for multilayers consisting of 20/20 and 40/40  $\text{BaTiO}_3/\text{SrTiO}_3$  unit cells [7]. A comparison between symmetric and asymmetric  $\text{BaTiO}_3/\text{SrTiO}_3$  structures has shown that a stacking periodicity of 15/3 unit cells exhibits the largest remanent polarization of  $23 \mu\text{C}/\text{cm}^2$ , while the dielectric constant was 240 [5].

It is known that tetragonal  $\text{BaTiO}_3$  exhibits ferroelectric distortions due to displacements of the  $\text{Ba}^{2+}$  and  $\text{Ti}^{4+}$  cations relative to the  $\text{O}^{2-}$  anions, leading to a net dipole per unit area, equivalent to the  $c/a$  lattice distortion of 1.01. A schematic model of these ferroelectric distortions present in  $\text{BaTiO}_3$  is shown in Fig. 4.53, according to ref. [6].

A lattice mismatch of 2.28 % along the  $a$  direction, and one of 3.4 % along the  $c$  direction is present in  $\text{BaTiO}_3/\text{SrTiO}_3$  multilayers. In these multilayers, an interaction between the “ferroelectric” distortion and the lattice mismatch can be expected to occur, resulting in an overall effect on the dielectric and ferroelectric properties. The mismatch strain in the  $\text{BaTiO}_3$  layers relaxes with increasing layer thickness [148]. In addition to the expected reduction of strain with increasing thickness of

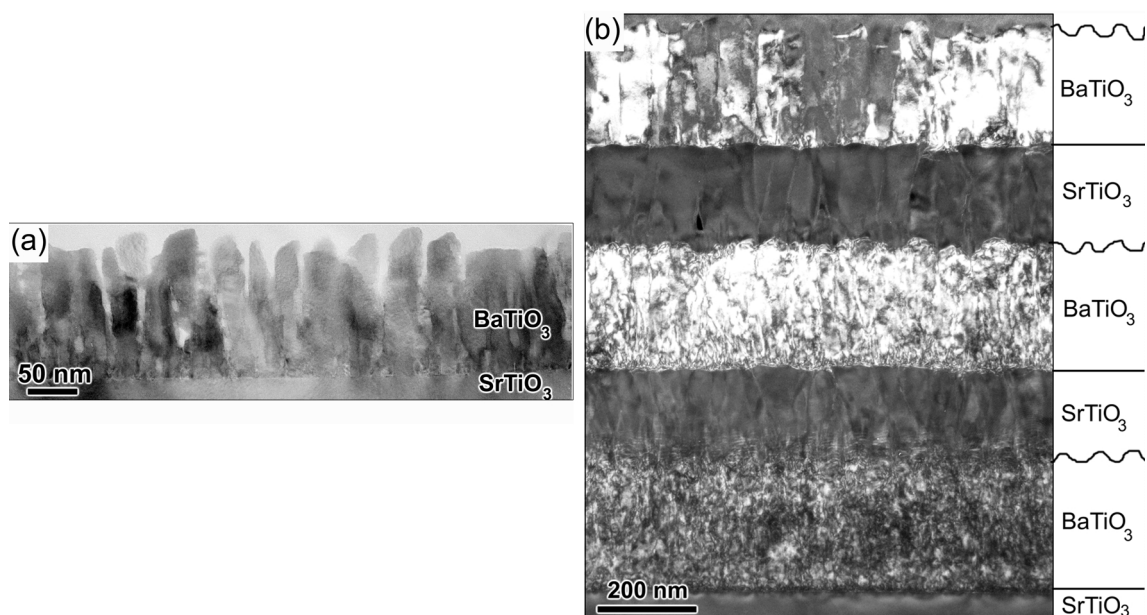


**Fig. 4.54:** (a) Cross-sectional TEM view of an epitaxial  $\text{BaTiO}_3$  film (about 150 nm thick) grown on a  $\text{SrTiO}_3$  substrate. (b) TEM cross-section image of an epitaxial  $\text{BaTiO}_3/\text{SrTiO}_3$  multilayer grown on a  $\text{SrTiO}_3$  (001) substrate. The thickness of the individual  $\text{BaTiO}_3$  layers is about 260 nm, and that of the individual  $\text{SrTiO}_3$  layers is about 210 nm.

the individual  $\text{BaTiO}_3$  layers, the development of a columnar structure in thick layers has to be taken into account. Fig. 4.54(a) shows this columnar structure in a single, about 150 nm thick  $\text{BaTiO}_3$  film, while Fig. 4.54(b) (repeating Fig. 4.41) reveals the presence of a columnar structure in the individual, about 200 nm thick,  $\text{BaTiO}_3$  and  $\text{SrTiO}_3$  layers of a thick multilayer.



Unfortunately, it is very difficult to apply the previously discussed dead layer model onto  $\text{BaTiO}_3/\text{SrTiO}_3$  multilayer systems because too many parameters are involved. Nevertheless, TEM analysis shows the presence of dead layers in  $\text{BaTiO}_3/\text{SrTiO}_3$  multilayers, too (Fig. 4.55). An interesting

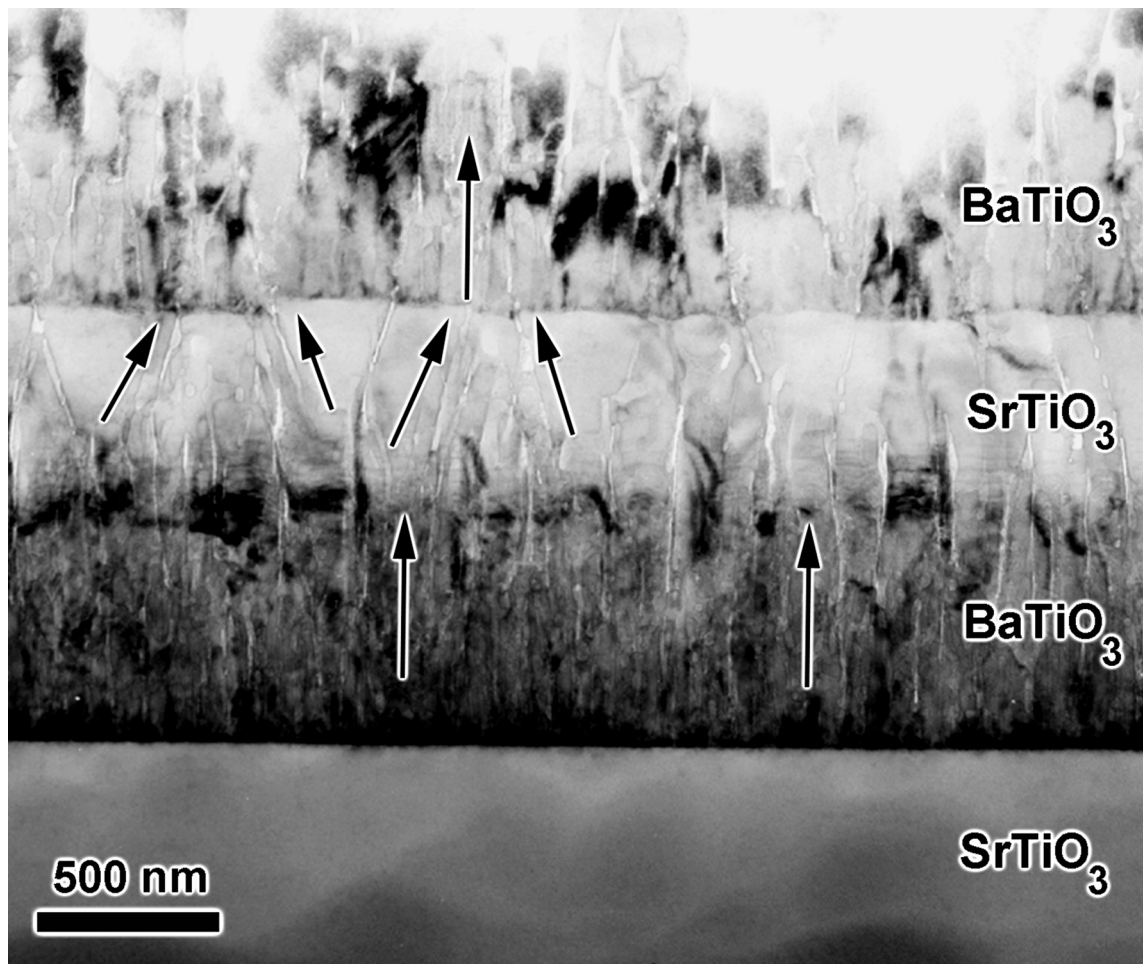


**Fig. 4.55:** TEM image taken in Fresnel contrast revealing the dead layers (indicated by arrows) between  $\text{BaTiO}_3$  grains, as well as between  $\text{SrTiO}_3$  grains.

feature is that dead layers have different direction in different layers. They are parallel to the grains in  $\text{BaTiO}_3$  layers, while in  $\text{SrTiO}_3$  layers they are inclined (Fig. 4.55). This could possibly be explained by the different morphological stability which might result in somewhat differently oriented grain boundaries in the two different layers.

From the point of view of applications, as the thickness of the oxide films decreases to a few tens of nm, a condition required by some devices, the electrical behavior of the films deviates considerably from that of the bulk materials, mainly due to the dependence of the electrical properties on the interfaces. However, it is known that the dielectric constant measured at zero bias decreases drastically with decreasing thickness when metal electrodes (e.g.  $\text{Pt}$ <sup>[167]</sup>) are used, while the dielectric constant is almost independent on the film thickness when conducting oxide electrodes (e.g.  $\text{IrO}_2$ <sup>[166]</sup>,  $\text{SrRuO}_3$ <sup>[171]</sup>) are used. According to ref.<sup>[171]</sup>, the film thickness should be less than 20

nm in ultralarge scale integrated DRAMs with a minimum lateral size of  $0.1 \mu\text{m}$ . A low lateral size favours a high memory density. From this condition it follows that the overall dielectric properties are highly dependent on the interfacial low dielectric layers. Therefore, understanding the nature of the interfacial low dielectric layers has become a critical issue for adopting  $(\text{Ba}/\text{Sr})\text{TiO}_3$  capacitors in DRAMs and the above results hopefully contribute to this purpose.

## 5 Conclusions and outlook

Initial stages of the growth of epitaxial BaTiO<sub>3</sub> films on (001) SrTiO<sub>3</sub> substrates have been studied. A comprehensive study in terms of surface morphology, crystalline orientation, microstructure and film/substrate interface morphology has been carried out applying a combination of investigation techniques such as AFM, HRTEM, and XRD.

The regularly terraced TiO<sub>2</sub>-terminated surfaces of vicinal SrTiO<sub>3</sub>:Nb substrates prepared by a definite chemical and thermal treatment yield regular step patterns with the height of one single unit cell. Effects of different parameters involved in the etching and annealing treatments of substrates of different miscut angles were studied by AFM investigations of the surface morphology. The preparation of single terminated SrTiO<sub>3</sub> (001)-oriented substrate surfaces with regular and sharp edge terraces was successfully achieved by controlling the miscut angle (0.1°), the annealing temperature (1200 °C), and the annealing time (10 min). The chemically and thermally treated vicinal SrTiO<sub>3</sub>:Nb substrate surfaces provided the required reference for the investigation of the initial growth mode of the epitaxial BaTiO<sub>3</sub> thin films.

The morphological analysis of epitaxial BaTiO<sub>3</sub> films of different nominal thicknesses reveals important features of the growth mechanism. A layer-then-island (Stranski-Krastanov) growth mechanism of the epitaxial BaTiO<sub>3</sub> films on the SrTiO<sub>3</sub>:Nb substrates was identified and can be explained as follows:

In the early growth stage, a grainy, but uniform, closed “wetting” layer of 1 nm thickness covers the substrate. This layer, which is apparently free from observable lattice defects, is most probably growing pseudomorphically strained on the SrTiO<sub>3</sub>:Nb substrate due to the small BaTiO<sub>3</sub>/SrTiO<sub>3</sub> lattice misfit. On increasing the film thickness above 5 nm, individual grains begin to grow and the film stress relaxes. This critical thickness of 5 nm represents the turning point when small individual nuclei begin to grow on the surface of the wetting layer. Their density increases on further deposition. Some of these small grains grow further into larger grains of about 100 nm in lateral size which are observed at 40 nm thickness.

The microstructure analysis revealed a grainy structure of the thin BaTiO<sub>3</sub> layer followed by a columnar structure for thick BaTiO<sub>3</sub> films. A sharp interface between the BaTiO<sub>3</sub> film and the SrTiO<sub>3</sub> substrate was observed. XRD and HRTEM investigations confirmed the epitaxial relationship between the BaTiO<sub>3</sub> film and the SrTiO<sub>3</sub> substrate and demonstrated both a good in-plane and out-of-plane orientation. The obtained results, in particular the deduced Stranski-Krastanov growth mechanism, deepen the understanding of the growth of thin perovskite films.

With the aim of improving the dielectric properties, epitaxial BaTiO<sub>3</sub>/SrTiO<sub>3</sub> multilayers were grown by PLD on SrTiO<sub>3</sub> (001) substrates and they were studied in terms of surface morphology, crystalline orientation, microstructure, film/substrate interface morphology, and dielectric properties. The Stranski-Krastanov growth mode was found to govern the growth of the BaTiO<sub>3</sub> layers on the preceding SrTiO<sub>3</sub> layers, as it was observed before for the BaTiO<sub>3</sub> layers grown on SrTiO<sub>3</sub> substrates. Up to 6 nm in thickness, the BaTiO<sub>3</sub> films show no defects and have sharp BaTiO<sub>3</sub>/SrTiO<sub>3</sub> interfaces. In multilayers consisting of thick individual layers, an asymmetry was observed of the morphology, between SrTiO<sub>3</sub>-on-BaTiO<sub>3</sub> and BaTiO<sub>3</sub>-on-SrTiO<sub>3</sub> interfaces. This feature is most probably due to a difference in the morphological stability of the growth surfaces caused by different surface energies and different mobilities of the Ba and Sr atoms reaching the SrTiO<sub>3</sub> and BaTiO<sub>3</sub> layer, respectively. Dielectric measurements were performed on BaTiO<sub>3</sub> films and on BaTiO<sub>3</sub>/SrTiO<sub>3</sub> multilayers of different overall thickness. Below an overall thickness of 75 nm, the dielectric constant shows a sharp linear decrease with decreasing overall thickness and does not depend on the number of multilayers. This behaviour is most probably caused by dead layers of low dielectric constant extending vertically along the column boundaries.

The obtained results, in particular the deduced Stranski-Krastanov growth mechanism, are particularly significant in view of actual efforts to grow artificial superlattices involving very thin individual layers of BaTiO<sub>3</sub> and/or SrTiO<sub>3</sub>. For example, epitaxial BaTiO<sub>3</sub>/SrTiO<sub>3</sub> artificial superlattices with a thickness of the individual layers in the order of 5 to 10 nm are currently studied aiming at either an improvement of the ferroelectric properties or the achievement of new dielectric properties. Optimizing these properties certainly requires a good understanding of the initial growth mode of these very thin individual layers, to which the present results should be able to contribute. Most probably, these observations are not restricted to ferroelectric systems, but applicable more generally to different oxide superlattice systems that follow a Stranski-Krastanov growth mechanism.

# Bibliography

- [1] S. K. Streiffer, C. Basceri, C. B. Parker, S. E. Lash, and A. I. Kingon, *J. Appl. Phys.*, **86**, 4565 (1999).
- [2] C. Dubourdieu, R. Pantou, F. Weiss, J. P. Sénateur, E. Dooryhee, J. L. Hodeau, M. Nemoz, G. Köbernik, and W. Haessler, *Ferroelectrics*, **268**, 557 (2002).
- [3] T. Hayashi and T. Tanaka, *Jpn. J. Appl. Phys.*, **34**, 5100 (1995).
- [4] B. D. Qu, M. Evstigneev, D. J. Johnson, and R. H. Prince, *Appl. Phys. Lett.*, **72**, 1394 (1998).
- [5] T. Shimuta, O. Nakagawara, T. Makino, S. Arai, H. Tabata, and T. Kawai, *J. Appl. Phys.*, **91**, 2290 (2002).
- [6] H. Tabata, H. Tanaka, and T. Kawai, *Appl. Phys. Lett.*, **65**, 1970 (1994).
- [7] T. Tsurumi, S. Mitarai, S. M. Nam, Y. Ishibashi, and O. Fukunaga, *IEEE 10-th International Symposium on Applications of Ferroelectrics, Proceedings*, **1**, 499 (1996).
- [8] Z. Wang, T. Yasuda, S. Hatatani, and S. Oda, *Jpn. J. Appl. Phys.*, **38**, 6817 (1999).
- [9] Q. D. Jiang, Z. J. Huang, C. L. Chen, A. Brazdeikis, P. Jin, H. H. Feng, A. Benneker, and C. W. Chu, *Mat. Res. Soc. Symp. Proc.*, **493**, 243 (1998).
- [10] Y. S. Kang, I. Tanaka, H. Adaki, and S. J. Park, *Jpn. J. Appl. Phys.*, **35**, L1614 (1996).
- [11] J. Valasek, *Phys. Rev.*, **17**, 475 (1921).
- [12] T. Mitsui, I. Tatsuzaki, and E. Nakamura, In: *An introduction to the physics of ferroelectrics*, G. W. Taylor (Ed.) , Gordon and Breach Science Publishers, London, 1976, p. 7.
- [13] G. A. Smolenskii, V. A. Bokov, N. N. Isupov, V. A. Krainik, R. E. Pasynkov, and A. I. Sokolov, In: *Ferroelectrics and related phenomena*, G. A. Smolenskii (Ed.) , Gordon and Breach Science Publishers, Amsterdam, 1984, p. 185.
- [14] W. Känzig, *Ferroelectrics*, **74**, 285 (1987).
- [15] M. Suzuki and T. Ami, *Mater. Sci. Eng.*, **B41**, 166 (1996).
- [16] J. C. Slater, *Phys. Rev.*, **78**, 748 (1950).
- [17] R. E. Cohen, *Nature*, **358**, 136 (1992).
- [18] A. F. Devonshire, *Phil. Mag.*, **40**, 1040 (1949).

- [19] A. F. Devonshire, *Phil. Mag.*, **42**, 1065 (1951).
- [20] G. A. Smolenskii, V. A. Bokov, N. N. Isupov, V. A. Krainik, R. E. Pasynkov, and A. I. Sokolov, In: *Ferroelectrics and related phenomena*, G. A. Smolenskii (Ed.) , Gordon and Breach Science Publishers, Amsterdam, 1984, p. 3.
- [21] G. A. Smolenskii, V. A. Bokov, N. N. Isupov, V. A. Krainik, R. E. Pasynkov, and A. I. Sokolov, In: *Ferroelectrics and related phenomena*, G. A. Smolenskii (Ed.) , Gordon and Breach Science Publishers, Amsterdam, 1984, p. 422.
- [22] N. Lemée, C. Dubourdieu, G. Delabouglise, J. P. Sénateur, and F. Laroudie, *J. Crystal Growth*, **235**, 347 (2002).
- [23] R. A. Cowley, *Phys. Rev. Lett.*, **9**, 159 (1962).
- [24] M. E. Lines and A. M. Glass, In: *Principles and Applications of Ferroelectrics and Related Materials*, W. Marchall and D.H. Wilkinson (Eds.) , Clarendon Press, Oxford, 1977, p. 255.
- [25] J. F. Schooley, W. R. Hosler, and M. L. Cohen, *Phys. Rev. Lett.*, **12**, 474 (1964).
- [26] M. J. Akhtar, Z. N. Akhtar, R. Jackson, C. Richard, and A. Catlow, *J. Am. Ceram. Soc.*, **78**, 421 (1995).
- [27] K. A. Mueller and H. Burkard, *Phys. Rev. B*, **19**, 3593 (1979).
- [28] P. Y. Lesaicherre, H. Yamaguchi, Y. Miyasaka, H. Watanabe, H. Ono, and M. Yoshida, *Integrated Ferroelectrics*, **8**, 201 (1995).
- [29] A. T. Findikoglu, Q. X. Jia, X. D. Wu, G. J. Chen, T. Vankatesan, and D. W. Reagor, *Appl. Phys. Lett.*, **68**, 1651 (1996).
- [30] F. A. Miranda, R. R. Ramanofski, F. W. VanKeuls, C. H. Mueller, R. E. Treece, and T. V. Rivkin, *Integrated Ferroelectrics*, **17**, 231 (1997).
- [31] M. J. Lancaster, J. Powell, and A. Porch, *Supercond. Sci. Technol.*, **11**, 1323 (1998).
- [32] J. A. Venables and G. L. Price, In: *Epitaxial growth, Part B*, J. W. Matthews (Ed.) , Academic Press, New York, 1975, p. 382.
- [33] K. Sangwal and R. Rodriguez-Clemente, In: *Surface Morphology of Crystalline Solids*, Trans Tech, Zürich, 1991, p. 13.
- [34] K. Sangwal and R. Rodriguez-Clemente, In: *Surface Morphology of Crystalline Solids*, Trans Tech, Zürich, 1991, p. 14.
- [35] K. Sangwal and R. Rodriguez-Clemente, In: *Surface Morphology of Crystalline Solids*, Trans Tech, Zürich, 1991, p. 144.
- [36] P. Hartman, In: *Crystal Growth - an Introduction*, North -Holland, Amsterdam, 1973, p. 368.
- [37] I. V. Markov, In: *Crystal Growth for Beginners*, World Scientific, New Jersey, 1995, p. 283.
- [38] L. Royer, *Bull. Soc. Fr. Mineralog. Cristallogr.*, **51**, 7 (1928).

- [39] F. C. Frank and J. H. van der Merwe, Proc. Res. Soc. A, **198**, 205 (1949).
- [40] I. V. Markov, In: *Crystal Growth for Beginners*, World Scientific, New Jersey, 1995, p. 376.
- [41] J. S. Horwitz and J. A. Sprague, In: *Pulsed Laser Deposition of Thin Films*, D. B. Chrisey and G. K. Hubler (Eds.) , Wiley, New York, 1994, p. 231.
- [42] J. H. van der Merwe, J. Woltersdorf, and W. A. Jesser, Mater. Sci. Eng., **81**, 1 (1986).
- [43] J. E. Greene, In: *Multicomponent and multilayered thin films for advanced microtechnologies: techniques, fundamentals and devices*, O. Auciello and J. Engemann (Eds.) , Klumer Academic Publishers, Dordrecht, 1993, p. 42.
- [44] M. H. Grabow and G. H. Gilmer, Surf. Sci., **194**, 333 (1988).
- [45] C. Noguera, In: *Physics and chemistry at oxide surfaces*, Cambridge University Press, Cambridge, 1996.
- [46] I. Markov and S. Stoyanov, Contemp. Phys., **28**, 267 (1987).
- [47] R. W. Whatmore, Ferroelectrics, **255**, 179 (1999).
- [48] R. Kohler, N. Neumann, N. Hess, R. Bruchhaus, W. Wersing, and M. Simon, Ferroelectrics, **201**, 83 (1997).
- [49] C. J. Brierley, C. Trundle, L. Considine, R. W. Whatmore, and F. M. Ainger, Ferroelectrics, **91**, 181 (1989).
- [50] Ferroelectricity Newsletter, **4** (Fall, 1996 - Special Issue on Chemical Solution Deposition).
- [51] N. M. Shorrocks, A. Patel, M. J. Walker, and A. D. Parsons, Microelectronic Engineering, **29**, 59 (1995).
- [52] M. Alexe, C. Harnagea, D. Hesse, and U. Gösele, Appl. Phys. Lett., **75**, 1793 (1999).
- [53] M. Alexe, C. Harnagea, D. Hesse, and U. Gösele, Appl. Phys. Lett., **79**, 242 (2001).
- [54] S. Matsui and K. Mori, J. Vac. Sci. Technol., **B4**, 299 (1986).
- [55] K. Mori and S. Okamura, Jpn. J. Appl. Phys., **31**, L1143 (1992).
- [56] S. Okamura, Y. Yagi, S. Ando, T. Tsukamoto, and K. Mori, Jpn. J. Appl. Phys., **35**, 6579 (1996).
- [57] M. Hiratani, C. Okazaki, H. Hasegawa, N. Sugii, Y. Tarutani, and K. Takagi, Jpn. J. Appl. Phys., **36**, 5219 (1997).
- [58] A. Stanishevsky, S. Aggarwal, A. S. Prakash, J. Melngailis, and R. Ramesh, J. Vac. Sci. Technol., **B16**, 3899 (1998).
- [59] R. Nötzel, Semicond. Sci. Technol., **11**, 1365 (1996).
- [60] D. J. Eaglesham and M. Cerullo, Phys. Rev. Lett., **64**, 1943 (1990).



- [61] S. Guha, A. Madhukar, and K. C. Rajkumar, *Appl. Phys. Lett.*, **57**, 2110 (1990).
- [62] C. Deshpandey and R. Bunshah, In: *Thin Film Processes*, J. L. Vossen and W. Kern (Eds.) , Academic Press, San Diego, 1991, p. 79.
- [63] R. Parsons and J. A. Sprague, In: *Thin Film Processes*, J. L. Vossen and W. Kern (Eds.) , Academic Press, San Diego, 1991, p. 177.
- [64] P. P. Chow, In: *Thin Film Processes*, J. L. Vossen and W. Kern (Eds.) , Academic Press, San Diego, 1991, p. 133.
- [65] R. Kelly and R. W. Dreyfus, *Surf. Sci.*, **198**, 263 (1988).
- [66] K. F. Jensen and W. Kern, In: *Thin Film Processes*, J. L. Vossen and W. Kern (Eds.) , Academic Press, San Diego, 1991, p. 283.
- [67] S. Kumar and A. Mansingh, *IEEE 7-th International Symposium on Applications of Ferroelectrics, Proceedings*, 717 (1991).
- [68] M. Sayer, *IEEE 6-th International Symposium on Applications of Ferroelectrics, Proceedings*, 560 (1986).
- [69] S. T. Lee, N. Fujimura, and T. Ito, *Jpn. J. Appl. Phys.*, **34**, 5168 (1995).
- [70] K. Abe and S. Komatsu, *Mat. Res. Soc. Symp. Proc.*, **361**, 465 (1995).
- [71] D. G. Schlom, J. N. Eckstein, I. Bozovic, Z. J. Chen, A. F. Marshall, K. E. Dessonneck, and J. S. Harris, *Growth of Semiconductor Structures and High-Tc Thin Films on Semiconductors, SPIE Proceedings*, **1285**, 234 (1990).
- [72] C. D. Theis, J. Yeh, D. G. Schlom, M. E. Hawley, and G. W. Brown, *Mater. Sci. Eng.*, **B56**, 228 (1998).
- [73] Y. Yoneda, K. Sakaue, and H. Terauchi, *Jpn. J. Appl. Phys.*, **39**, 4839 (2000).
- [74] Y. Yoneda, T. Okabe, K. Sakaue, and H. Terauchi, *J. Appl. Phys.*, **83**, 2458 (1998).
- [75] Y. Yoneda, T. Okabe, K. Sakaue, and H. Terauchi, *Surf. Sci.*, **410**, 62 (1998).
- [76] R. G. Gordon, C. Feng, N. J. Diceglie, A. Kenigsberg, L. Xinye, and J. Teff, D. J. Thornton, *Mat. Res. Soc., Chemical Aspects of Electronic Ceramics Processing Symposium*, **495**, 63 (1998).
- [77] J. Lindner, M. Schumacher, M. Dauelsberg, F. Schienle, S. Miedl, D. Burgess, E. Merz, G. Strauch, and H. Juergensen, *Advanced Materials for Optics and Electronics*, **10**, 163 (2000).
- [78] B. Bihari, J. Kumar, G. T. Stauf, P. C. Buckirk, and C. S. Hwang, *J. Appl. Phys.*, **76**, 1169 (1994).
- [79] L. H. Robins, D. L. Kaiser, L. D. Rotter, K. P. Schenck, G. T. Stauf, and D. Rytz, *J. Appl. Phys.*, **76**, 7487 (1994).
- [80] T. Tohma, H. Masumoto, T. Hirai, and T. Goto, *Mater. Trans.*, **42**, 702 (2001).

- [81] D. L. Kaiser, M. D. Vaudin, G. Gillen, C.-S. Hwang, L. H. Robins, and L. D. Rotter, *J. Crystal Growth*, **137**, 136 (1994).
- [82] P. C. Van Buskirk, R. Gardiner, P. S. Kirilin, and S. B. Krupanidhi, *IEEE 8-th International Symposium on Applications of Ferroelectrics, Proceedings*, 340 (1992).
- [83] Y. M. Chen, D. Ritums, N. J. Wu, and A. Ignatiev, *IEEE 11-th International Symposium on Applications of Ferroelectrics, Proceedings*, 43 (1998).
- [84] H. Wang, J. M. Zeng, Z. Wang, M. Wang, and S. X. Shang, *SPIE Proceedings*, **2896**, 264 (1996).
- [85] S. B. Ogale, S. M. Kanetkar, S. M. Chaudhari, V. P. Godbole, V. N. Koinkar, S. Joshi, R. Nawathey, and A. R. Moghe, *Ferroelectrics*, **102**, 85 (1990).
- [86] J.-P. Maria, Mc-K. Trolier, and D. G. Schlom, *IEEE 10-th International Symposium on Applications of Ferroelectrics, Proceedings*, **1**, 333 (1996).
- [87] P. K. Shenck, M. D. Vaudin, D. W. Bonnell, J. W. Hastie, and A. J. Paul, *Appl. Surf. Sci.*, **127-129**, 655 (1998).
- [88] O. Auciello, In: *Handbook of Crystal Growth*, volume 3A, D. T. J. Hurle (Ed.) , Elsevier Science, Amsterdam, 1994, p. 367.
- [89] J. T. Cheung, In: *Pulsed Laser Deposition of Thin Films*, D. B. Chrisey and G. K. Hubler (Eds.) , Wiley, New York, 1994, p. 10.
- [90] J. G. Bednorz and K. A. Müller, *Z. Phys.*, **B64**, 189 (1986).
- [91] R. K. Singh and J. Narayan, *Phys. Rev. B*, **41**, 8843 (1990).
- [92] R. K. Singh and J. Narayan, *Mater. Sci. Eng.*, **B3**, 217 (1989).
- [93] R. Ramesh, A. Inam, W. K. Chan, B. Wilkens, K. Myers, K. Reimschnig, D. L. Hart, and J. M. Tarascon, *Science*, **252**, 944 (1991).
- [94] Y. Shibata, K. Kaya, K. Akashi, M. Kanai, T. Kawai, and S. Kawai, *Appl. Phys. Lett.*, **61**, 1000 (1992).
- [95] K. R. Carroll, J. M. Pond, D. B. Chrisey, J. S. Horwitz, R. E. Leuchtner, and K. S. Grabowski, *Appl. Phys. Lett.*, **62**, 1845 (1993).
- [96] S. B. Krupanidhi, M. Sayer, K. El-Assal, C. K. Jen, and G. W. Farnell, *J. Can. Ceram. Soc.*, **54**, 28 (1984).
- [97] H. Adachi, T. Mitsuyo, O. Yamazaki, and K. Wasa, *J. Appl. Phys.*, **60**, 736 (1986).
- [98] N. Ichinose, Y. Hirao, N. Nakamoto, and T. Tamshita, *Jpn. J. Appl. Phys.*, **24**, 463 (1985).
- [99] A. P. Jardine, G. C. Johnson, A. Crowson, and M. Allen, *Mat. Res. Soc. Symp. Proc.*, **276**, 1 (1992).
- [100] A. J. Mulson and J. M. Herbert, In: *Electroceramics*, Chapman and Hall, New York, 1990.

- [101] O. Auciello and A. I. Kingon, IEEE 8-th International Symposium on Applications of Ferroelectrics, Proceedings, **1**, 320 (1992).
- [102] H. N. Lee, A. Visinoiu, S. Senz, C. Harnagea, C. Pignolet, D. Hesse, and U. Gösele, J. Appl. Phys., **88**, 6658 (2000).
- [103] J. T. Cheung and H. Sankur, Critical Review in Solid State and Materials Science, **15**, 63 (1988).
- [104] H. Schwartz and H. A. Tourtellote, J. Vac. Sci. Technol., **6**, 373 (1969).
- [105] O. Auciello, Materials and Manufacturing Processes, **6**, 33 (1991).
- [106] T. Kuroiwa, Y. Tsunemine, T. Horikawa, T. Makita, J. Tanimura, N. Mikami, and K. Sato, Jpn. J. Appl. Phys., **33**, 5187 (1994).
- [107] K. Iijima, T. Terashima, Y. Bando, K. Kamigaki, and H. Terauchi, J. Appl. Phys., **72**, 2840 (1992).
- [108] K. Sakayori, Y. Matsui, H. Abe, E. Nakamura, M. Kenmoku, T. Hara, D. Ishikawa, A. Kokubu, K. Hirota, and T. Ikeda, Jpn. J. Appl. Phys., **34**, 5443 (1995).
- [109] S. Fähler, M. Störmer, and H. U. Krebs, Appl. Surf. Sci., **109-110**, 433 (1997).
- [110] T. Kusumori and H. Muto, Physica C: Superconductivity, **351**, 227 (2001).
- [111] M. G. Norton and C. B. Carter, J. Mater. Res., **5**, 2762 (1990).
- [112] G. M. Davis and M. C. Gower, Appl. Phys. Lett., **55**, 112 (1989).
- [113] W. J. Lin, T. Y. Tseng, H. B. Lu, S. L. Tu, S. J. Yang, and I. N. Lin, J. Appl. Phys., **77**, 6466 (1995).
- [114] J. Gonzalo, R. Gomez San Roman, J. Perriere, C. N. Afonso, and R. Perez Casero, Appl. Phys. A, **66**, 487 (1998).
- [115] D. Y. Kim, S. G. Lee, Y. K. Park, and S. J. Park, Jpn. J. Appl. Phys., **36**, 7307 (1997).
- [116] J. Zhang, Jpn. J. Appl. Phys., **36**, 276 (1997).
- [117] A. Ito, A. Machida, and M. Obara, Integrated Ferroelectrics, **20**, 87 (1998).
- [118] A. S. Hwang, M. D. Vaudin, and P. K. Schenck, J. Mater. Res., **13**, 368 (1998).
- [119] V. Srikant, E. J. Tarsa, D. R. Clarke, and J. S. Speck, J. Appl. Phys., **77**, 1517 (1995).
- [120] W. J. Kim, J. C. Rife, J. S. Horwitz, R. C. Y. Auyeung, D. B. Chrisey, M. I. Bell, and R. W. Smith, Mat. Res. Soc. Symp. Proc., **541**, 635 (1999).
- [121] M. N. Khan, H. T. Kim, T. Kusawake, H. Kudo, K. Oshima, and H. Uwe, J. Appl. Phys., **86**, 2307 (1999).
- [122] T. Suzuki, Y. Nishi, and M. Fujimoto, Jpn. J. Appl. Phys., **39**, 5970 (2000).

- [123] L. Beckers, J. Schubert, W. Zander, J. Ziesmann, A. Eckau, P. Leinenbach, and C. Buchal, *J. Appl. Phys.*, **83**, 3305 (1998).
- [124] Y. Liu, Z. Chen, C. Li, D. Cui, Y. Zhou, and G. Yang, *J. Appl. Phys.*, **81**, 6328 (1997).
- [125] Y. A. Boikov and T. Claeson, *J. Appl. Phys.*, **89**, 5053 (2001).
- [126] K. Iijima, T. Terashima, K. Yamamoto, K. Hirata, and Y. Bando, *Appl. Phys. Lett.*, **56**, 527 (1990).
- [127] T. Terashima, Y. Bando, K. Iijima, K. Yamamoto, K. Hirata, K. Hayashi, K. Kamigaki, and H. Terauchi, *Phys. Rev. Lett.*, **65**, 2684 (1990).
- [128] Z. P. Zheng, Q. Y. Ying, S. Witanachi, Z. Q. Huang, D. T. Shaw, and H. S. Kwok, *Appl. Phys. Lett.*, **54**, 954 (1989).
- [129] R. Kelly and A. Miotello, In: *Pulsed Laser Deposition of Thin Films*, D. B. Chrisey and G. K. Hubler (Eds.) , Wiley, New York, 1994, p. 55.
- [130] D. B. Geohegan, In: *Pulsed Laser Deposition of Thin Films*, D. B. Chrisey and G. K. Hubler (Eds.) , Wiley, New York, 1994, p. 115.
- [131] D. H. A. Blank, G. Koster, G. Rinders, E. van Setten, P. Slycke, and H. Rogalla, *Appl. Phys. A: Mater. Sci. Process.*, **69**, S17 (1999).
- [132] W. C. Goh, S. Y. Xu, S. J. Wang, and C. K. Ong, *J. Appl. Phys.*, **89**, 4497 (2001).
- [133] D. H. A. Blank, G. Koster, G. Rijnders, E. van Setten, P. Slycke, and H. Rogalla, *J. Cryst. Growth*, **211**, 98 (2000).
- [134] S. Battaglia, M. Franzini, and L. Leoni, *Powder Diffr.*, **7**, 194 (1992).
- [135] L. S. Zevin and G. Kimmel, In: *Quantitative x-ray diffractometry*, I. Mureinik (Ed.) , Springer, New York, 1995, p. 352.
- [136] J. A. Bearden, *Rev. Mod. Phys.*, **39**, 78 (1967).
- [137] S. P. Chen, *J. Mater. Res.*, **13**, 8148 (1998).
- [138] G. Koster, G. Rijnders, D. H. A. Blank, and H. Rogalla, *Physica C: Superconductivity*, **339**, 215 (2000).
- [139] M. Kawasaki, K. Takahashi, T. Maeda, R. Tsuchiya, M. Shinohara, O. Ishiyama, T. Yonezawa, M. Yoshimoto, and Koinuma H., *Science*, **266**, 1540 (1994).
- [140] Y. Liang and D. A. Bonell, *Surf. Sci.*, **310**, 128 (1994).
- [141] Y. Liang and D. A. Bonell, *J. Am. Ceram. Soc.*, **78**, 2633 (1995).
- [142] K. Szot, W. Speier, J. Herion, and Ch. Freiburg, *Appl. Phys. A*, **64**, 55 (1996).
- [143] T. T. Tsong, In: *Surface diffusion - Atomistic and collective processes*, M. C. Tringides (Ed.) , Plenum Press, New York, 1997, p. 49.

- [144] W. Wunderlich, M. Fujimoto, and H. Ohsato, *Mater. Sci. Eng.*, **A309-310**, 148 (2001).
- [145] W. C. Goh, S. Y. Xu, S. J. Wang, and C. K. Ong, *J. Appl. Phys.*, **89**, 4497 (2001).
- [146] S. Y. Xu, C. K. Ong, and X. Zhang, *Solid State Commun.*, **107**, 273 (1998).
- [147] K. D. Develos, M. Kusunoki, and S. Ohshima, *Jpn. J. Appl. Phys.*, **37**, 6161 (1998).
- [148] H. Tabata, H. Tanaka, T. Kawai, and M. Okuyama, *Jpn. J. Appl. Phys.*, **34**, 544 (1995).
- [149] R. A. McKee, F. J. Walker, E. D. Specht, G. E. Jellison, and L. A. Boatner, *Phys. Rev. Lett.*, **72**, 2741 (1994).
- [150] W. W. Mullins and R. F. Sekerka, *J. Appl. Phys.*, **35**, 444 (1964).
- [151] M. Martin, In: *Reactivity of solids: Past, present and future*, V. V. Bolyrev (Ed.) , Blackwell Science, Paris, 1996, p. 91.
- [152] T. Hayashi and T. Tanaka, *Jpn. J. Appl. Phys.*, **33**, 5277 (1994).
- [153] L. J. Sinnamon, R. M. Bowman, and J. M. Gregg, *Appl. Phys. Lett.*, **78**, 1724 (2001).
- [154] M. Dawber, L. J. Sinnamon, J. F. Scott, and J. M. Gregg, *Ferroelectrics*, **268**, 455 (2002).
- [155] V. G. Bhide, R. T. Gonhalekar, and S. N. Shringi, *J. Appl. Phys.*, **36**, 3825 (1965).
- [156] G. Teowee, C. D. Baertlein, E. A. Kneer, J. M. Boulton, and D. R. Uhlmann, *Integrated Ferroelectrics*, **7**, 149 (1995).
- [157] I. Stolichnov, A. Tagantsev, N. Setter, J. S. Cross, and M. Tsukada, *Appl. Phys. Lett.*, **75**, 1790 (1999).
- [158] D. Choi, B. Kim, S. Son, S. Oh, and K. Park, *J. Appl. Phys.*, **86**, 3347 (1999).
- [159] M. Izuha, K. Abe, and N. Fukushima, *Jpn. J. Appl. Phys.*, Part 1, **36**, 5866 (1997).
- [160] V. Craciun and R. K. Singh, *Appl. Phys. Lett.*, **76**, 1932 (2000).
- [161] C. Zhou and D. M. Newns, *J. Appl. Phys.*, **82**, 3081 (1997).
- [162] K. Natori, D. Otani, and N. Sano, *Appl. Phys. Lett.*, **73**, 632 (1998).
- [163] P. Wurfel and I. P. Batra, *Phys. Rev. B*, **8**, 5126 (1973).
- [164] Y. G. Wang, W. L. Zhong, and P. L. Zhang, *Phys. Rev. B*, **51**, 5311 (1995).
- [165] O. G. Vendik, S. P. Zubko, and L. T. Ter-Martirosayn, *Appl. Phys. Lett.*, **73**, 37 (1998).
- [166] C. S. Hwang, B. T. Lee, C. S. Kang, K. H. Lee, H. J. Cho, H. Hideki, W. D. Kim, Lee. S. I., and M. Y. Lee, *J. Appl. Phys.*, **85**, 287 (1999).
- [167] C. S. Hwang, *J. Appl. Phys.*, **92**, 432 (2002).
- [168] N. Ichinose and T. Ogiwara, *Jpn. J. Appl. Phys.*, **34**, 5198 (1995).

- [169] W. J. Lee, H. G. Kim, and S. G. Yoon, *J. Appl. Phys.*, **80**, 5891 (1996).
- [170] L. J. Sinnamon, M. M. Saad, R. M. Bowman, and J. M. Gregg, *Appl. Phys. Lett.*, **81**, 703 (2002).
- [171] K. Hieda, K. Eguchi, N. Fukushima, T. Aoyama, K. Natori, M. Kiyotoshi, S. Yamazaki, M. Izuha, S. Niwa, Y. Fukuzumi, Y. Ishibashi, Y. Kohyama, T. Arikado, and K. Okumura, *IEEE International Electron Devices Meeting, New York, Proceedings*, 807 (1998).

# Eidesstattliche Erklärung

Ich erkläre, dass ich keine anderen als die von mir angegebenen Quellen und Hilfsmittel zur Erstellung meiner Dissertation verwendet habe. Den benutzten Werken wörtlich oder inhaltlich entnommene Stellen sind als solche gekennzeichnet.

Alina Visinoiu

Halle / Saale, am 10 Februar 2002



# Acknowledgements

This work benefited from the help and advices of the people around me. It is my pleasure to thank my research supervisors, my colleagues and my friends.

I have been fortunate to work at the Max Planck Institute of Microstructure Physics. I would like to thank Prof. Ulrich Gösele for offering me this opportunity.

My special thanks go to Priv.-Doz. Dr. Dietrich Hesse for his constant encouragement, his confidence and his continuous technical and moral support devoted to an extended guidance over the professional work. His enthusiasm, openness to new ideas and uncompromising faith in people have been the leading qualities, which I wish I would inherit.

A great challenge has been to work together with Dr. Marin Alexe and part of my knowledge are due to his constant support and many long discussions encouraging me to strive to become a good scientist. I would like to say a sincere “Multumesc” to him for all his effort and his help extended over physics and my personal welfare.

I owe a great debt to Dr. Ho Nyung Lee for his constant encouragement, his advices and good ideas. Part of my knowledge about pulsed laser deposition and experimental techniques is the result of many discussions and our active collaboration.

I am very grateful to Dr. Roland Scholz and Dr. Dima N. Zakharov for the Transmission Electron Microscopy analysis and for many advices during our discussions.

I take this opportunity to thank Prof. Alain Pignolet for scientific discussions and the coordination of my work. I thank Dr. Catalin Harnagea who helped me to understand and perform the Atomic Force Microscopy investigations.

Many thanks to my Romanian friends for their warm friendship, and their moral support as well as for being the persons helping me day by day to overcome problems.

A special gratitude to my parents and my brother who helped me a lot inspite of the physical distance giving me hope, encouragement and support whenever needed.

I apologize if I forgot somebody. I do appreciate all the people who helped me in one way or another and I would like to say to all: “Thank you very much” and I hope I can return their help whenever they will need it.

# Curriculum Vitae

## Personal information

**Name:** **VISINOIU Alina Mihaela**  
**Permanent address:** Viilor Str. P12, Apt. 6, 0300 Pitesti (Arges), Romania  
**Date and place of birth:** 27 June 1974, Pitesti, Romania  
**Citizenship:** Romanian  
**Marital status:** Unmarried

## Education and Professional experience

**1989-1993** “Dimitrie Cantemir” College, Pitesti, Romania  
**1993** Graduation  
**1993-1998** Faculty of Physics, Bucharest University, Romania  
**1998** Graduation with title of **Bachelor in Materials Science** (Mark: 9.33 from 10)  
Specialty: Science and Technology of Materials  
Diploma title: “*Field Effect Transistors with Copper Phthalocyanine Thin Films*”  
under leadership of Prof. Stefan Antohe  
**1998-1999** Master Study in Materials Science, Bucharest University, Romania  
**1999** Graduation with title of **Master in Materials Science** (Mark: 9.66 from 10)  
Specialty: Microtechnologies and Integrated Optoelectronics  
Master Diploma title: “*The effect of electron irradiation on the electrical properties of thin polycrystalline CdS layers*”  
under leadership of Prof. Stefan Antohe  
**1998-1999** **Assistant Researcher**, National Institute for Research and Development in  
Microtechnologies, Laboratory of Thin Solid Films, Bucharest, Romania  
**1999** **Design Engineer**, “Semiconix Design” Company, Bucharest, Romania  
**1999-2002** **Ph.D. Student** at Martin Luther University, Halle - Wittenberg, Germany  
**1999-2002** Doctorate Study at Max Planck Institute of Microstructure Physics, Halle, Germany  
under leadership of Prof. Ulrich Gösele and Priv.-Doz. Dr. Dietrich Hesse

# Publication List

1. **A. Visinoiu**, R. Scholz, M. Alexe, and D. Hesse, *Microstructure and dielectric properties of epitaxial BaTiO<sub>3</sub> films and BaTiO<sub>3</sub>/SrTi<sub>3</sub> multilayers*, Mat. Res. Symp. Proc. U13.2 (2003).
2. **A. Visinoiu**, R. Scholz, S. Chattopadhyay, M. Alexe, and D. Hesse, *Formation of epitaxial BaTiO<sub>3</sub>/SrTiO<sub>3</sub> multilayers grown on vicinal SrTiO<sub>3</sub> substrates*, Jpn. J. Appl. Phys. **41**, 6633 (2002).
3. **A. Visinoiu**, M. Alexe, H. N. Lee, D. N. Zakharov, A. Pignolet, D. Hesse, and U. Gösele, *The initial growth stages of epitaxial BaTiO<sub>3</sub> films on vicinal SrTiO<sub>3</sub> (001) substrate surfaces*, J. Appl. Phys. **91**, 10157 (2002).
4. **A. Visinoiu**, M. Alexe, H. N. Lee, D. N. Zakharov, A. Pignolet, D. Hesse, and U. Gösele, *Initial growth stages of epitaxial BaTiO<sub>3</sub> films on vicinal SrTiO<sub>3</sub>:Nb (001) substrates*, Mat. Res. Symp. Proc. **688**, C8.4.1 (2001).
5. A. Pignolet, C. Harnagea, H. N. Lee, **A. Visinoiu**, S. Senz, D. Hesse, *Ferroelectricity in epitaxial pulsed laser deposited Bi-layered perovskite thin films of different crystallographic orientations*, Ferroelectrics **258**, 197 (2001).
6. M. Alexe, C. Harnagea, **A. Visinoiu**, A. Pignolet, D. Hesse, and U. Gösele, *Patterning and switching of nano-size ferroelectric memory cells*, Scripta Materialia **44**, 1175 (2001).
7. H. N. Lee, **A. Visinoiu**, S. Senz, C. Harnagea, A. Pignolet, D. Hesse, and U. Gösele, *Structural and electrical anisotropy of (001)-, (116)- and (103)- oriented epitaxial SrBi<sub>2</sub>Ta<sub>2</sub>O<sub>9</sub> thin films on SrTiO<sub>3</sub> substrates grown by pulsed laser deposition*, J. Appl. Phys. **88**, 6658 (2000).
8. H. N. Lee, S. Senz, **A. Visinoiu**, A. Pignolet, D. Hesse, U. Gösele, *Epitaxial growth of non-c-oriented ferroelectric SrBi<sub>2</sub>Ta<sub>2</sub>O<sub>9</sub> thin films on Si (100) substrates*, Appl. Phys. A **71**, 101 (2000).
9. M. Ghita, M. Gheorghe, **A. Visinoiu**, *Microelectronic manufacturing of a microsensor based on polyaniline for ammonia gas sensing*, 22<sup>nd</sup> International Conference on Microelectronics, Piscataway, NJ, USA, IEEE Proceeding **2**, 619-22 (1999).

## Patent

- H. N. Lee, S. Senz, **A. Visinoiu**, A. Pignolet, D. Hesse, U. Gösele, Non-c-oriented layered-perovskite ferroelectric thin films on Si (100). Pending U.S. Patent, Reg. Nr. 09/875 630, June 06, 2001.

# International Conferences

1. **A. Visinoiu**, R. Scholz, M. Alexe, and D. Hesse, *Microstructure and dielectric properties of epitaxial BaTiO<sub>3</sub> films and BaTiO<sub>3</sub>/SrTi<sub>3</sub> multilayers*, MRS Fall Meeting, Boston, USA, December 2-6, 2002 (poster).
2. **A. Visinoiu**, R. Scholz, S. Chattopadhyay, M. Alexe, and D. Hesse, *Formation of epitaxial BaTiO<sub>3</sub>/SrTiO<sub>3</sub> multilayers grown on vicinal SrTiO<sub>3</sub> substrates*, IFFF 2002, Nara, Japan, May 28 - June 1, 2002 (poster).
3. **A. Visinoiu**, M. Alexe, H. N. Lee, D. N. Zakharov, A. Pignolet, D. Hesse, and U. Gösele, *Stranski-Krastanov growth of epitaxial BaTiO<sub>3</sub> films on vicinal SrTiO<sub>3</sub> (001) substrates*, Condensed Matter and Materials Physics Conference of the Institute of Physics, Brighton, U. K., April 7 - 11, 2002 (Best Poster Award).
4. **A. Visinoiu**, M. Alexe, H. N. Lee, D. N. Zakharov, A. Pignolet, D. Hesse, and U. Gösele, *The growth mechanism of epitaxial BaTiO<sub>3</sub> films on vicinal SrTiO<sub>3</sub> (001) surfaces*, 66<sup>th</sup> Annual Conference of the German Physical Society (DPG), Regensburg, Germany, March 11-15, 2002 (poster).
5. **A. Visinoiu**, M. Alexe, H. N. Lee, D. N. Zakharov, A. Pignolet, and D. Hesse, *Stranski-Krastanov growth mechanism of epitaxial BaTiO<sub>3</sub> films and epitaxial BaTiO<sub>3</sub>/SrTiO<sub>3</sub> multilayers on vicinal SrTiO<sub>3</sub> substrates*, 2<sup>nd</sup> International Workshop on "Oxidic Interfaces", Wittenberg, Germany, February 15-17, 2002 (talk).
6. **A. Visinoiu**, M. Alexe, H. N. Lee, D. N. Zakharov, A. Pignolet, D. Hesse, and U. Gösele, *Preparation of ferroelectric BaTiO<sub>3</sub> nanostructures on vicinal Nb-doped SrTiO<sub>3</sub> substrates*, 65<sup>th</sup> Annual Conference of the German Physical Society (DPG), Hamburg, Germany, March 26-30, 2001 (poster).
7. **A. Visinoiu**, M. Alexe, H. N. Lee, D. N. Zakharov, A. Pignolet, and D. Hesse, *Initial growth stages of epitaxial BaTiO<sub>3</sub> films on vicinal (001) Nb-doped SrTiO<sub>3</sub> substrates*, MRS Fall Meeting, Boston, USA, November 26-30, 2001 (poster).